Quantum transport phenomena in 2D semiconductor-superconductor hybrid structures

Inauguraldissertation

zur
Erlangung der Würde eines Doktors der Philosophie
vorgelegt der
Philosophisch-Naturwissenschaftlichen Fakultät
der Universität Basel

von

Ian Correa Sampaio

2023

Genehmigt von der Philosophisch-Naturwissenschaftlichen Fakultät
auf Antrag von

Erstbetreuer: Prof. Dr. Christian Schönenberger

Zusätzlicher Erstbetreuer: Dr. Andreas Baumgartner

Zweitbetreuer: Prof. Dr. Richard Warburton

Externe Experten: Prof. Dr. Thomas Ihn & Prof. Dr. Stefan Heun

Basel, den 20.06.2023

<div align="right">

Prof. Dr. Marcel Mayor
Dekan

</div>

Contents

Contents

1 Introduction

The field of quantum- and nanoelectronics has driven solid-state physics by exploring quantum states and low dimensionality. Motivated on one hand by fundamental research purposes, this field has brought remarkable breakthroughs in engineering and controlling quantum states, broadening our understanding of nature. On the other hand, the field is thrust by applications in computation and sensing, witnessed by the miniaturization problem proposed by Moore [1, 2] and the rise of quantum computation [3–5].

A specific area providing fruitful outcomes to both ends is the physics of hybrid devices, particularly, semiconductors-superconductors devices. These have attracted large interest in fundamental research, for example as potential hosts of topological quantum states [6–9], thermoelectrics [10], or even as a source of spin-entangled electron pairs [11]. From a technological point of view, these devices can be used as gate tunable qubits [12], in sensing small magnetic fields [13] and radiation [14].

So far, hybrid devices have been successfully implemented in many systems such as metals [15], molecular-beam epitaxy (MBE) grown quantum wells [16] and nanowires [17]. With the discovery of graphene [18] a new class of materials came into play, the two-dimensional materials [19].

Two-dimensional (2D) materials represent strong candidates for high performance devices at the atomic limit [20], being compatible with silicon chip fabrication [21]. On a fundamental research level 2D materials are revolutionizing the field of quantum electronics and optics, with their extraordinary properties, such as strong spin-orbit interaction, spin and valley degrees of freedom [22, 23], the possibility of creating complex vertical heterostructures [24] and exploration of the twist angle which opened a whole new field of research [25]. A step further could be given by combining the exotic properties of these 2D materials with superconducting hybrid devices. This has successfully been done for graphene [26] and has shown promising results of other semimetals [27], however, very few results have been reported for 2D semiconductors [28, 29]. The immediate benefit of having a gate tunable system is the fine control over the charge carriers in the device as a whole or as locally defined nanostructures [30].

1

In this dissertation, we introduce platforms for hybrid semiconductor- superconductor devices based on 2D semiconductor crystals, namely molybdenum disulfide (MoS_2) and indium selenide (InSe). These are combined with superconductors such as aluminium, molybdenum rhenium, and tin. The main challenge lies in achieving reliable electrical contact to the 2D semiconductors and obtaining coherent coupling across the material interface. The properties of these devices are explored in spectroscopy measurements which show evidences of quantum coherent phenomena. Additionally, we demonstrate control over the semiconductor by a well-defined nanostructure, a quantum point contact, which can be used for probing superconducting proximitized regions [31], but for many other applications.

Outline of the thesis

We start the thesis by providing the theoretical background in low dimension transport, superconductivity and 2D semiconductors in chapter 2. Chapter 3 describes the techniques employed for fabricating our devices including the isolation of the 2D crystals, stacking of heterostructures, contacting techniques, and a description of the measurement setup. The experimental part starts in chapter 4. We engineer confinement potential in the 2D system using a quantum point contact and probe its effects on the system. Chapter 5 and 6 are dedicated to superconductor-semiconductor hybrid devices. In chapter 5, we introduce a novel contacting technique, now extended to hybrid devices. We probe the superconducting energy gap in temperature and magnetic field in spectroscopy measurements. Additionally, we observe evidences of coherent transport, expressed in quantum interference effects phenomena. In chapter 6 we demonstrate the versatility of the contacting technique by employing it to InSe. The quantum interference effects present some divergences from the MoS_2 devices, which are discussed in terms of the semi-classical model. Lastly, in chapter 7 we summarize the findings and propose future experiments.

2 Theoretical background
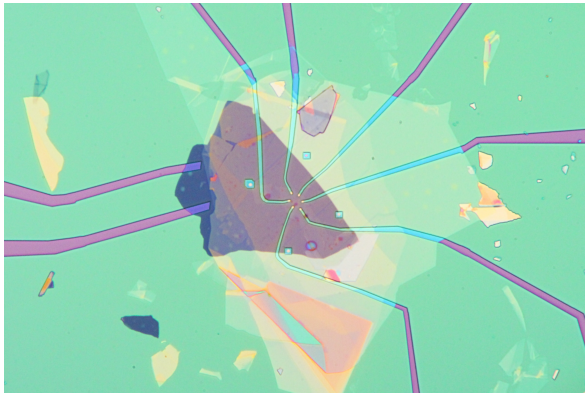
In this chapter, we discuss the relevant theoretical concepts necessary to understand the experiments in this work. The electrical properties and physical phenomena are briefly described with references for further readings. We start by introducing 2D materials, in particular, molybdenum disulfide (MoS_2) and indium selenide (InSe). We describe the fundamental physical mechanisms in low-dimensions structures, such as quantum point contacts and quantum dots. After that, we give a short introduction to superconductivity and its effects in normal-superconductor junctions.

2.1. Electronic transport phenomena

We start by providing some basic quantities of electronic transport through 2D systems which will be used later on, such as the conductivity, mobility and charge carrier density.

2.1.1. Conductivity in the Drude model

For the mean free path shorter than other relevant length scales, like the device size or the coherence length, the Drude model can be used to describe the transport properties [32]. We consider a non-interacting electron gas in a solid with randomly distributed scatterers. The electrons are accelerated by an electric field $\mathbf{E}$, momentum is randomized by scattering. The average momentum gained between two collisions is $\langle \mathbf{p} \rangle = e\mathbf{E}\tau$, where e is the electron charge and τ is an average time between collisions, called mean free time. Assuming a density n of electrons in this conductor, a current density is expressed by

$$\mathbf{j} = en(\frac{\langle \mathbf{p} \rangle}{m^*}) = \frac{ne^2\tau}{m^*}\mathbf{E} \tag{2.1}$$

where m^* is the effective mass of the electrons in the periodic potential of a solid. The quantity connecting the current density $\mathbf{j}$ and the electric field applied $\mathbf{E}$ is the conductivity, defined as

$$\sigma_D = \frac{ne^2\tau}{m^*}. \tag{2.2}$$

The resistivity ρ is defined $\rho = 1/\sigma_D$. An important quantity is the mobility, which is defined as

$$\mu = \frac{e\tau}{m^*}, \tag{2.3}$$

such that $\sigma = ne\mu$. The scattering time τ provides a characteristic length scale between the scatterers, known as mean free path ℓ_{mfp}, which characterizes the average length an electron can travel without relaxing its momentum and its given by

$$\ell_{\text{mfp}} = v_F\tau \tag{2.4}$$

where v_F is the Fermi velocity of the electrons carrying current $v_F = \hbar k_F/m^*$. The Fermi wavevector k_F is given by the Fermi energy E_F by

$$k_F = \sqrt{\frac{2m^*E_F}{\hbar^2}}. \tag{2.5}$$

2.1.2. Charge carrier density and field effect mobility

To estimate the number of charge carriers induced by an applied voltage at the gate V_g, we consider a simple plate capacitor model in 2D semiconductor devices. The charge carrier density is then simply

$$n = \frac{c}{e} \left(V_g - V_o \right) \tag{2.6}$$

with the capacitance per unit of area $c = \varepsilon_0 \varepsilon_r / d$, where ε_0 (ε_r) is the vacuum (relative) permittivity of the dielectric material and d the thickness of the dielectric material. V_o is the depletion voltage, associated to the bottom of the conduction band (CB). We use $\varepsilon_{SiO_2} \approx 3.9$ and $\varepsilon_{hBN} \approx 4$.

From the gate voltage response of a semiconductor and using equations 2.2 and 2.6, one has a recipe to obtain the field effect mobility μ_{FE}

$$\mu_{FE} = \frac{d\sigma}{dV_g} \cdot \frac{d}{\varepsilon_0 . \varepsilon_r} \tag{2.7}$$

2.1.3. Density of states in two dimensions

For a parabolic dispersion relation in two dimensions centered at gamma point

$$E = \frac{\hbar^2 \mathbf{k}^2}{2m^*} \tag{2.8}$$

$\mathbf{k}$ are the electron wavenumber in a plane $k_{x,y}$. For a given energy E_F the number of states available in the system per unit of area is given by the sum in reciprocal space of the available $k_{x,y}$

$$N(E) = 2 \, (\text{for spin}) \cdot \frac{1}{A} \int_0^{\mathbf{k}(E)} d^2 k = \frac{m^*}{\pi \hbar^2} \int_0^E dE' = \frac{m^*}{\pi \hbar^2} E \tag{2.9}$$

with the density of states in two dimension

$$D_{2D}(E) = \frac{dN(E)}{dE} = \frac{m^*}{\pi \hbar^2}. \tag{2.10}$$

2.2. Two-dimensional materials

A two-dimension electron gas (2DEG) is typically obtained in a quantum well by offsets in the band structure at the interfaces of materials such as the interface of GaAs/AlGaAs [33] or InAs/InGaAs [34]. The band offsets form effective potential barriers in the out-of-plane direction confining the freedom of electrons to a two-dimensional plane. These structures are grown by Molecular Beam Epitaxy, a costly method in resources and personnel. The isolation

of a single layer graphite in 2004 [18], graphene, opens a new opportunity to low dimensionality. 2D materials are crystals that can be thinned down to a single layer of atoms, producing natural platforms for 2DEGs. Since then, many other materials joined the 2D materials family [19]. The semiconductors MoS_2, InSe, black phosphorous, insulators such as hexagonal boron nitride (hBN), and even superconductors such as $NbSe_2$ and $PdTe_2$. These materials are all composed of planes of covalent bonds interconnected by van der Waals force to the adjacent planes. Besides the possibility pf mechanical exfoliating them to thinner layers, it is also possible to create heterointerfaces between materials with different lattices without causing interface strain [24], which gives a greater freedom of choice compared to MBE and similar techniques. Beyond the vertical degree of freedom, 2D materials founded the field of twistronics, by engineering band structures using the twist angle between crystal planes [25]. In this work, we focused on two 2D semiconductors, namely MoS_2 and InSe.

2.2.1. Molybdenum Disulfide
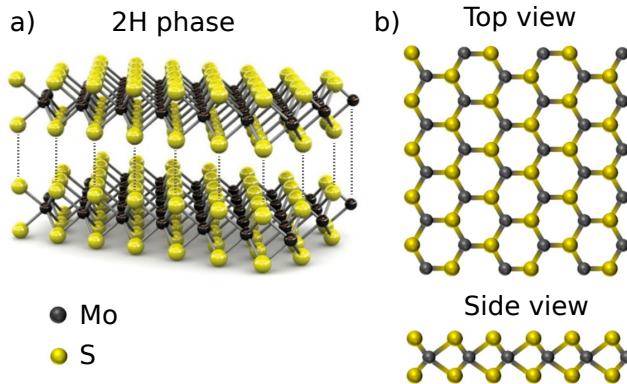
Figure 2.1. Illustration of the crystal structure of 2H phase MoS_2 in different perspectives. Adapted from [35, 36].

Transition metal dichalcogenides (TMDCs) are interesting materials for their large spin-orbit interaction, large effective electron masses, optical activity, and potentially large electron mobility. These materials have a chemical composition of MX_2, where M is a transition metal (such as molybdenum, tungsten, niobium, etc.) and X is a chalcogen (sulfur, selenium, tellurium, etc.). Every M atom forms covalent bonds to X atoms, such that a plane of M atoms is sandwiched between planes of X atoms, as shown in Figure

2.1. Within the TMDC family MoS_2 is the most investigated semiconductor. Like the other members of its family, MoS_2 has in-plane six-fold symmetry of rotation, with atoms placed in a honeycomb from top view.

Every Mo atom is bonded to six S atoms with a spacing of about 2.5 Å. The single layer MoS_2 is connected to the adjacent one by van der Waals attraction with a spacing of about 0.6 Å.
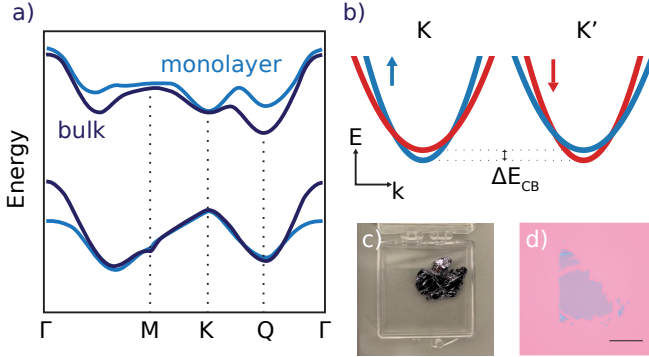
Figure 2.2. a) Band structure of bulk and monolayer MoS_2. b) Detail of the spin-split close to the CB minimum around the K points. c) Bulk crystal d) Optical image of monolayer MoS_2. Scalebar is $6\,\mu$m.

The six-fold symmetry is also reflected in reciprocal space. The band structure of MoS_2 is depicted on Figure 2.2. For a monolayer MoS_2 there is a direct band gap with band edges located at the K and $K^{'}$ points of the Brillouin zone (BZ) about 2 eV. For multilayer, the CB minimum shifts to the Q points of BZ, with three inequivalent Q points, resulting in an indirect band gap.

For thin crystals of MoS_2 the parity of the layer number determines the presence of an inversion symmetry in the crystal. An odd number of layers do not have an inversion center for the chalcogenide atoms. As a consequence, mono- and trilayer MoS_2 present an intrinsic spin-orbit interaction and a spin splitting in the bands [37]. Calculations of an intrinsic spin-orbit interaction yield in a spin-split in opposite directions for K and $K^{'}$ points of about 3 meV [38]. However, experimental data points to values five times higher [39]. The two subbands have slightly different effective masses, i.e. in different curvatures in the dispersion relation, as shown in Figure 2.2. The spin and valley degrees of freedom make MoS_2 an interesting platform for spin- and valleytronic devices [40].

MoS_2 is usually a n-doped semiconductor [38]. The mobility encountered in

hBN encapsulated devices reaches up to $\mu \sim 5000\,\mathrm{cm}^2/\mathrm{Vs}$ [39]. Nevertheless, recent advances in synthesis resulted in electron mobilities above $44000\,\mathrm{cm}^2/\mathrm{Vs}$ [41].

Electron-electron interactions play an important role in MoS_2. At low charge carrier density, there is evidence for a first-order phase transition to a ferro-magnetic phase due to inter-valley exchange scattering [42]. At high CB oc-cupation, utilizing ionic liquid gating, MoS_2 becomes a superconductor [43]. At such carrier concentration, it is thought that phonon-mediated coupling overcomes Coulomb repulsion turning the system into the superconducting state.

Although MoS_2 can exhibit high mobility, it is also known for containing several types of crystal defects. The most common are S vacancies, which are extensively studied [44–46] and in some cases even engineered [47, 48].

2.2.2. Indium Selenide
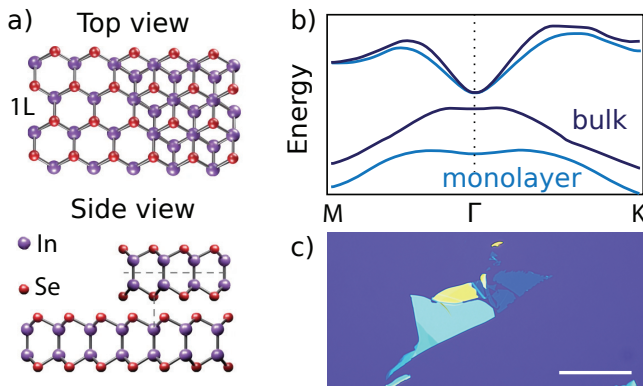
Figure 2.3. a) Illustration of the crystal structure of γ-phase InSe and stack-ing of bilayer in ABC configuration. Adapted from [49]. b) Band structure of bulk and monolayer InSe. Adapted from [50]. c) Optical image of exfoliated InSe flakes. Scalebar is $10\,\mu\mathrm{m}$.

Another group of 2D materials is the III-VI post-transition metal monochalco-genide such as gallium selenide and indium selenide (InSe). InSe attracted interest among the 2D semiconductors due to high mobility $\sim 12700\,\mathrm{cm}^2/Vs$ and small effective mass $m_e^* \simeq 0.14 m_e$ [49].

Its essential layer is composed by a In-Se-Se-In sheet of atoms connected by covalent bonds, as shown in Figure 2.3 a).

InSe is very promising for optical applications. It possesses a direct bandgap from bulk (0.26 eV) to bilayer (0.99 eV), which corresponds to photon energies from near-infrared to visible. The monolayer InSe has an indirect bandgap with CB minimum at the Γ point and a Mexican hat shaped valence band (VB), shown in Figure 2.3 b).

Recent results demonstrate a field effect transistor based in 2D InSe with gate efficiency, ohmic current injection, and channel length reaching the current state-of-the-art Si standards [51]. The Mexican hat-shaped VB could host ferromagnetism, superconductivity, and topological quantum phase transition [52]. Quantum hall effect has been observed for up to 10 layers flakes [49]. InSe possesses Rashba type spin-orbit interaction tunable with electric field and layer number [53]. Gate confinement nanostructures have been demonstrated experimentally [54, 55]. Predictions exist of engineering superconductivity in InSe by various mechanisms, such as twisting [56], doping [57] or straining [58].

2.2.3. Schottky barrier formation at metal-2D semiconductors interface

At the interface between a metal and a bulk semiconductor, there is an abrupt change in the band structure and the Fermi energy. Once metal and semiconductor are put in contact, carriers are exchanged until an equilibrium distribution is reached, where the electrochemical potential becomes equal across the interface and far in the bulk of the two materials. This change in the chemical potential across the interface, compared to the bulk values, requires a compensating change in the electrical potential bending the semiconductor band. The result is an energy barrier, called Schottky barrier, which in a first approximation is calculated by the difference of the metal work function and the semiconductor electron affinity [59].

The situation for 2D materials differs from the 3D case since the thickness is much shorter than the depletion width. The Schottky barrier energy, in this case, is thought to be the difference between the metal work function energy and the conduction band energy of the 2D semiconductor [60]. The literature uses the term Schottky barrier in the context of 2D materials as a term to describe all the mechanisms that can induce Fermi level pinning to the band gap or that cause worsening of the contact quality. These are several factors, which are summarized below starting from a dirty regime, that is when defects modify the electronic properties of the system, to a clean regime, where we consider perfect interfaces and crystal lattices.

Starting from the dirty regime, defects induce Fermi level pinning by several mechanisms [60], namely chemical reactions and intercalation of the contact material into the 2D semiconductor, such as shown in XPS characterization of TMDCs contacted by Ti, Ir, Sc and Cr [61–63]. The intercalation and reac-
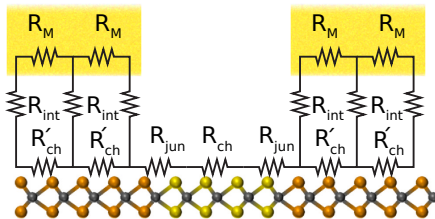
Figure 2.4. Schematic of the generalized resistance network that generates a Schottky barrier in a thin semiconductor FET.

tion of Pd in WTe_2 is also well studied and used to induce superconductivity in the system [64, 65]. High-temperature metal deposition can also introduce defects by kinetic damage to the 2D semiconductor [66]. Direct exposure of TMDCs to polymers is known to cause degradation of the interfaces [67]. Vacancies are commonly present in 2D materials and also a cause of the Schottky barrier, as they generate defect states up to 0.4 eV below the CB minimum in MoS_2 [68, 69]. Strain is also known for impacting the band structure of 2D semiconductors [58, 70, 71], which can also influence the contact quality [72, 73].

Even if one assumes an entirely clean interface between the 3D metal and the 2D semiconductor, there are still mechanisms for a barrier formation such as metal induced gap states (MIGS), interface dipoles and tunneling through van der Waals gap and the classical charge exchange mechanism. MIGS are formed when a semiconductor is in proximity to a metal. The wavefunction of the electrons in the metal causes a perturbation in the thin semiconductor, giving rise to new states in its band gap by hybridization [74, 75]. The formation of interface dipoles arises from charge transfer [76], pushback effect [77] or the energy level broadening effect [78], which leads to shifts in the energy levels. In addition, the presence of a physical gap, that can be as large as a few angstroms, realized by the dangling bonds in the chalcogenide atoms creates a short vacuum segment for the electrons to tunnel [79].

The effect on transport experiments is summarized in the resistance network shown in Figure 2.4. Starting from the left electrode represented by the net of resistors R_M, the tunneling process of electrons from this electrode to the 2D material is described by the parallel resistors R_{int} at the interface. Inside the 2D material, below the metal, we have a sheet resistivity different from the free semiconductor symbolized by the resistors R'_{ch}. A resistor R_{jun} separates the junction between different doped parts of the 2D material. Finally, R_{ch} represents the sheet resistance of the open 2D channel [80]. The ratios between R_{int} and R'_{ch} determines how much of the current flows through the metal only

passing through R_{jun} or through the parallel R_{int} and $R_{\text{ch}}^{'}$. The transfer length characterizes the distance over which the current is transferred from the metal contact to the semiconductor and can also determine whether the area or length of the contacts dominates the interface resistance.

There is no consensus over the magnitude of the transfer length of MoS_2, with both, few nanometers [81–83] and micron-scale [84, 85] being reported. Some publications suggest a dependence on the crystal thickness [86], a dependence on the presence of oxide layers [87] or even asymmetric scaling of source and drain leads [88].

Theoretical predictions in the literature suggest that contacting the edge of the 2D materials would improve the contact quality [89, 90], reducing the barrier strength, due to a reduction of the vdW gap and the formation of MIGS. However, edge contacts showed no advantage over top contacts so far [91].

2.3. Transport through narrow channels, Quantum Point Contacts
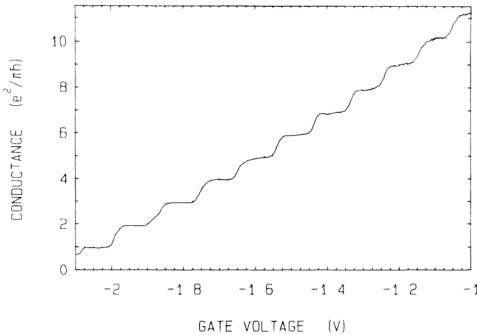
Figure 2.5. Quantum point contact conductance as a function of gate voltage. Figure from [92].

In 1988, two groups [92, 93] independently demonstrated that the conductance of a current passing through a narrow clean constriction in a 2DEG occurs in quantized values which were multiples of what is now called conductance quantum.

In the transverse direction, the splitgate confines the electrons in a potential well of about the size of the Fermi wavelength at discrete energies. By tuning the voltage applied to the gates one can control the number of modes

occupied. For every mode, the conductance adds a step of e^2/h to the total conductance. For N modes occupied, with spin degeneracy of 2, the total conductance through the constriction is

$$G_{\text{QPC}} = 2 \cdot \frac{e^2}{h} N \tag{2.11}$$

This narrow quasi-one dimensional constriction is known as quantum point contact (QPC). To understand the quantization of the conductance in detail we consider a long wire (in z-axis) with finite width (in x) and height (in y-axis). A three-dimension, time-independent Schrödinger equation describing the electrons in the wire is

$$\left[-\frac{\hbar^2}{2m} \nabla^2 + V(x,y,z) \right] \psi(x,y,z) = E\psi(x,y,z). \tag{2.12}$$

Here we consider an uniform wire, where the potential $V(x,y,z)$ does not depend on the current direction along z-axis. This differential equation is separable into solutions in z-direction and in the xy-plane, such that the electron wavefunction is

$$\psi(x,y,z) = \chi_n(x,y) \cdot \frac{1}{L} e^{ik_z^n z} \tag{2.13}$$

the prefactor $1/L$ for normalization in the current. For the cross-section direction, we consider a quadratic dispersion relation, such that

$$\varepsilon_n(k_x, k_y) = \frac{\hbar^2}{2m^*} \left(k_{n_x}^2 + k_{n_y}^2 \right) \tag{2.14}$$

The wave numbers $k_z^n = \pm\sqrt{\frac{2m}{\hbar^2}(E - \varepsilon_n)}$ describe the electrons carrying current in the wire from the left (right), only if $E > \varepsilon_n$, otherwise it describes evanescent waves. From the electronic wavefunction, we define the group velocity as

$$v_{n_z} = \frac{1}{\hbar} \frac{dE}{dk_{n_z}} = \frac{\hbar k_n}{m} \tag{2.15}$$

Now considering a non-equilibrium net current generated by a voltage bias V_{SD} applied at the ends of the wire, we can calculate the current carried by single mode n with

$$I_n = \frac{e}{2\pi} \int_0^\infty D_{1D} v_n \left[f_L(E) - f_R(E) \right] dE \tag{2.16}$$

where $f_{L,R}(E)$ are the Fermi distribution in the reservoirs on left and right side of the wire. The density of states in one dimension $DoS_{1D} = 1/(dE/dk)$ cancels the energy dependence with the group velocity v_n leaving

$$I_n = \frac{e}{h} \int_0^\infty [f_L(E) - f_R(E)] \, dE \qquad (2.17)$$

The difference in Fermi occupations close to $T = 0$ can be taken as $[f_L(E) - f_R(E)] = e(\mu_L - \mu_R) = eV_{SD}$, which results in

$$I_n = \frac{e^2}{h} V_{SD} \qquad (2.18)$$

$G = I/V_{SD}$ we obtain $G_n = e^2/h$ for the conductance of a single mode. For a Fermi energy such that N modes are in the "bias window" between $\mu_l eft$ and $\mu_r ight$ the total conductance is

$$G_N = \frac{e^2}{h} N \qquad (2.19)$$

Now we adapt this picture to a two-dimensional conductive plane and we make some assumptions for the shape of confinement potential $V(x, y, z)$ created by splitgates.

2.3.1. Parabolic potential approximation

We define the y direction perpendicular to the current flow in the constriction and x along the current flow. The potential landscape throughout a QPC can be understood in its simplest form as given by saddle point with parabolic shapes along each axis, expressed by

$$V_p(x, y, z) = -\frac{1}{2} m^* \omega_x^2 x^2 + \frac{1}{2} m^* \omega_y^2 y^2 + V_0) \qquad (2.20)$$

where ω_x and ω_y represent the curvatures in x and y, respectively, and V_0 is an offset from the bottom of the potential. In the y direction the eigenenergies are those of a harmonic oscillator

$$E_y(n) = \hbar \omega_y (n + 1/2) \qquad (2.21)$$

where $n \in \mathbb{N}_0$ represents the QPC modes. The transmission through the potential also depends on the curvature on x direction and is given by [94]

$$T_n = \frac{1}{1 + e^{-2\pi \varepsilon_n}}, \quad \text{where} \ \ \varepsilon_n = \frac{E - \hbar \omega_y (n + 1/2) - E_z}{\hbar \omega_x}. \qquad (2.22)$$

With that, we can rewrite the conductance of the QPC as

$$G = \sum_n T_n(E_F) \qquad (2.23)$$

summing up to the N-th occupied mode until the Fermi energy E_F.

2.3.2. Hard wall potential approximation

We now consider a QPC potential with a sharper confinement, the hard wall potential. In this case, we describe the potential as

$$V_h = \begin{cases} V_0, & \text{if } -w/2 \leqslant y \leqslant w/2 \\ \infty, & \text{otherwise} \end{cases} \qquad (2.24)$$

where W is the width of the potential. The energy separation for the transversal modes is given by the particle-in-a-box solutions

$$E_y(n) = \frac{\pi^2 \hbar^2 n^2}{2m^* W^2} + V_0. \qquad (2.25)$$

Here the spacing between energy levels increases for increasing n. So far we considered perfect transmission and no scattering between the modes. But if the transverse mode energies ε_n depend on x, the eigenmodes in the QPC center become coupled [95]. For example for the hard wall potential we obtain

$$\left[-\frac{\hbar^2}{2m} \frac{\partial^2}{\partial z^2} + \varepsilon_n(E) - E \right] \psi_n(x,y,z) = \Lambda_{nm} \psi_n(x,y,z) \qquad (2.26)$$

where

$$\Lambda_{nm} = \frac{\hbar^2}{2m} \int \chi_{mz}(y) \left[2 \frac{\partial}{\partial z} \chi_{nz} \frac{\partial}{\partial z} + \frac{\partial^2}{\partial z^2} \chi_{nz} \right] \qquad (2.27)$$

mixes the longitudinal modes. This can cause a non-unitary transmission of the QPC modes and fluctuations in the step-like conductance. If the longitudinal wavefunction smoothly varies across the z direction we call it the adiabatic approach where $\Lambda_{nm} \approx 0$.

Further informations and detailed derivations of these results can be found in Refs. [32], [95] and [96].

2.4. Coulomb blockade and Quantum Dots

Considering a conductive island connected to its environment through small or highly resistive junctions, the energy $U \sim e^2/C$ for charging a single electron into the island becomes relevant for small capacitance C. If this energy is higher than the thermal energy $k_b T$ and U/e is higher than the voltage across the junction, no current can flow, this regime is called Coulomb blockade. Quantum dots (QD) are small conductive islands where the motion of electrons is confined in all spacial dimensions, creating quantized energy levels, related to the quantized kinetic energy of the orbitals allowed for the electrons in the confinement. The spacing between these energy levels is often called single-particle level spacing δE and is usually comparable to the changing energy of the QD. Consequently, the energy required to add an electron to the QD is

$E_{add} = \mu_{N+1} - \mu N = e^2/C + \delta E$. In general, a charge can be transfer to a QD when at least one of the energy levels lies in the voltage bias window of the leads as shown in Figure 2.6. Additionally, the electrochemical potential of the energy level in the QD can be tuned via an electric voltage, e.g. applied by a gate V_g. With these two parameters, one obtains the so-called Coulomb diamonds represented in Figure 2.6. The blue lines represent the edge of the diamond in which the transport is blocked. The panels I to III show different biasing conditions in which either source or drain aligns to one of the energy levels, changing the dot occupation by a charge e. The other features in Figure 2.6 are beyond the scope of this work.
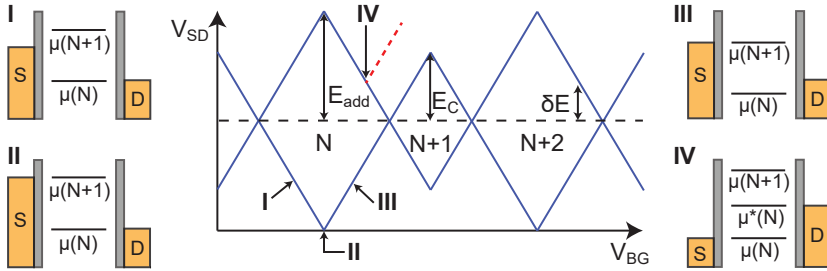

Figure 2.6. Coulomb blockade of a QD. The diagrams from I to IV show different source S and drain D configurations with respect to the quantized levels in the QD. At the center a plot of the differential conductance as a function of the bias voltage V_{SD} and the gate voltage V_{BG}. The blue lines describe the edges of the Coulomb diamonds where the transport is blocked. The occupation of the QD is marked by N, $N+1$, etc. Adapted from [97].

If several QD are present in a sample in a disordered form, their Coulomb diamonds overlap in a chaotic pattern, often referred as Coulomb shards.

2.5. Superconductivity

In 1911, three years after being able to first condense Helium to the liquid phase, Kamerlingh Onnes observed that around $4.2\,\mathrm{K}$, the electrical resistance of mercury dropped from $0.1\,\Omega$ to unmeasurably small values [98]. This phenomenon is now known as superconductivity. Another important property observed in superconductors is the complete expulsion of magnetic fields, this perfect diamagnetism is known as the Meissner effect [99]. A phenomenological explanation was provided by London in 1937 [100], who also introduced the London penetration depth λ_L, a length characterizing the scale over which the fields are expelled. As observed initially for mercury, superconductivity

is quenched above a certain critical temperature T_c, but also above a certain critical field B_c. Superconductors can be classified in type I, fully expelling magnetic fields up to B_c, or type II, hosting vortices that allow penetration of discrete magnetic flux quantum $\Phi_0 = h/2e$.

In type II superconductors, the fields are expelled completely up to B_{c1}, while for larger fields discrete normal regions develop, corresponding to one superconducting flux quantum (charge 2e). At the second critical field $B_{c2} > B_{c1}$, the superconductivity is then fully suppressed (with the possible exception of surface superconductivity). For superconductors in general there is also a finite amount of supercurrent that can be carried without dissipation, the critical current I_c.
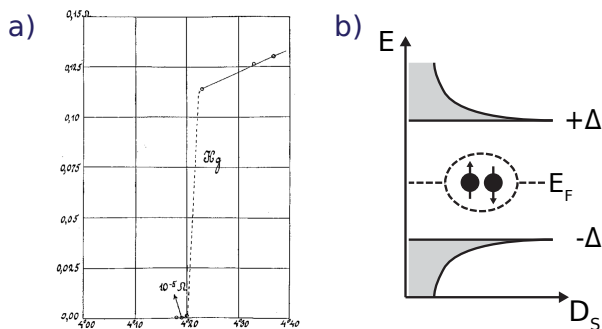
Figure 2.7. a) Resistance of mercury as a function of temperature. Adapted from [98]. b) Quasi-particle density of states of a superconductor given by equation 2.28. The Cooper pair condensate sits at the Fermi energy E_F.

In 1957, Bardeen, Cooper, and Schrieffer provided a microscopic understanding of these phenomena (BCS theory [101]). An attractive interaction mediated by phonons pairs electrons of opposite momentum and spin in so-called Cooper pairs. These correlated pairs of electrons possess a common ground state, called the BCS ground state. Single quasiparticle excitations can be created from the superconductor ground state above a certain energy Δ. The density of states for the quasiparticle excitations is described by

$$D_S(E) = \begin{cases} D_N(E_F) \dfrac{|E - E_F|}{\sqrt{(E - E_F)^2) - \Delta^2}}, & \text{if } |E - E_F| > \Delta \\ 0, & \text{otherwise.} \end{cases} \tag{2.28}$$

D_N is the density of states in the normal state. Figure 2.7 b) plots $D_S(E)$.

The zero density of state for quasiparticles within $|\Delta|$ is also known as the energy gap of a superconductor. Superconductivity can also be described by a heuristic macroscopic wavefunction introduced by Ginzburg and Landau [102], who introduced a global wavefunction ψ_S representing the Cooper pair condensate, as

$$\psi_S(\mathbf{r}, t) = \sqrt{n_s((\mathbf{r}, t))}e^{i\varphi(\mathbf{r}, t)}, \tag{2.29}$$

where n_s is a density of Cooper pair and φ is the macrocopic phase of the superconductor. The Ginzburg-Landau theory also includes the coherence length ξ which gives a characteristic length for changes in the phase of Δ. For bulk superconductors the coherence length is given by $\xi_0 = \hbar v_F/\pi\Delta$ and in the dirty limit $\xi = \sqrt{\hbar D/2\Delta}$.

Further readings in superconductivity can be found in Ref. [103].

2.5.1. Josephson effect

In 1962 Brian D. Josephson proposed that superconductors connected by a short non-superconducting segment could still carry a supercurrent [104]. Before this prediction, it was taken that only single electrons could tunnel independently through a barrier, but as it was later observed by Anderson and Rowell, Cooper pairs could also tunnel in a correlated manner through a weak link carrying a supercurrent [105].

The current across a Josephson junction driven by the phase difference between the two superconductors $\varphi_1 - \varphi_2$, as described by the first Josephson relation given by

$$I(\varphi) = I_c \sin(\varphi), \text{ with } \varphi = \varphi_1 - \varphi_2 \tag{2.30}$$

where I_c is the critical current of the junction. This effect is known as the DC Josephson effect. If a voltage is applied across the junction, it causes a time-dependent variation of the phase difference

$$\frac{d\varphi}{dt} = \frac{2eV}{\hbar}. \tag{2.31}$$

Inserting into the first Josephson relation results in

$$I(V, t) = I_c \sin(\varphi_0 + 2eVt/\hbar). \tag{2.32}$$

A voltage bias causes a sinusoidally oscillating current across the junction, known as AC Josephson effect.

For further readings in Josephson effect physics refer to [95] and [106].

2.5.2. SNS junctions

The weak link can be realized by an insulating oxide layer (SIS junctions) acting as a tunnel barrier, a constriction in a superconductor (SS$'$S junctions), or a normal conductor (SNS junction). Below we describe the microscopic process involving SNS junctions.

Andreev Reflection and Transmission through a N-S interface

As shown in equation 2.28 for energies within the superconducting gap i.e. $(E - E_F) < \Delta$ the quasiparticle density of states in a superconductor is zero, depicted in Figure 2.8 a). Though it is not allowed for quasiparticles in the normal metal to tunnel to the superconductor, a process called Andreev reflection (AR) allows the transmission of two charges. An electron with wavenumber **k** on the normal metal hits the interface to a superconductor and it is retro-reflected into a hole, which is the time-reversed of the original electron with wavenumber **k**. The charge $2e$ missing at the normal side allows the creation of a Cooper pair (with net momentum zero) on the superconductor side. The process is depicted in Figure 2.8 b). The inverse process can also occur, where a charge of $2e$ in form of a Cooper Pair vanishes from the superconductor side by absorbing a hole from the normal side and turning into an electron.

A description of the transmission probabilities of the Andreev process was provided by Blonder, Tinkham, and Klapwijk (BTK) [107]. They depend on the transmission coefficient T of a single electron, which is a property of the interface and varies from 0 to 1. In the BTK model, T is given by a repulsive potential barrier $H\delta(x)$, where H is a barrier height. We can then write the transmission as

$$T = \frac{1}{1 + Z^2} \text{ where } Z = H/\hbar v_F. \tag{2.33}$$

here v_F is the group velocity at the Fermi energy. Considering $E < \Delta$, the coefficient A, the probability of an AR, and B, the probability of a normal reflection at the N-S interface are given by

$$A = \frac{\Delta^2}{E^2 + (\Delta^2 - E^2)(1 + Z^2)^2} \tag{2.34}$$

$$B = 1 - A. \tag{2.35}$$

Figure 2.8 c) shows the reflection probabilities A and B as a function of energy for different values of transmission coefficients T at the interface. Above the energy gap there are transmission C, of an electron with a wavevector on the same side of the Fermi surface and the transmission D, of an electron with a wavevector crossing through the Fermi surface.
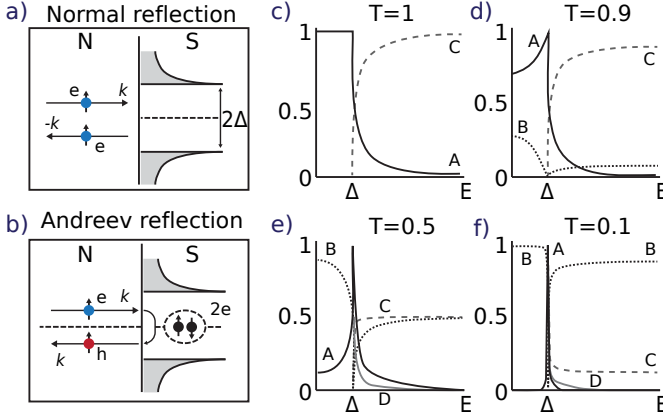
Figure 2.8. a) Schematic of normal- and b) Andreev reflection at the N-S interface. DoS of the superconductor are represented by the shaded areas. c) to f) Probabilities A, B, C, D as a function of energy for the indicated transmission values. Adapted from [107].

The current through an N-S interface with V applied bias is written in terms of these coefficients by

$$I = N_0 \frac{e}{h} \int_{-\infty}^{\infty} [1 + A(E) - B(E)] \cdot [f(E) - f(E + eV)] dE. \qquad (2.36)$$

where N_0 is the normal state conductance.

If the interface is not clean, such that $T \ll 1$, the probability of an AR decays proportionally to T^2 for $E \ll \Delta$, meaning that this process is severely suppressed.

The coherence between incident electron and retro-reflected hole in an AR results in a non-zero probability of finding a Cooper pair in the normal conductor. Therefore, the Cooper pair density decays continuously on the scale of the BCS coherence length ξ. This 'leak' of Cooper pairs into normal conductor is known as the proximity effect [108].

Andreev bound state

After an AR the hole reflected into the normal conductor is free to travel to another N-S interface, say in series with the previous. There, the Andreev process can take place once more converting the hole into an electron and transmitting the change $2e$ into the superconductor. The electron can restart the process creating consecutive loops of ARs at the interfaces. If the electron
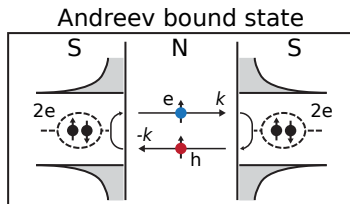
Andreev bound state

Figure 2.9. Schematic of consecutive AR generating a bound state in the normal conductor.

(and hole) partial waves interfere constructively, discrete states develop, called Andreev Bound States (ABS), depicted in Figure 2.9. For every AR the phase acquired for an electron into a hole ϕ_{eh} and for a hole into an electron ϕ_{he} are

$$\phi_{eh} = -\arccos(E/\Delta) + \phi_S, \text{ and } \phi_{he} = -\arccos(E/\Delta) - \phi_S \tag{2.37}$$

The total phase acquired in a full cycle of reflection is

$$\phi_{\text{tot}} = (k_e - k_h)L + \phi + 2\arccos(E/\Delta) \tag{2.38}$$

here the first term is a phase gained within the normal region with length L, and ϕ is the phase difference between the two superconductors. For constructive interference $\phi_{\text{tot}} = 2\pi n$ with $n \in \mathbb{Z}$. We can solve for the energy in the short junction limit ($L \ll \xi$) which results in

$$E_{\pm}^{ABS} = \pm\Delta\cos(\phi/2) \tag{2.39}$$

The total current through the SNS junction (in the short junction limit, $L \ll \xi$) is given by the Ambegaokar-Baratoff relation between the normal state resistance and the critical current of the junction [109] as

$$I_{SNS} = \frac{\pi\Delta\sin(\phi)}{2eR_N}\tanh\left(\frac{\Delta}{2k_BT}\right) \tag{2.40}$$

In the long junction limit ($L \gg \xi$), E^{ABS} is determined by the phase acquired by the quasiparticles in the normal conductor, which scales with k_F. With that, additional states can form inside the superconducting gap [110, 111].

A bound state can also be formed between a single N-S interface and one normal interface as long as in the proximity region. The normal interface can be e.g. the boundaries of the system or defects that reflect the carriers into the superconductor creating successive reflections.

Reflectionless tunnelling

As seen in 2.5.2, in a N-S interface with a small transmission coefficient T the probability of an AR process is highly suppressed with T^2, such that if $T \ll 1$ the Cooper pair tunneling can be neglected compared to the single electron processes.

However, in a diffusive sample electrons are scattered by defects leading to multiple reflections at the N-S interface, as shown in Figure 2.10 a) for the case of two reflections at the N-S interface. Isolated, each one of these reflections has a small probability of AR. But after N-th coherent reflection the probability of an AR is drastically enhanced reaching $T_{tot} = 1$ for strong disorder, an effect known as "reflectionless tunneling" [112].
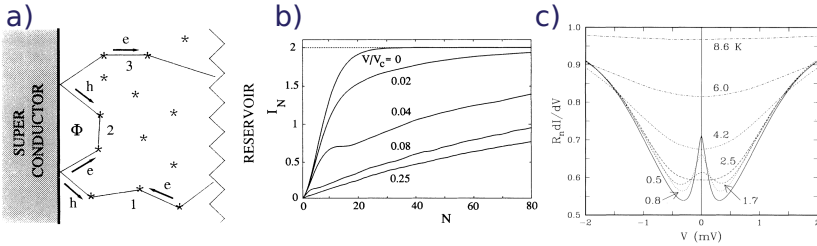

Figure 2.10. Reflectionless tunneling. a) Classical trajectories of electron (hole) being scattered close to the N-S interface. Trajectory 2 encloses a loop that receives a magnetic flux Φ. b) Current enhancement as a function of reflection number at N-S interface. Adapted from [112]. c) Normalized conductance vs voltage bias across a Nb-InGaAs structure for different temperatures. The zero bias peak is a consequence of reflectionless tunneling. Adapted from [113].

It turns out that the constructive interference is broken for increasing voltage bias, because of an increasing energy mismatch. This results in a zero bias enhancement of the current through an N-S interface. Such effect was first observed by Ref. [113] in a Nb-InGaAs structure. If the trajectories enclose a loop, if an external magnetic field B is applied there is a phase gain by the magnetic flux enclosed. Considering a trajectory length L and an enclosed area A of the loops, the total phase shift between two reflections is given by

$$\Delta\phi = \frac{2EL}{\hbar v_F} + 4\pi \frac{BA}{\Phi_0}. \tag{2.41}$$

Constructive interference happens for $\Delta\phi = 2\pi n$ with $n \in \mathbb{Z}$.

The result above assumes that the trajectories are not affected by the magnetic field. A simple picture discussing the semiclassical trajectories at finite magnetic fields is discussed in chapter 5 to address our experimental findings.

Reflectionless tunneling is also shown for ballistic systems as long as the geometry provides multiple reflections at the N-S interface [114].

2

3 Device Fabrication and Experimental Methods

This chapter describes the fabrication and characterization methods employed in 2D heterostructures. The first section shows how 2D crystals are obtained from bulk material by exfoliation. The stacking of heterostructures by dry transfer technique is depicted in the second section, followed by contacting techniques. The last section details the electric measurement setup and lock-in techniques employed. A detailed description of the fabrication steps and parameters is given in appendix A.

3.1. Fabrication of van der Waals heterostructures

The fabrication of vdW heterostructures consists of several processing steps that have been developed in recent years. Therefore, most of the processing is still manual and every sample has its features, e.g. flake shape and thickness, trapped impurities, etc. In this section, we demonstrate how to isolate thin layers from the bulk materials using the exfoliation technique. Although it is possible to grow 2D materials, for example using Chemical Vapor Deposition, the exfoliation from bulk 3D crystals is simple and yields high crystal quality for many-layered materials. We find the flake's thickness by comparing Atomic Force Microscope (AFM) scans of test samples with the color contrast in the optical microscope during fabrication. Then, we use the so-called dry-transfer technique to stack these materials into vertical heterostructures. As much as possible, the following processes are carried out in the inert atmosphere of a glovebox filled with purified N_2 (>99.9999%) and O_2 and H_2O residual partial pressures below 0.1 ppm.

3.1.1. Exfoliation of 2D crystals

Figure 3.1. Exfoliation of 2D materials. a) Bulk crystal is tapped on adhesion tape leaving some material. b) The crystal is cleaved several times, covering the tape with random thickness flakes. c) The tape is brought in contact with a silicon wafer, depositing some flakes on its surface. Adapted from [115].

As demonstrated for graphene in 2004, van der Waals materials can be mechanically exfoliated from a bulk crystal to a single atomic layer by successive cleaving [18]. Exfoliating vdW materials is possible because these crystals are formed by sheets of atoms bound in a plane by covalent bonds. These planes are vertically bound by vdW interaction, much weaker than the covalent bonds, favoring the cleaving in the in-plane direction. Exfoliating is achieved by pressing the bulk crystal against an adhesive tape leaving a fraction of the material sticking to the surface. By successively folding, sticking and releasing the tape the crystal is thinned down to a few layers. The tape containing residues of the material is pressed onto a silicon (Si) wafer and removed, leaving some flakes of various thicknesses on the wafer surface. The

exfoliation process is similar for all materials used in this work. The exfoliation of MoS_2 and InSe are preferably carried out in the glovebox, due to their oxidation and degradation when exposed to air. hBN and graphite can be exfoliated in air due to their high stability. A common issue faced with the exfoliation technique is the presence of polymer residues on the flakes. The gross can be identified with the optical microscope, but AFM scans show very low contrast contamination that cannot be noticed in a microscope. The next step is to identify the flake's thickness. This can be done directly with AFM scans, or indirectly by associating the thickness to another scale, such as Raman shift or Photoluminescence spectrum. A quick way to identify the flake thickness for a given material is by its color contrast in a standard optical microscope as used in the fabrication procedure. [116, 117]. The color contrast of each material depends on its thickness, its refractive index, and the properties of the substrate. Figure 3.2 exemplifies this by comparing the green channel intensity of an optical image to an AFM scan of the same region. In this example, the green channel was chosen for its monotonic increase (but not linear) with thickness of InSe from 1 to about 30 layers on a 290nm SiO_2 chip.

3.1.2. Dry-transfer method for stacking heterostructures

After acquiring flakes, and determining their thickness and area, the materials are ready to be stacked into a vertical heterostructure. Here we describe the dry transfer method [118], using a viscoelastic stamp to capture the flakes one by one from the exfoliation substrates. The setup is placed inside a glovebox to avoid degradation and contamination of the materials to be stacked. The stamps are made of Polydimethylsiloxane (PDMS) and covered with a sacrificial film of Poly (Bisphenol A) Carbonate (PC). The stamp fabrication is described in the appendix E. The dry transfer process starts by mounting the stamp with a small angle to a motorized arm inside the glove box. The stamp is placed between the microscope objective and the chip containing the material. The chip is heated to $90°$ C. The stamp descends to the substrate until it touches the surface. The contrast of the region in contact with the stamp changes, providing a good control of the area in contact. Once the desired flake is fully covered, by slowly retracting the stamp upwards the material flake detaches from the substrate stinking to PC film. The process can be now repeated for the next layers of the heterostructure. Once an initial flake sticks to the stamp, the consecutive flakes are attached by van der Waals force to the bottom of the previous. The final heterostructure is released onto a substrate by heating the substrate to $150°$ C which melts the PC layer onto the substrate surface releasing the stack. The melted PC film is removed in a Dichloromethane bath followed by a Isopropyl alcohol bath. Typically, the stack present in this work consists of the semiconductor material encapsulated
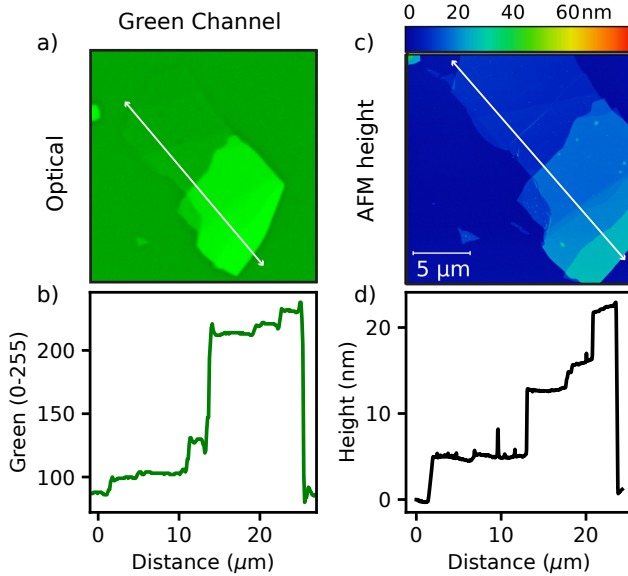
3

Figure 3.2. Color contrast vs flake thickness. a) Green channel of the optical image and b) Extracted green intensity (0-255). c) AFM height scan of the same flake and d) extracted height profile.

by ∼20-30 nm flakes of hBN. At the bottom of the stack, a graphite flake is placed as an electrical gate for the semiconductor. The hBN encapsulation is particularly known for protecting materials against oxidation and enhancing their electron mobility [119, 120]. Once the heterostructure is created, it is time to produce electrical connections to it. The following section describes the most common architectures for providing contacts to 2D materials.

3.2. Contacting architectures and materials for 2D semiconductors

There are several methods for producing electrical contact to 2D materials. Each has advantages and constrains. The selected technique for the device depends on the parameter to be optimized, e.g. electron mobility, interface cleanliness, contact resistance, or production time. This section describes the contacting strategies we employed in our samples.
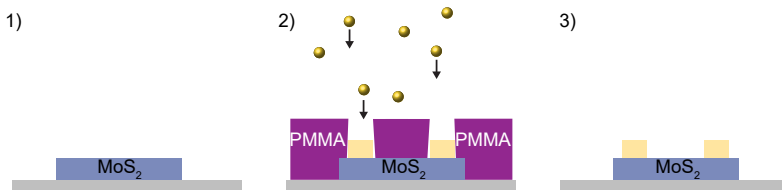
3.2.1. Top contact architecture

Figure 3.3. Top contacts fabrication. 1) Exfoliation of 2D semiconductor onto SiO$_2$. substrate. 2) EBL and contact material deposition. 3) Final structure after lift-off.

The simplest device fabrication is building devices directly on the exfoliation wafer by top contact architecture. The 2D semiconductor flakes are exfoliated onto a doped Silicon substrate with an insulating SiO$_2$ layer at the surface. The wafer is immediately spin-coated with PMMA polymer to temporarily protect the flakes from degrading. The flake thickness is identified by color contrast and a step of EBL defines the regions where the contacts are evaporated. After developing the E-beam-resist the sample is immediately mounted to the E-beam evaporation chamber and pumped down to pressures $\leq 10^{-6}$ mbar. The desired contacting materials are deposited and an acetone bath lifts off the excess material. As the devices are not encapsulated, after fabrication they must be quickly cooled to cryogenic temperatures to avoid degradation. We fabricated top contacted MoS$_2$ devices with several materials such as Bi-Au, Bi-Al, Sn, and Nb. The contact resistance can vary depending on the material of choice. For detailed information, see section 3.4. The mobility of these devices ranges from 100 to 700 cm^2/Vs at cryogenic temperatures. These numbers for electron mobility are expected for non-encapsulated 2D materials.

3.2.2. Bottom contact architecture

This architecture consists in fabricating the electrodes on a substrate and afterward depositing the active material onto it by dry transfer method. This architecture allows easy top hBN encapsulation. Full encapsulation can be achieved if the electrodes are evaporated onto a hBN flake previous to the stacking process [121]. We produced samples using bottom contact architecture for MoS$_2$ devices using several electrode materials such as Au, Pd, Al-Pd, and MoRe-Pt. The contact quality depends not only on the Schottky barrier but also on the cleanliness and surface topography. For metals that are E-beam evaporated (Au, Pd, Al) a good surface is easily achieved. For metals
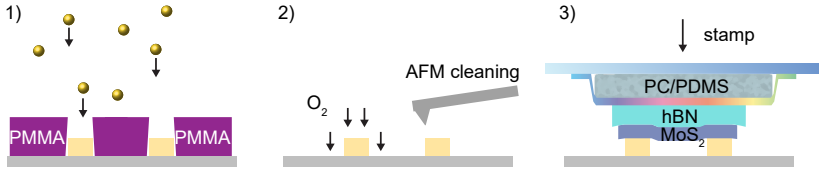
Figure 3.4. Bottom contacts fabrication. 1) EBL onto SiO_2 substrate and deposition the contact material. 2) Surface cleaning. O_2 plasma for e-beam evaporated materials and additional AFM cleaning for sputtered materials. 3) Transfer of the 2D semiconductor by PDMS/PC stamp.

that are sputtered, there is usually a side deposition at the undercuts of the PMMA, which creates a rugged contact surface. The latter can be improved by using an AFM cleaning [122]. Field effect gates are implemented by either the doped Si substrate or a posterior top-gate deposition. In our most remarkable device, with MoRe contacts to a monolayer MoS_2, we obtained resistance-area product as low as $13.5\,\mathrm{k}\,\Omega\,\mu\mathrm{m}^2$ and electron mobility up to $100\,\mathrm{cm}^2/\mathrm{Vs}$ [123].

3.2.3. Edge contact architecture
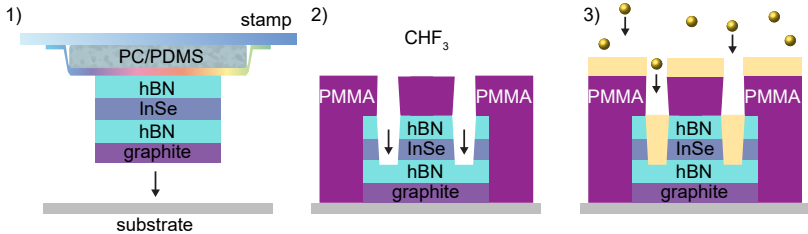
Figure 3.5. Edge contacts fabrication. 1) Heterostructure stack by dry-transfer method. The stack is released in a Si substrate. 2) CHF_3 plasma etching of the top hBN and 2D semiconductor. 3) Metal deposition and lift-off.

Originally developed for graphene [124], this architecture has been also successfully expanded to TMDCs such as WTe_2 [64]. The fabrication is depicted in Figure 3.5. Edge contacts are normally made in a hBN encapsulated heterostructure. The top hBN is etched away, in a CHF_3 plasma, to expose a lateral cross-section of the 2D material. The contact material is then deposited into the holes creating an electrical contact to the rims of the material.

Our attempts to produce edge contacts to mono- or few-layer MoS_2 generated devices with too high contact resistance for practical use [123]. Literature present other attempts [91, 125]. However, significant improvements were made recently [126].

We obtain better results with a few layers InSe devices with MoRe edge contacts. The measurements are discussed in chapter 6. At $V_{BG} = 18\,\mathrm{V}$ we estimate a contact resistance-length product of about $3\,\mathrm{M\Omega\,\mu m}$, which is a high value in comparison to other contact techniques shown in this work but presents similar physics as the one discussed in Chapter 5.

3.2.4. Van der Waals contacts

An interesting solution to reduce the Schottky barrier is to use another vdW material as contacts to the semiconductors. The attractive vdW force provides a natural connection between the flakes, yielding a clean interface for contacts. This is realized, for example, by placing graphene flakes at the extremities of a MoS_2, as in Ref. [120, 127, 128]. As graphene by itself is easy to contact, it can provide good charge injection to the semiconductor. This type of devices show very low contact resistance and high mobility. The same technique has also been used for other vdW semiconductors, such as InSe [49] and WSe_2 [129]. We create a short MoS_2 junction contacted by the vdW superconductor $NbSe_2$. The dry transfer technique does not provide enough resolution to create sub-micrometer junction lengths between $NbSe_2$ flakes. Designing a trench in a $NbSe_2$ is challenging since the material is prone to oxidation when exposed to air [130]. We overcome this issue by covering a thin $NbSe_2$ flake in a monolayer graphene. These two are stacked and deposited onto Au electrodes in a Si substrate. An EBL step followed by reactive ion etching creates a trench in $NbSe_2$/graphene. Afterward a monolayer MoS_2 covered by a top hBN is deposited above the trench, creating a 150nm junction between $NbSe_2$/graphene flakes. An Au topgate is evaporated above the junction for charge carrier tunability. These results were published in Ref. [123]. We demonstrate that after the processing, $NbSe_2$ still holds intrinsic superconductivity, showing that the graphene protects the $NbSe_2$ underneath against strong oxidation. No sign of proximity-induced superconductivity or tunneling through N-S interface with low transmission is observed across the MoS_2 junction. Instead, a suppression in conductance tentatively attributed to environmental Coulomb blockade with weak magnetic field dependence is observed. The contact resistance-area product is estimated $\sim 200\mathrm{k\Omega\,\mu m^2}$.

3.2.5. Vertical interconnect access contacts

Vertical interconnect access (VIA) contacts use the hBN encapsulation to provide electrical contact to the thin semiconductor material without exposing it

to chemical treatments. The metallic leads are deposited into the hBN flakes providing a flat and clean interface between metal and semiconductor. The name is imported from printed circuit boards and coined by Ref. [131] when adapting to vdW materials in 2018. The fabrication of the VIA contacts is described below and depicted in Figure 3.6.
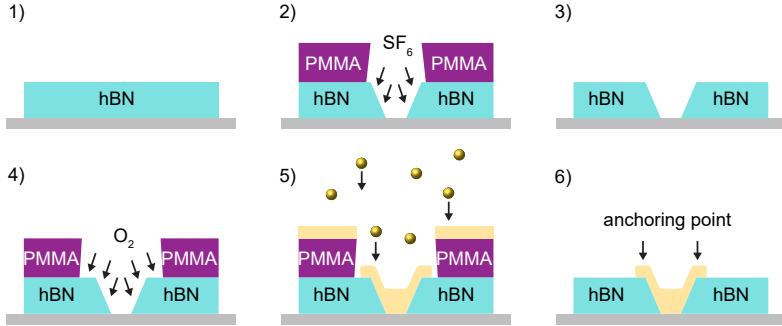

Figure 3.6. Schematic fabrication of the VIA contacts. 1) Exfoliation and characterization of the hBN flake. 2) Etching holes into hBN using SF_6 plasma etching. 3) Wash-off PMMA and second step of lithography. 4) Surface cleaning with O_2 plasma etching. 5) Metal evaporation and lift-off. 6) hBN is taken to dry transfer technique.

An hBN is exfoliated onto a silicon substrate and selected for sufficient area, thickness, and cleanliness. The wafer is spin-coated with PMMA polymer and a step of EBL defines windows that expose the hBN surface. A sulfur hexafluoride (SF_6) plasma etches the hBN flake until the substrate is reached. The PMMA is washed out and a second step EBL defines areas slightly larger than the former. This is done to allow metal to deposit at the surface of hBN serving as anchor points to the VIA contacts. The surface of the sample is cleaned by O_2 plasma etching. The next step consists of depositing the desired metal, that being Au or MoRe, etc. The excess metal is removed in an acetone lift-off. The result is metal columns that penetrate the hBN flakes until the SiO_2 surface. With that, the VIA contacts are ready to be peeled out using the dry transfer technique described above. The semiconductor is put in direct contact with the metal columns by the van der Waals force induced between the flakes. After completion of the stack, metallic leads connect the VIA metal columns to the bond pads, where the sample can be contacted. We attempted several contacting materials for the VIA architecture, namely Au, MoRe, Al, Nb and V. Most of them turned out to be impractical for either being too brittle and cracking the metal column while being pick-up or

pinning too strongly to the substrate. We successfully use Au and MoRe in ten MoS$_2$ or InSe devices. Electron mobility up to $2500\,\text{cm}^2/\text{Vs}$ and resistance area product down to $14\text{k}\,\Omega\,\mu\text{m}^2$. Samples fabricated using VIA contacts are the main subject of Chapter 5.

3.3. Measurement setup

Most of the experiments realized in this work use a standard lock-in technique to probe the conductance or current through the devices. The common measurement setup is depicted in Figure 3.7. A sinusoidal voltage is provided by the output of a lock-in amplifier which is then coupled to a DC voltage source through a transformer. The voltage is usually lowered in the voltage divider filtered for voltage ripples in a pi-filter. This excitation is applied to the source side of the device. At the drain side, the current is amplified by an IV converter and supplied to the input of the lock-in and DC multimeter. The gate channels are also filtered before being supplied to the device gate(s). In a four-terminal configuration, one can overcome the contact resistance by directly probing the voltage drop of the system. This is done by adding a differential voltage amplifier connected to the terminals to be measured and provided its output to a (second) lock-in amplifier.
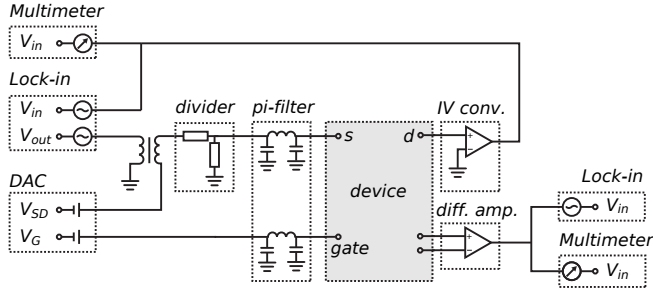
Figure 3.7. Summarized schematic of the measurement setup. Values of single components may vary according to experiment and were omitted.

3.4. Semimetal contacts to MoS$_2$

Besides the contacting architecture the second crucial point for contacting 2D semiconductor is choosing the correct material for the leads. For the purpose of this work we are interested in superconducting leads, but an effective way to reducing the Schottky barrier has been shown recently by Ref. [74] and

[79], where they use semimetal as contacts which are approaching the quantum limit of resistance in field effect transistors. Semimetals have a reduced density of states around the Fermi level. As discussed in section 2.2.3, one of the mechanisms for creating a Schottky barrier to 2D semiconductors is by inducing MIGS in the band gap of the semiconductor. If these MIGS have a considerable density of states, they are partially occupied, pinning the Fermi energy to the gap. When in close contact to MoS_2 the reduced density of states around the Fermi level in the semimetal diminishes the formation of MIGS, pushing the Fermi level up to the bottom of the conduction band of MoS_2. The few gap states present in MoS_2 are fully occupied raising the Fermi level pinning close to the conduction band minimum, as shown in Figure 3.8 c).
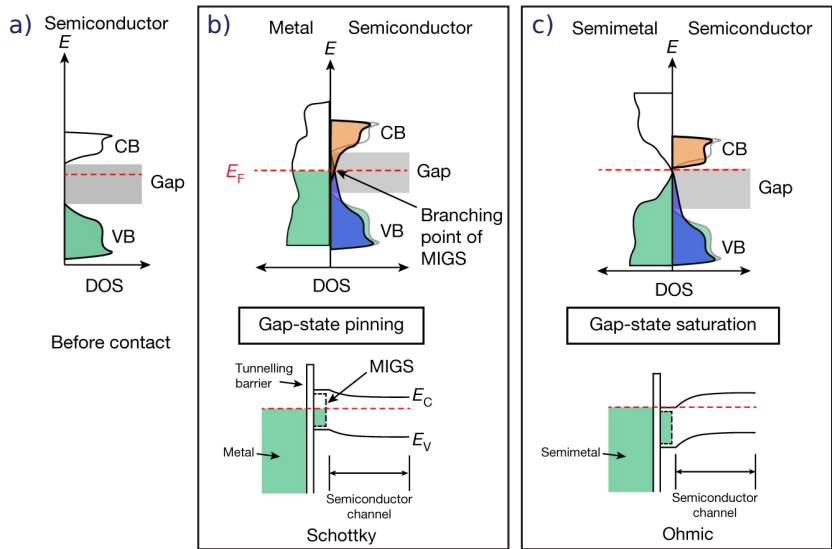
Figure 3.8. Schematics of density of states for a) semiconductor in the absence of interface with other materials. b) Metal-semiconductor interface. The density of states in the semiconductor is altered due to proximity to metal, generating MIGS, which are partially occupied. The Fermi level is pinned at the band gap to the branching point between MIGS originating from VB and CB. c) Semimetal-semiconductor. The semimetal density of states diminishes the formation of MIGS, which brings the Fermi level to the bottom of conduction band. Adapted from [74].

Another aspect of realizing ohmic contacts is to overcome the van der Waals gap formed between contact and semimetal. Ref. [79] has computed that

semimetallic antimony Sb (0112) hybridizes with the orbitals from MoS$_2$ such that the p and s orbitals of Sb intersect with the d orbitals of Mo. Reducing this physical gap between materials optimizes the charge injection into the 2D semiconductor reducing the resistance-length product to $42\,\Omega\,\mu$m, approaching the quantum limit of a metal-semiconductor junction, defined by

$$R_{QL} = \frac{h}{2e^2}\sqrt{\frac{\pi}{2n}} \tag{3.1}$$

with n the charge carrier density. This limit assumes ballistic transport of charges with coherent transport across the interface without back-scattering. Engineering of InSe into a semimetallic phase by yttrium doping has also achieved resistances close to the quantum limit [51].

To reproduce the results shown in Ref. [74], we fabricated top contacted monolayer MoS$_2$ devices with Bi/Au leads. A monolayer MoS$_2$ is exfoliated directly onto a doped Si substrate with 80 nm SiO$_2$ layer and immediately spin-coated with PMMA resist. Contact leads are patterned by EBL and after developing the resist the sample is immediately mounted to an E-beam evaporator and pumped to 10^{-7} mbar. A film of 20 nm bismuth is evaporated at $0.5\,\text{Å/s}$, followed by 60 nm Au. The lift-off of the excess material is done in a 50° C acetone bath. We note that bismuth is wetting SiO$_2$ badly, so an additional Ti/Au (5 nm/80 nm) is needed to create bondpads. The sample was wire bonded, mounted to a dilution refrigerator, and cooled down to 60mK.

At maximum gate voltage, with $n \sim 2 \times 10^{12}\,\text{cm}^{-2}$, we obtain a resistance-length product of $15\text{k}\,\Omega\,\mu$m or $7\text{k}\Omega\,\mu\text{m}^2$ resistance-area product. These values are two orders of magnitude higher than reported by Ref. [74], but still one of the lowest among our devices. From 14 samples fabricated[1], we obtained a spread of values, shown in Figure 3.9, with only one sample approaching the literature value[2]. This shows that the results are not easily reproducible. Ref. [79] reports improved reproducibility for Sb (0112). We note that better Bi films are obtained by cooling the sample to liquid nitrogen temperatures during the material evaporation.

We exploit the Schottky barrier lowering caused by semimetallic bismuth to create short S-N-S junctions. The idea is to use semimetallic Bi as a wetting layer for superconducting contacts. We employ top contact fabrication as described above, replacing Au with 100 nm Al layer followed by 10 nm Pd capping layer. The following measurements were realized using standard lock-in technique at 50 mK.

First, we make sure that the Al contacts are superconducting at low temperature. For that, we probe the voltage drop across the superconducting leads as a function of the magnetic field. By applying a constant current of $I = 1\,\mu$A to one of the sides of the lead and grounding the counterpart, we measure the

---

[1] Including Bi-Au and Bi-Al contacts
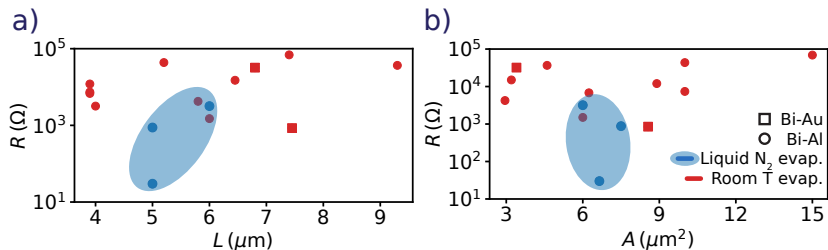[2] Ref. [74] present results at 77 K.

Figure 3.9. Resistance as a function of a) length and b) area of the Bi contacts to MoS_2. The Bi-Au samples are indicated, the other are Bi-Al samples. The red and blue shades indicate room temperature and liquid nitrogen temperature film evaporation respectively.

voltage drop and translate it to the resistance of the lead in the inset of Figure 3.10. Discounting for the series resistance in the cryostat, we observe a $3\,\Omega$ increase in resistance around $|B| \sim 4\,\text{mT}$. This is compatible with the critical field of bulk Al [132], demonstrating superconductivity in the Al leads.

Figure 3.10 a) shows the conductance of the MoS_2 channel as a function of the backgate voltage V_{BG}. At maximum $V_{BG} = 45\,\text{V}$ we obtain a two-terminal resistance of $600\,\Omega$, the best among the devices fabricated in this project.

Though the contact resistance was lowered, no sign of proximity-induced superconductivity was observed. Figure 3.10 b) shows the conductance as a function of the applied bias voltage. Around zero bias a sharp suppression is observed much narrower than the energy values expected of Al superconducting gap [133]. Also, the suppression is persistent up to 9T magnetic field. We tentatively attribute the suppression to the diminished density of states in the semimetal. In Figure 3.10 b) we also plot the four terminal resistance through the sample. Considering $R_T = 2R_C + R_{2DEG}$ we can extract the contact resistance, yielding $150\,\Omega\,\mu\text{m}$ or $200\,\Omega\,\mu\text{m}^2$.
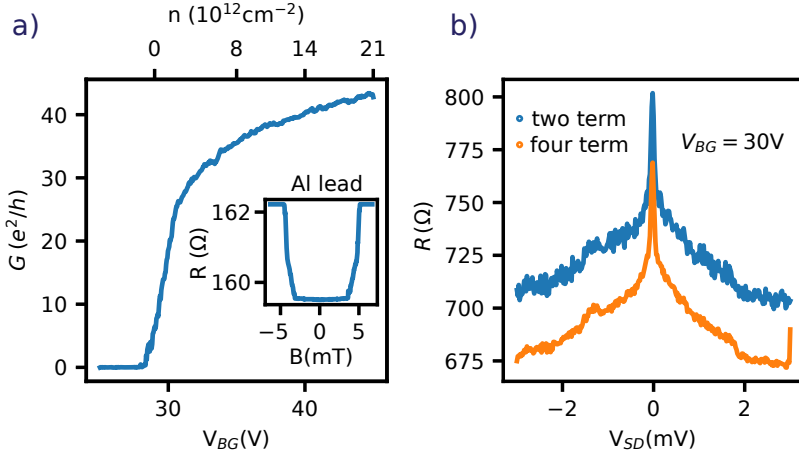
Figure 3.10. Bi-Al contacts to MoS_2. a) Conductance as function of V_{BG}. The charge carrier density axis is calculated using a plate capacitor model. The inset shows the resistance of one of the superconducting leads as a function of perpendicular magnetic field B. b) Resistance as function of V_{SD} measured between two and four terminal configuration.

3.5. Summary

We explore several fabrication architectures, contacting materials, and device geometries. Device architectures such as VIA, edge- and vdW contacts are well suited to retain the high electron mobility because the hBN encapsulation can be employed. Top contacts are easy to fabricate but suffer from polymer residues and degradation of the 2D material. Although interesting for some materials, we did not achieve low contact resistances with edge contacts. We employ several contacting materials searching for optimizing the Schottky barrier formation, which we believe, is the main reason we observe no proximity effect in our devices. We also demonstrate semimetallic contacts to 2D semiconductors showing contact resistances approaching the quantum limit. We fabricate devices using semimetallic bismuth as a wetting layer for Al superconducting contacts. Although a substantial decrease in resistance was achieved compared to other materials, we did not observe any signs of superconducting effects. We speculate that Bi might cause a strong inverse proximity effect by a strong spin-orbit interaction given by its high atomic number. Figure 3.11 summarizes the resistance-area and length product for the methods and materials employed in this work. For multiple samples of the
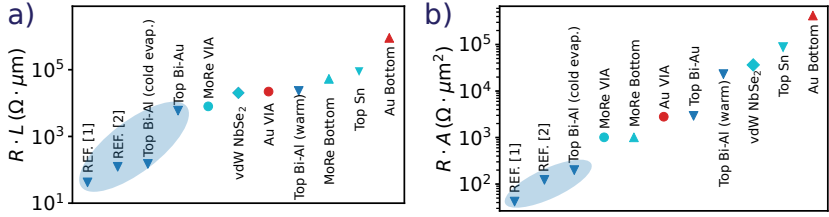
Figure 3.11. a) Resistance-length product and b) Resistance-area product of MoS$_2$ devices in this work and [123], compared to the records in literature [74, 79]. Color code is dark blue for semimetals, light blue for superconductors, and red for metals. Symbol code is $\triangledown$ for top contacts, $\bigcirc$ for VIA, $\triangle$ for bottom contact, and $\diamond$ for vdW contacts.

same type, we select the ones with the lowest resistance. All the values were obtained for temperatures at least below 1.7 K.

4 Quantum Point Contact in monolayer MoS$_2$
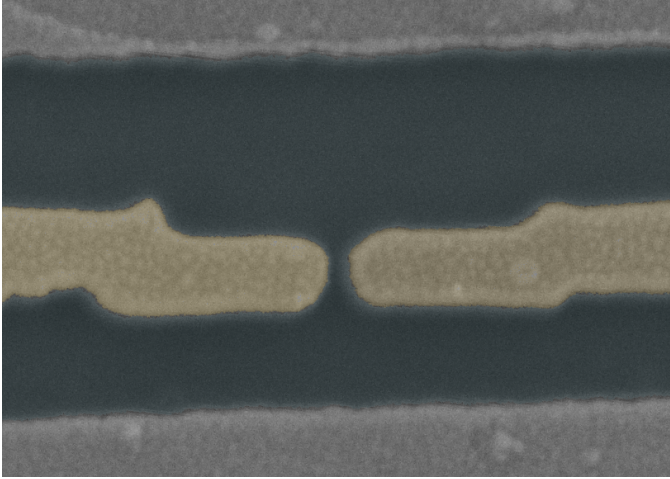
Phenomena involving gate-defined nanostructures have been investigated for many decades and still bring out innovative results [134]. Implementing lateral confinement in TMDCs such as MoS$_2$ could provide control over charge, spin, and valley states which is promising for future experiments and applications [38]. In this chapter, we study the transport through a small constriction generated by locally gating a monolayer MoS$_2$. We demonstrate that this constriction forms a well-defined quantum point contact (QPC) by quantization of the conductance through the channel in multiples of $2 \times e^2/h$. Our measurements also present indications of a 0.7 anomaly known in QPC devices. The energy spacing between QPC states allows us to reach conclusions about the confinement potential shape. Applying an external magnetic field perpendicular to the sample we analyze the evolution of the plateaus due to Zeeman splitting and further into quantizing fields.

4.1. Introduction

Quantum point contacts are the primary gate structure to demonstrate local gate control in a two-dimensional system. These constrictions have many applications in nanoelectronic devices. In ballistic systems, QPCs represent an interesting point emitter, with an emission profile dependent on the mode occupation [135]. They can also be used as charge detectors in proximity to a quantum dot [136], as beam splitters [134], as spin filters [137], to investigate spin-orbit coupling [138] or for controlled carrier wave package injection [139]. Their characteristic have also been studied in shot noise measurements [140], thermoelectric transport [141], opto- [142] or magnetotransport [143]. When in a proximitized region, QPCs can be used as a spectroscopy tool to probe the superconducting states [144, 145]. Despite all these possibilities, there are only a few reports exploring QPC in 2D semiconductors, with little exploration of its prospects [127, 128, 146–148]. Here we report the fabrication and characterization of a QPC to a monolayer MoS$_2$, discussing the electrostatic environment involved in the channel formation and its characteristics in energy and magnetic field.

4.2. Fabrication

The sample consists of a monolayer MoS$_2$ encapsulated in hBN flakes and top contacted by Bi-Au electrodes. We start the fabrication by exfoliating and selecting a clean hBN flake of ~ 20 nm thickness. To this flake, an EBL step defines holes that will be used to electrically contact the sample. An SF$_6$ reactive plasma etches down the hBN until the SiO$_2$ substrate is reached. The flake is transferred to the glovebox, where MoS$_2$ is exfoliated to a monolayer and identified by color contrast. Using the dry transfer technique, the monolayer MoS$_2$ is sandwiched between hBN flakes. The etched hBN flake is placed at the top of MoS$_2$ leaving exposed to the contacts. A multilayer graphite at the bottom of the stack is used as a global backgate. The stack is released onto a SiO$_2$ substrate. Figure 4.1 a) shows an optical image of the sample. Figure 4.1 shows a vertical cross-section of the heterostructure indicating the thickness of flakes obtained by AFM scans.

After the stacking process, the PC film is removed in a dichloromethane bath, followed by an IPA bath. The sample is blown dry and immediately spin-coated to avoid long exposure of the MoS$_2$ surface to the atmosphere. An EBL step defines PMMA windows around the holes in hBN. The resist is developed and the sample is transferred to the evaporation chamber and pumped to 10^{-6} mbar. A layer of 20 nm Bi is deposited at the steady rate of 0.5 Å/s followed by 50 nm Au capping layer. The excess material is lifted-off in an acetone bath. A second EBL step defines the splitgate structure, leads to graphite backgate, and to Bi-Au contact. Those are created by evaporation of
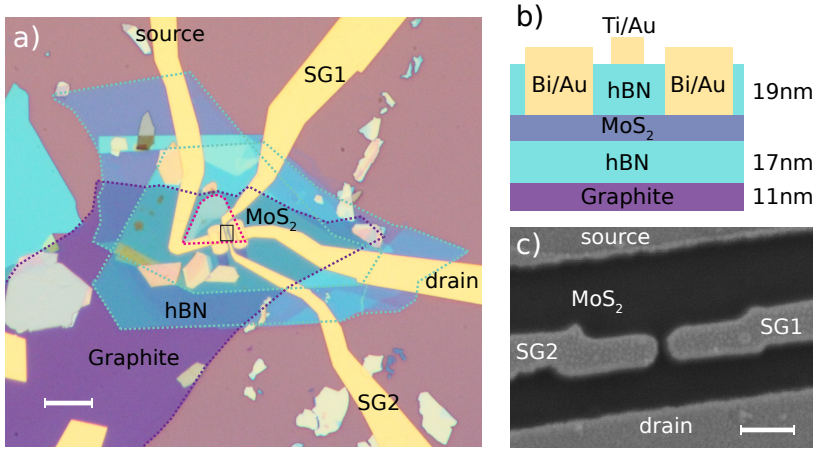
Figure 4.1. a) Optical image of the sample, showing the flakes limits, contacts, and splitgates deposited at the surface in yellow. The scale bas is $10\,\mu$m. b) Schematic of a vertical cross-section of the heterostructure. The flake's thicknesses are indicated at the right of the stack. c) Scanning electron microscopy scan of the splitgate region. The scale bar is $200\,$nm.

$5\,$nm Ti plus $80\,$nm Au. The tips of the splitgates are designed to have $100\,$nm circular radius, and $70\,$nm spacing, as shown in Figure 4.1 c). A length of about 1μm separates the center splitgate from contacts leads. Finally, the sample is glued to a chip carrier, wire bonded and mounted to a dilution refrigerator and pumped for $12\,$hs. This helps to remove water molecules adsorbed to the surface. The measurements described below are performed at the base temperature of $40\,$mK.

4.3. Sample characterization

We first characterize the sample without the presence of the splitgate potential. By applying a sinusoidal source-drain voltage added to a constant voltage $V_{SD} = 0.25\,$mV we measure the differential conductance and DC conductance as a function of V_{BG} applied to the graphite backgate. Figure 4.2 a) shows the conductance of the sample as a function of the backgate voltage V_{BG}, applying the same voltage to the splitgates. A sharp increase in conductance is observed from $V_{BG} = 0.5\,$V, which saturates at $V_{BG} \sim 1.5\,$V to a flat slope around $0.65 \times e^2/h$, marked as region A and B, respectively. The
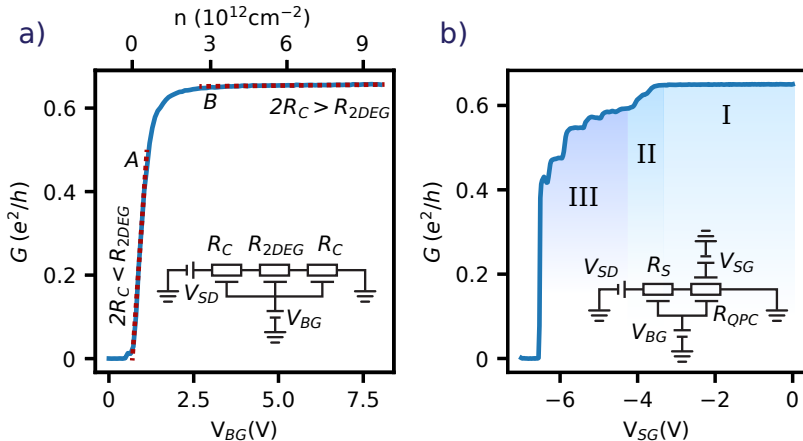
Figure 4.2. a) Conductance as a function of backgate voltage V_{BG}. b) Conductance as a function of splitgate voltage V_{SG} at V_{BG} =3.4 V. Three regions are discussed in the text.

charge carrier concentration axis is calculated from a parallel-plate capacitor model with depletion voltage $V_{BG} = 0.5$ V. We model the system as shown in the inset of Figure 4.2 a). The 2DEG resistance R_{2DEG} is placed in series with two contact resistances R_C at the source and drain. At region B, V_{BG} >2 V, we extract a slope of about $50\,\Omega/V$. At the maximum backgate voltage V_{BG} =8 V, we assume $R_S \gg R_{2DEG}$ to extract a upper bound for the contact resistance as $R_C \sim 19\,\mathrm{k\Omega}$. This contact resistance is severely higher than the previously measured for the Bi-Au FET as in section 3.4. The reason might lay in the exposure of the monolayer MoS₂ to sacrifice the PC film of the stamp and dichloromethane after the stacking phase, which can induce defects and impurities at the interface. In region A, we assume that R_{2DEG} is the dominating resistance to extract a field effect mobility from the linear part of the slope, yielding μ_{FE} =1150±100 cm²/Vs. This value is comparable to other encapsulated monolayer MoS₂ devices [39, 149] and to the estimation from the magnetic field dependence (see appendix A). A mean free path can be estimated by taking v_F from the plate capacitor model. For example at $V_{BG} = 3.4$ V, we obtain $\ell_{\mathrm{mfp}} \sim 45\,\mathrm{nm}$.

Now we turn to the QPC formation in the 2D channel by applying a negative voltage to the splitgates. Figure 4.2 b) shows the measured conductance through the sample as a function of the splitgate voltage V_{SG} at V_{BG} =3.4 V. We observe three distinct regions. For V_{SG} from zero to −3.5 V (region I) a slow decrease in conductance occurs. A transition marked by a sharp reduc-

tion of $\sim 10\%$ in conductance occurs at $V_{SG} \sim -3.5\,\mathrm{V}$, identified as region II. In region III, as stronger negative voltages are applied to the splitgate the conductance continues to decrease forming step-like features, until total depletion, at $V_{SG} = -6.5\,\mathrm{V}$.
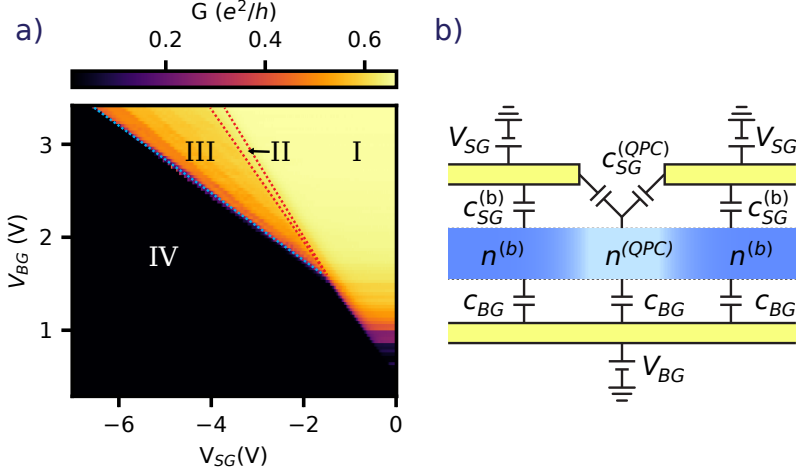

Figure 4.3. a) Conductance as a function of V_{SG} and V_{BG}. b) Schematic of the vertical cross-section showing a capacitor network model between gates and regions of MoS_2.

Changing the backgate voltage alters the characteristics of the QPC pinchoff curve. Figure 4.3 a) shows the conductance as a function of V_{SG} and V_{BG} at $V_{SD} = 0.25\,\mathrm{mV}$. The bright areas represent a finite conductance, with aforementioned regions I to III. At the dark sites, the transport is blocked by the depleted QPC (IV), while the rest of the 2DEG is still open. For $V_{BG} > 1.5\,\mathrm{V}$ we see the formation of quantized plateaus in region III. For V_{BG} below this value, there is a direct transition from open 2DEG (I) to depleted (IV). The region within the red dotted lines represents region II.

We can qualitatively understand the slope structure of this plot using a simple capacitor model, depicted in Figure 4.3 b). The chemical potential $\mu^{(b)}$ directly below the splitgates is given by

$$\mu^{(b)} = en^{(b)} = c_{BG}\Delta V_{BG} + c_{SG}^{(b)}\Delta V_{SG}, \tag{4.1}$$

where the gate voltages $\Delta V_{BG,SG}$ is the difference to respective depletion voltages and c_{BG} and $c_{SG}^{(b)}$ are the capacitances of the back- and splitgates to

the region directly below the splitgates (dark blue regions). The position of feature with a fix $\mu^{(b)}$ in Figure 4.3 a) is then given by

$$\Delta V_{BG}(\Delta V_{SG}) = \mu^{(b)} - \frac{c_{SG}^{(b)}}{c_{BG}} \Delta . V_{SG}. \qquad (4.2)$$

where the ratio of capacitances $c_{SG}^{(b)}/c_{BG}$ is roughly the ratio the dielectric thicknesses $d_{bhBN}/d_{thBN} \sim 0.8 \pm 0.1$, matching the slope ~ 0.77 of the right red dotted line.

The region between the splitgates, i.e. light blue region in Figure 4.3 b) is only reached by stray electric field lines. This means that the splitgate capacitance to this region must be smaller then the regions directly underneath it. Explicitly, we can write $c_{SG}^{(QPC)} < c_{SG}^{(b)}$. Considering that the backgate capacitance c_{BG} is unchanged, we could write equation 4.2 for the region between the splitgates leads obtaining a smaller slope for the ratio $c_{SG}^{(QPC)}/c_{BG}$. From the slope of the blue line in Figure 4.3 a) we obtain $c_{SG}^{(QPC)}/c_{BG} \sim 0.4$, which is consistent with this model.

For $V_{BG} < 1.5\,\text{V}$ the system goes from region I to IV without showing quantized plateaus. This implies that the potential formed between splitgates is too shallow, e.g. in equation 2.22 if ω_y/ω_y goes to zero, the plateau width goes to zero.
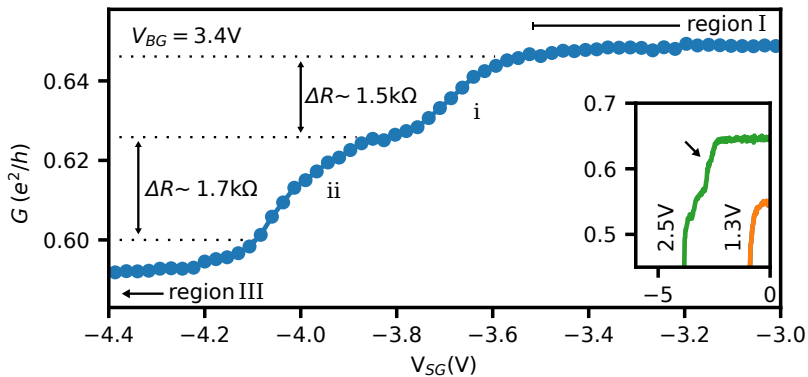

Figure 4.4. Zoom in region II of conductance as a function of V_{SG} at $V_{BG} = 3.4\,\text{V}$. Two consecutive decreases in conductance are identified. Inset shows the pinch-off curve for two other backgate voltages indicated. For $V_{BG} = 1.3\,\text{V}$ the shoulders are not observed above the noise level. The inset has the same axis as the main figure.

4.4. Region II: Current redistribution and Sharvin resistance

Figure 4.4 shows a zoom-in region II of the splitgate voltage dependence. Starting from $V_{SG} = -3$ V, an initial drop takes place at $V_{SG} = -3.5$ V, decreasing the conductance from $0.65 \times e^2/h$ to $0.63 \times e^2/h$. Then, a shoulder is formed followed by further decreasing to $0.60 \times e^2/h$. This two-step decrease is observed for all backgate voltages where region III is also visible.
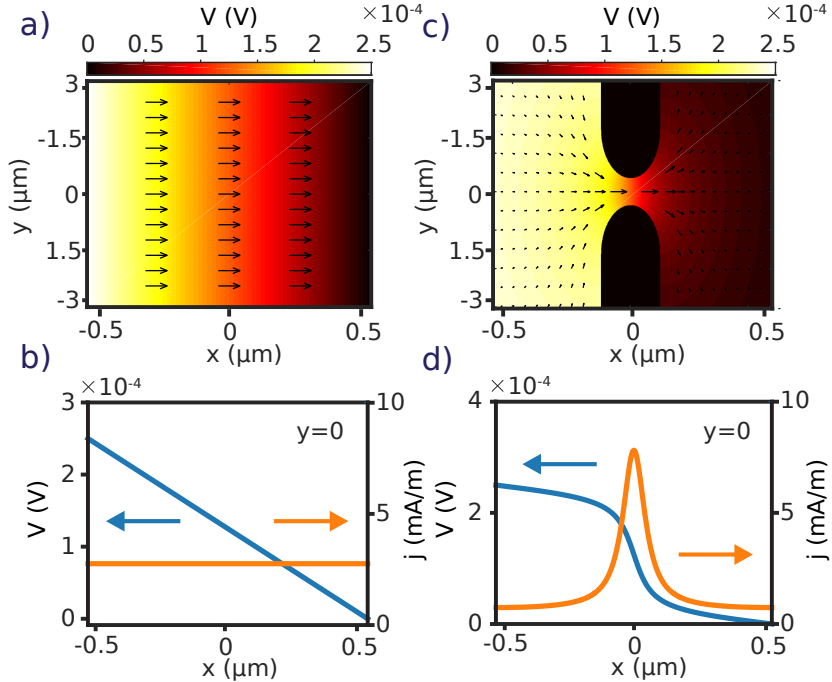
Figure 4.5. Simulation of diffusive system. a) Electrical potential and current density (arrow) for an open conductor. b) Cross section of a) at $y = 0$. c) Electrical potential and current density (arrow) for the conductor with constriction given by the geometry of the splitgates. d) Cross section of c) at $y = 0$.

We tentatively attribute these two steps to: i) an initial redirection of the current distribution in the 2DEG when the constriction is formed, i.e. when the 2DEG region below the splitgates is depleted. At this stage, the 2DEG and the constriction region are still in the diffusive transport regime. ii) The transition from a diffusive to ballistic transport in the QPC so that the resistance of the

diffusive constriction region is replaced by a Sharvin resistance.

To illustrate the change in conductance due to the geometrical current re-distribution, we simulate[1] the electrical potential and the current density of a fully diffusive system characterized by a local resistivity. Figure 4.5 a) shows a uniform decrease in electrical potential and constant current density. Once the splitgates depletes the 2DEG the current is redirected to flow through the constriction, as depicted in Figure 4.5 b). The electrical potential and the current density along a cross-section at $y = 0$ for these two cases are plotted in Figure 4.5 c) and d). The values for resistivity are taken from the conductance at $V_{BG} =8$ V and $V_{SG} =0$ and the estimated area of the MoS$_2$ flake. The boundary conditions for the potential are set by the applied DC bias $V_{SD} =250 \mu$V.

From the mobility estimated above and the charge carrier density $n \simeq 3.5 \times 10^{-12}$cm^2/Vs calculated from the plate capacity model at $V_{BG} =3.4$ V, we obtain the sample resistivity without the splitgate influence. The increase in resistance given by the first shoulder, $\sim$1.2 kΩ corresponds to a decrease in width from $\sim$3 μm (active MoS$_2$ width) to 70 nm (design splitgate size) over a length of about 30 nm.

To describe the ballistic case, while the channel is larger than the Fermi wavelength avoiding discrete quantum states in the constriction, we assume that the second increase in resistance as a Sharvin resistance R_{Sh} that is given by [150]

$$R_{Sh} = \frac{\pi h}{2e^2 k_F w} \tag{4.3}$$

yielding $R_{Sh} \sim 1.3$ kΩ for $w =70$ nm and k_F calculated by plate capacitor model at $V_{BG} =3.4$ V, consistent with a resistance Sharvin mechanism [151].

These two pieces of information lead us to speculate about the first decrease in conductance being caused by a geometrical redirection of the current, which saturates after the constriction is formed giving rise to the first shoulder. The second decrease takes place as the channel becomes smaller than ℓ_{mfp}, due to Sharvin resistance. Up to the moment of publication of this work, we became aware of other possible mechanisms that could lead to the two steps described above. Unfortunately, no strong proof ruling out one mechanism from the other is yet available.

4.5. Region III: Series resistance extraction and quantized conductance plateaus

In region III we find quantized conductance plateaus, as reported very early on for GaAs [92, 93]. However, taking a closer look at the actual conductance

---

[1]Using MATLAB partial differential equation (PDE) solver.

values, one finds that they are not given exactly by an integer multiple of e^2/h. This makes it necessary to find an independent way to subtract a series resistance to identify the plateaus and the corresponding degeneracies. For this purpose, we extract a series resistance such that the QPC conductance is

$$G_{QPC} = \left(\frac{1}{G_{tot}} - R_S\right)^{-1}. \tag{4.4}$$

The increment in conductance from one plateau to the next is related to the number of degenerate subbands in the 2DEG. Ref. [128] suggests conductance increments in steps of e^2/h, implying a lift of the spin and valley degeneracies in MoS_2. However, these results depend strongly on the extracted series resistance. In the literature, it is common to take the open 2DEG resistance (without the splitgate influence) as the series resistance. However, this approach disregards the increase in the resistance due to a redirection of current density as the region below the splitgates is depleted as discussed above.
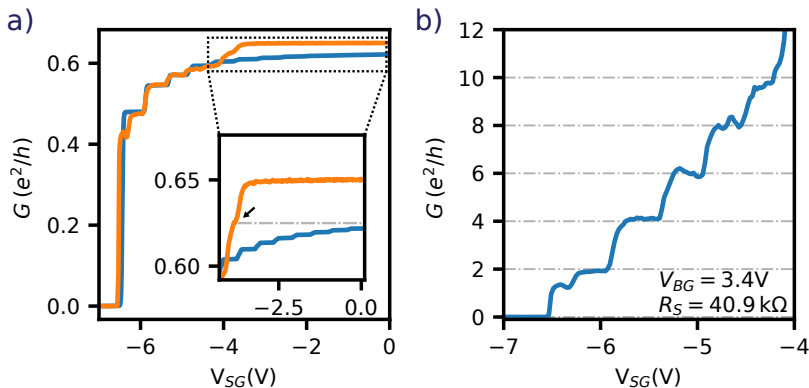

Figure 4.6. a) Conductance of model (Blue) in comparison to measured data (orange) as a function of V_{SG}. The inset shows how the saturation conductance $1/R_S$ matches region II. b) Corrected conductance of the QPC as a function of V_{SG} showing plateaus of $2 \times e^2/h$.

To clarify the effect of the series resistance on the QPC pinch-off curve we plot in Figure 4.5 a) the calculated conductance for a parabolic potential from equations 2.22 and 2.23, using $\hbar\omega_x = 0.66\,$meV, $\hbar\omega_y = 0.53\,$meV. We compare the model to the measured conductance from Figure 4.2 b). We find a series resistance of $R_S = 40.9\,$kΩ causing a conductance saturation to $G_S = 1/R_S$. This value is reached as long as the QPC has sufficient channel occupation, being independent of the number of subbands or degeneracy contributing to

transport. Using this analysis to extract the series resistance R_S we plot Figure 4.6 b) of the corrected QPC conductance as a function of slipgate voltage. Quantized plateaus of conductance with increments of $2 \times e^2/h$ are obtained, corresponding to a degeneracy of two. We also point out the presence of a shoulder at around $1.4 \times e^2/h$ which we tentatively attribute to 0.7 anomaly known in QPCs [152]. Other examples are shown in appendix A. We observe plateaus up to $5 \times 2e^2/h$ at maximum $V_{BG} = 3.9$ V. Small fluctuations in the conductance plateaus could arise due to mode mixing, away from the adiabatic approximation, or the presence of defects in the proximity of the constriction, as discussed in 2.3.

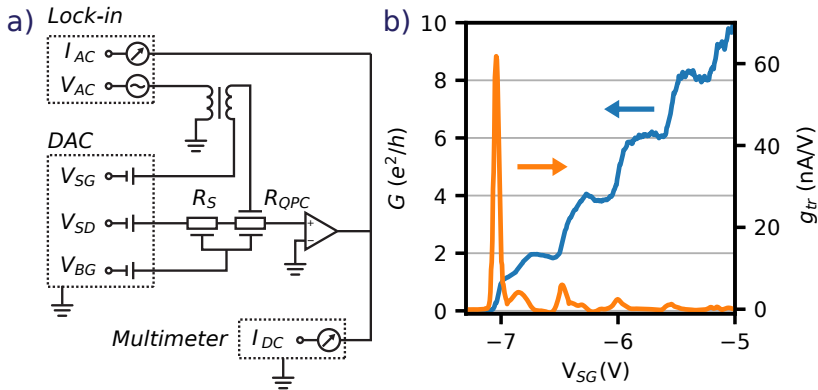## 4.6. Transconductance measurements

Figure 4.7. a) Measurement setup for transconductance. b) Conductance and transconductance as a function of V_{SG} at $V_{BG} = 3.9$ V.

To increase the sensitivity of the measurements to variation in the conductance caused by changes in the QPC potential, we measure the transconductance defined by

$$g_{tr} = dI/dV_G \tag{4.5}$$

where I is the current through the semiconductor and V_G the voltage applied to the gate. The transconductance is zero for conductance plateaus, and it has finite values if the conductance changes with respect to the gate voltage applied. The measurement setup for transconductance is shown in Figure 4.7 a). A sinusoidal voltage modulation provided by a lock-in amplifier is added

to the DC voltage in a transformer and supplied to the splitgates. The sample is biased with a DC voltage source ($V_{SD} =250\,\mu$V). At the drain, the DC and differential component of the signal are measured. The sinusoidal modulation is adjusted to an optimal frequency ($f =7.77$ Hz) such that the out-of-phase component of the signal can be neglected.

From the in-phase current modulation, we obtain the transconductance (in units of A/V) divided by the amplitude of the voltage modulation to the splitgate. Figure 4.7 shows the QPC conductance and the measured transconductance as a function of the splitgate voltage V_{SG}.
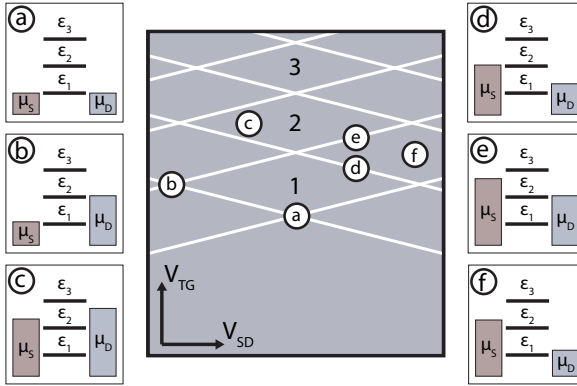

Figure 4.8. Schematic of transconductance as a function of the bias voltage applied to the QPC and splitgate voltage. The white lines represent jumps in transconductance as the chemical potential of the leads aligns with the energy levels in the QPC. The energy alignment of lead with respect to the QPC levels is shown in the boxes from a) to f).

4.7. QPC energy level spacing

The energy separation between discrete states of the QPC can be probed by changing the source and drain electrochemical potential difference [153].

By applying a bias voltage across the QPC one can align source and drain chemical potentials ($\mu_{S,D}$) to the transport resonances created by the confining potential as exemplified in Figure 4.8. As the chemical potential aligns to one of the energy levels the conductance increases causing a peak in transconductance, marked as the white lines. The splitgate voltage shifts the energy levels with respect to the chemical potential producing a sequence of diamonds in transconductance. The difference in energy between two energy levels can

be read out at the edges of the diamonds (point b) when $\mu_{S,D}$ aligns to consecutive energy levels.

Figure 4.9 shows the transconductance (g_{tr}) as a function of the V_{SD} and V_{SG}, plotted in a symmetrical logarithmic scale to allow negative values. For positive (negative) bias values we observe a positive (negative) transconductance, as changes in gate voltage cause an increase in current given by the bias direction. An exception happens at the nodes around $V_{SG} =$ 6.75 V, which has a flipped transconductance. At these nodes the feature previously identified as 0.7 anomaly develops into a resonance.

To find the actual voltage drop across the QPC, V_{SD}^*, one has to consider the series resistance, such that $V_{SD}^* = V_{SD} - R_S I$. This transformation of the voltages axis results in the replotted data in Figure 4.9 b), showing the absolute value of the transconductance as a function of V_{SD}^* and V_{SG}. The plot has been normalized by the absolute values of each V_{SG} for better visualization of the diamonds. The tapered shape comes from the V_{SD}^* axis correction as described above.
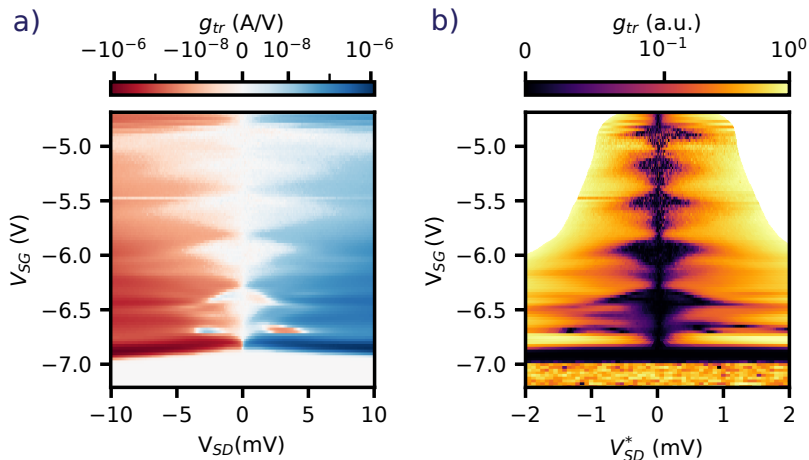
Figure 4.9. a) Transconductance g_{tr} as a function of V_{SD} and V_{SG} at $V_{BG} = -3.4$ V. b) Transconductance as a function of corrected QPC bias V_{SD}^* with normalized values for each V_{SG}. The tapered shape comes from the correction of the voltage bias for a series resistance R_S.

The limit of a diamond is extracted at 10% of the normalized scale. The extracted energy separation $\Delta\varepsilon = \varepsilon_{N+1} - \varepsilon_N$ are shown in Figure 4.10. A decrease in the energy separation is observed for increasing N, which suggests a potential shape that is flatter than a parabola. The error bars are given by the

asymmetry of the diamonds in V_{SD}^* axis. Varying the threshold for estimating the width of the diamonds changes the absolute values of the spacing but not the general decreasing trend.
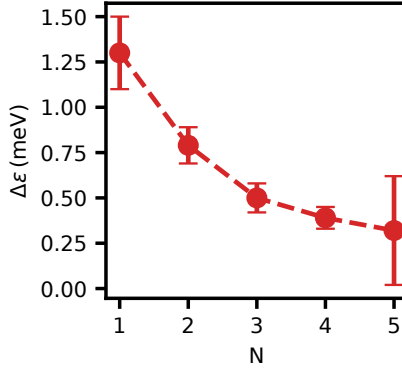

Figure 4.10. Energy separation between QPC energy level $\Delta\varepsilon_N$ extracted from bias dependence.

Although this simple analysis provides insight into the QPC potential, there are features that are not well understood. The diamonds have slight asymmetry for the different bias sides, which gives some uncertainty to the spacing extraction. The upper and lower boundaries of the diamonds seem to have different slopes, which could be attributed to changes in the capacitance by electrostatic screening after each mode is occupied. Between the diamonds, there seems to be a subset of smaller diamonds, e.g. at $V_{BG} = -6.25$ V and -5.75 V. We speculate that these features arise from the small fluctuations in the conductance plateaus as seen in Figure 4.6 b) and Figure 4.7 b). The origin is related to the resonances nearby or the mixing modes of the QPC.

4.8. Magnetic field subband splitting

We now investigate the effect of a magnetic field applied perpendicular to the sample plane. Figure 4.11 a) shows the conductance of the QPC from zero magnetic field to 500 mT in steps of 25 mT. A line resistance was subtracted as described above. The lines are displaced in the V_{SG} axis for clarity. At zero magnetic field, the plateaus occur at multiples of $2 \times e^2/h$. As the magnetic field increases the fluctuations on the conductance plateaus continuously change. From $4 \times e^2/h$ we notice a branching of another conductance plateau which ends at $3 \times e^2/h$. Similar branching happens from the shoulder at $1.4 \times e^2/h$

evolving to e^2/h value at 500mT [154]. This picture corresponds to Zeeman splitting of the degenerate spin subbands.

The evolution of the plateaus is best traced by considering the transconductance as a function of magnetic field B and splitgate voltage V_{SG}, shown in Figure 4.11 b). The white dashes follow the limits of the quantized conductance plateaus from zero magnetic field to finite field values as the plateaus at odd multiples of e^2/h evolve in splitgate axis. The map is filled with other features which we attribute to the fluctuations in the conductance plateau.
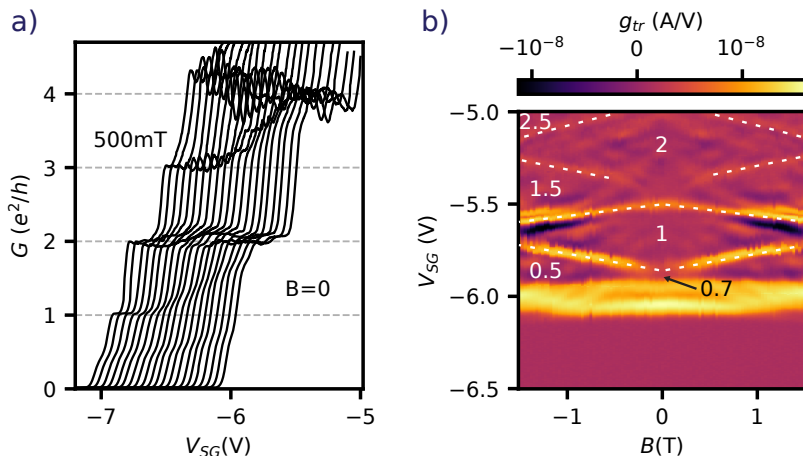

Figure 4.11. a) Evolution of the conductance plateaus from zero to 500mT in steps of 25mT. Curves are shifted in V_{SG} axis for clarity. b) Transconductance as a function of V_{SG} and B. White lines are guides to the eye. The numbers indicate the conductance values in terms of $2 \times e^2/h$.

Figure 4.12 a) shows the continuation of the magnetic field plot up to 9T and b) and schematic of the features. The QPC formation takes place at about $V_{SG} = -3.5\,\text{V}$ and total depletion at $V_{SG} = -5.5\,\text{V}$. The black dotted line below $V_{SG} = -3.5\,\text{V}$ indicate the evolution of the plateaus multiple of $2 \times e^2/h$, shrink down in magnetic field until the lines of consecutive odd multiples of e^2/h cross, indicated by the black dotted lines [93]. After this crossing the lines are discontinuous, indicated by the yellow dotted lines. Similar characteristics have been observed for GaAs [154, 155] and bilayer graphene [156]. The process that creates these discontinuities is not well understood but is thought to have a similar origin as the 0.7 anomaly [157]. At even larger magnetic fields, flat horizontal lines take place, shown as the dotted light grey lines. We attribute those to the interaction of the Landau levels with puddles of charge carrier

fluctuations within the QPC channel [158].

Additionally, for splitgate voltages above the QPC formation, there are diagonal lines which we interpret as a Landau fan diagram of Landau levels tuned in carrier density by the splitgate voltage.
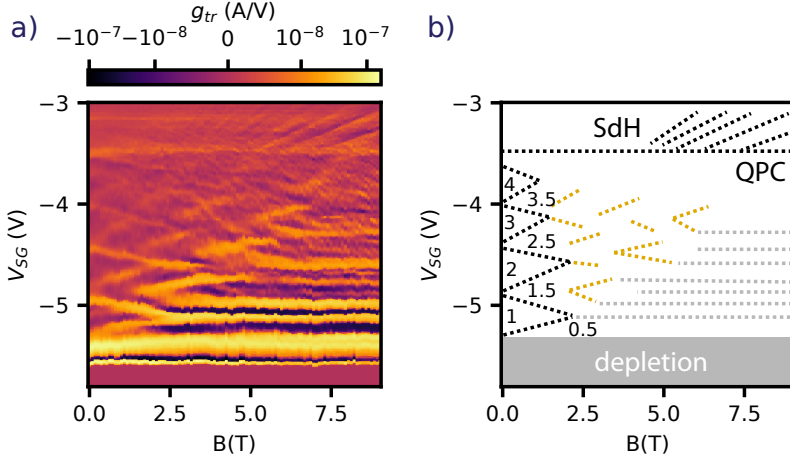

Figure 4.12. Evolution of the conductance plateaus at high magnetic field. a) Transconductance as a function of B and V_{SG}. b) Schematic outlining features in a). Numbers indicate conductance plateau values in terms of $2e^2/h$.

4.9. Outlook

We fabricated a 2DEG by encapsulating a monolayer MoS$_2$ in hBN showing high electron mobility $\mu_{FE} \sim 1155 \, \text{cm}^2/\text{Vs}$. By applying a voltage to the local splitgates, we were able to control the transport properties in a narrow constriction. We discuss how the depletion of the 2DEG underneath the splitgates can influence the sample conductance in the vicinity of the QPC. After subtraction of the correct series resistance that includes both, the 2DEG resistance and the lines resistances, a conductance quantization in steps of $2 \times e^2/h$ demonstrates a ballistic channel with discrete transverse states. The magnetic field dependence suggests that the degeneracy is rather from the spin than the valley degree of freedom. With simple electrostatic capacitances given by plate capacitor model, we were able to reproduce the backgate dependence of the transport. By probing the QPC energy channels using the chemical potential of the leads, we extract the energy separation between these channels, which points to a smooth potential shape with curvature flatter than the

ideal parabolic potential. The higher subband was not necessary to explain the QPC features. Perhaps the occupation of this upper subband is too high in energy and the QPC is already open at this energies.

These experiments demonstrate a reliable one-dimensional channel with well-understood electrostatic and quantum mechanical features given by simple models, which enable the use of QPC in MoS$_2$ semiconductors for future experiments, such as in probing superconducting proximitized regions and as a building block for QDs for spin-valley qubits.

4

5 Superconducting gap spectroscopy and quantum interference effects on S-MoS$_2$-S devices[1]
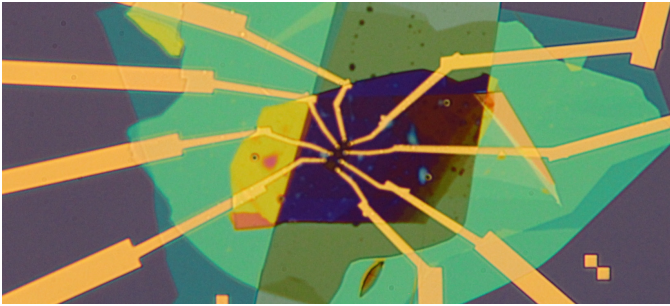
In this chapter, we demonstrate vertical interconnect access (VIA) contacts as a platform for superconductor-semiconductor hybrid devices. We build junctions using molybdenum rhenium, a type II superconductor with high critical field as contacts to a monolayer MoS$_2$. In the first device, we demonstrate the contacting of MoS$_2$ using the MoRe. Distinct contact resistance makes the electron transport mostly dominated by a single N-S junction. A clear superconductor gap is observed. In a second sample, we demonstrate the tunneling of quasi-particles through two N-S junctions. Quantum interference suggests coherent transport. A transition in the periodicity of the resonances below the superconductor energy gap indicates electron-hole transport. Sub-gap peaks in conductance close to zero bias voltage is evidence of Andreev Bound States in the system.

---

[1]Parts of this chapter were published in a similar form in Ref.[149]

5.1. Device I: Superconducting gap spectroscopy at N-S interface

In this section, we report fabrication and measurements of a superconductor-semiconductor hybrid device applying VIA contact technique. The material of choice for the contacts is molybdenum rhenium (MoRe), a type II superconductor. A monolayer MoS$_2$ is taken as the semiconductor. The transport characteristics are dominated by a single N-S interface. To avoid confusion with devices in the next sections, we name this device I. This section was published in a similar form in Ref. [149].

5.1.1. Fabrication

The sample consists of an encapsulated monolayer MoS$_2$ contacted by MoRe VIAs. Figure 5.1 a) shows an optical image of the device's surface and a schematic of the heterostructure cross-section. The VIAs were fabricated using by etching 200 nm radius holes into a 40 nm thick hBN flake with SF$_6$ reactive ion plasma. Detailed parameters are given in appendix E. In a second EBL step, a larger areas, $\sim$300 nm, are defined, where 60 nm of MoRe (50:50) are deposited by sputtering. MoRe is a type II superconductor with bulk critical temperature $T_C \approx$ 6-10 K and critical field $B_{C_2} \approx$ 8-9 T.

The chip containing the MoRe VIA contacts is transferred to the glovebox, where the heterostructure is assembled. It consists of a monolayer MoS$_2$ encapsulated by hBN flakes and contacted by the MoRe VIAs. A graphite flake serves as backgate. The heterostructure is released onto a SiO$_2$ chip. A final EBL step defines the leads and bondpads by evaporating Ti/Au electrodes by standard electron beam evaporation.

Most of the experiments were performed in a dilution refrigerator at 60 mK, with the exception of the higher temperatures, which were performed in a variable temperature insert (VTI) with base temperature of 1.7 K.

5.1.2. Single N-S interface transport

The fabrication process yields about 60% of working contacts. The minimal resistance area product is about 200 kΩ μm. The four contacts are labeled from C$_1$ to C$_4$ in Figure 5.1 a). From simple estimations of the magnetic field characteristics, we obtain electron mobilities $\mu \sim$ 2500 cm^2/Vs (data shown in appendix B).

We use contacts C2 and C4 for the main analysis, with a channel distance of about 4 μm. We use the standard lock-in technique to probe the conductance through the device by applying a sinusoidal signal of $f =$ 77 Hz of amplitude $V_{AC} =$ 5 μV. A DC voltage bias is added to this through a transformer.
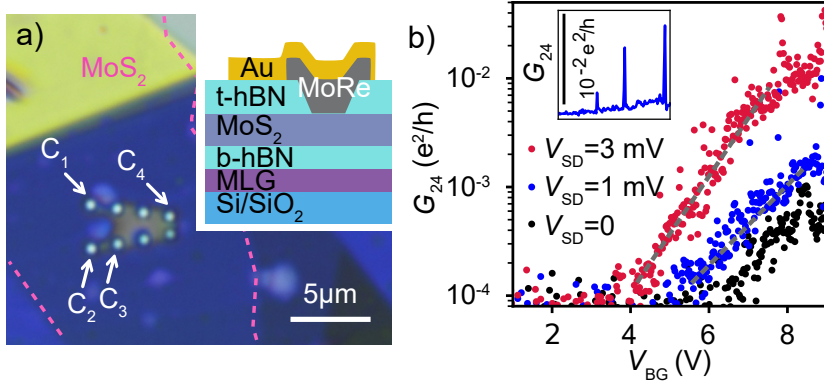
Figure 5.1. a) Optical image of the device I surface, indicating the contact labels. Inset: cross-section of the heterostructure. b) Conductance through C2-C4 as function of V_{BG} at the bias voltages indicated. Inset: same as blue dots on a linear scale, illustrating Coulomb resonances.

Figure 5.1 b) shows the conductance $G_{24} = dI/dV_{SD}$ as a function of the backgate voltage V_{BG} for three values of bias voltages V_{SD}, zero, 1 mV and 3 mV. Starting with the red dots for $V_{SD} = 3$ mV, we observe an exponential increase in conductance from the depletion at $V_{BG} \sim 4$ V. Decreasing the bias voltage to $V_{SD} = 1$ mV, shifts the depletion to a higher value, $V_{BG} \sim 5$ V. The extreme case happens at $V_{SD} = 0$, where the depletion happens at $V_{BG} \sim 6$ V. This shift in the depletion voltage indicates a bias dependence on the transport, suggesting an energy gap for low biases. Additionally, we observe sharp resonances in conductance, which are consistent with Coulomb blockade effects, shown in the inset of Figure 5.1 b). We note that the backgate should affect the charge carrier density in the semiconductor, the Schottky barrier at the metal-semiconductor interface and disorders induced by charge islands.

To further investigate the energy gap, we plot the conductance as a function of voltage bias V_{SD} and backgate voltage V_{BG} in Figure 5.2 a). A suppression in conductance of a factor of ~ 8 takes place at roughly $|V_{SD}| = 1.2$ mV throughout the whole range of V_{BG}. We attribute this value to the energy gap of bulk MoRe, which is consistent with literature values [159]. For $|V_{SD}| > 1.2$ mV, we observe a modulation in the conductance, correspondent to the aforementioned Coulomb blockade resonances. These resonances result from strong confinement near the contact region. Given that such a sharp gap is only observable if a tunnel barrier is present between N and S parts, we understand the device as a MoS$_2$ channel, incoherently coupled to the MoRe contacts with one of the
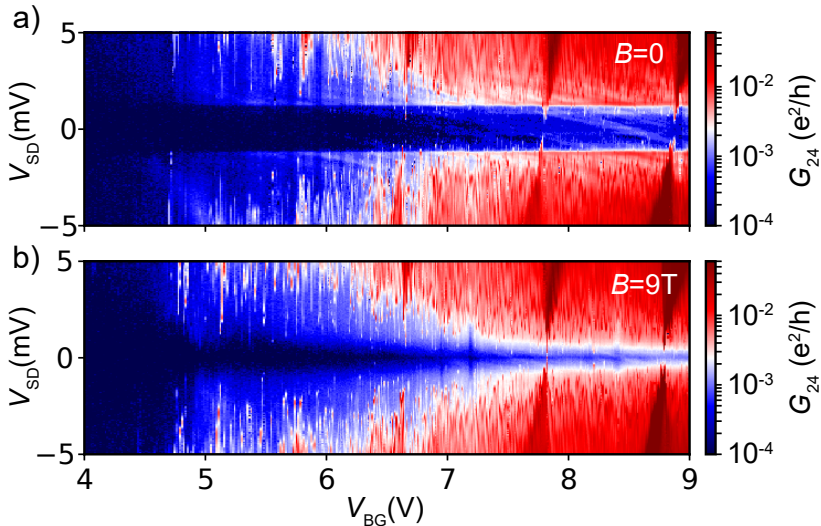
Figure 5.2. a) Conductance as a function of V_{SD} and V_{BG} at $B = 0$ and b) at $B =$9 T.

interfaces dominating the transport, namely the one with larger voltage drop.

Figure 5.2 b) shows the conductance as function of the backgate voltage V_{BG} and voltage bias V_{SD}, now at $B =$9 T magnetic field applied in out of plane direction. As expected, the bulk MoRe superconducting gap diminishes, represented by the reduction in the suppression width in bias. Moreover, a backgate voltage dependence is observed, giving a tapered shape to the suppression. This is tentatively attributed to a gate independent superconducting energy gap convoluted with a gate tunable MoS$_2$ conductance.

We further investigate the gap dependence in magnetic field by repeating the measurements shown in Figure 5.2 for more field values (See appendix B). We averaged these plots over a gate voltage interval of 0.5 V for each V$_{SD}$ value. Figure 5.3 d) shows a consistent decrease of the energy gap for increasing magnetic field. For $B = 0$ we fit the BTK model, using equation 2.36 modified to include a broadening parameter [160]. The resulting fit parameters are consistent with a single N-S junction with low transmission at the interface.

Figure 5.3 e) shows the trend of the energy gap Δ^* as a function of magnetic field for three contact configurations. The inflection point of the curves are taken as the energy gap. To fit the field dependence of the superconducting energy gap Δ^* we use the standard theory of superconductivity for pair-breaking in the dirty limit, where $l_{\mathrm{mfp}} \ll \xi$ [161]. The energy gap Δ^* is given by the
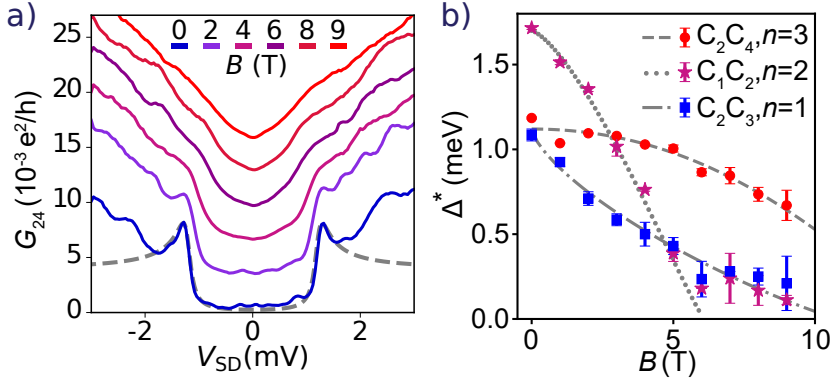
Figure 5.3. a) Average conductance as a function of V_{SD} at the indicated magnetic fields. Curves displaced in y-axis. b) Superconducting energy gap Δ^* as a function of B for different contact pairs. Δ^* is extracted from the inflection points in the averaged curves (red disks), from the Coulomb resonances in Figure 5.4 (purple stars), and from the data set shown in appendix B (blue rectangles).

pair braking parameter α by [162]

$$\Delta^*(\alpha) = \tilde{\Delta}(\alpha)[1 - (\alpha/\tilde{\Delta}(\alpha))^{2/3}]^{3/2}, \tag{5.1}$$

where the order parameter $\tilde{\Delta}(\alpha)$ is obtained from the self consistent equation $ln(\tilde{\Delta}(\alpha)/\Delta_0) = -\pi\alpha/4\tilde{\Delta}(\alpha)$, with Δ_0 being the energy gap in absence of magnetic field. The field dependence of the pair braking parameter α is given by

$$\alpha = 0.5\Delta_0(B/B_c)^n, \tag{5.2}$$

with n as characteristic exponent. The best fit we obtain for $n = 3$, $\Delta_0 = 1.12\,\text{meV}$ and the (upper) critical field $B_C = 14.5\,\text{T}$. The latter value is clearly larger than reported for bulk MoRe.

If a quantum dot is in close proximity to a proximitized S region, the tips of the Coulomb diamonds are displaced in bias voltage by the superconducting energy gap [163]. In Figure 5.4, we follow the evolution of Coulomb resonances in magnetic field. The low-bias ends of the Coulomb resonances are shifted in energy and in gate voltage, as indicated by the gray dashed lines, consistent with a MoS$_2$ quantum dot directly coupled to one superconducting contact, forming an S-QD-N junction. We read out Δ^* from the bias values at which 50% of the large bias conductance is reached at the tip of the Coulomb blockade

resonances. With this analysis, contacts C1-C2 (purple star) yields a significantly larger zero field gap, $\Delta_0 \sim 1.7$ meV, and a rather different functional dependence on B. The latter is demonstrated by the dotted line obtained for the exponent n = 2, and $B_C =6.4$ T. Furthermore, these resonances are connected across the gap by a single faint resonance, pointed out by yellow arrows, best seen at B = 2 T. We attribute these lines to resonant Andreev tunneling, in which the electrons of a Cooper pair pass through the QD in a higher order tunneling process [163]. This process is suppressed much stronger by a tunnel barrier than single particle tunneling, which suggests that the quantum dot is strongly coupled to the superconductor [164]. The proportions of the quantum dot are estimated using a circular disk geometry yielding $r \sim 300$ nm.
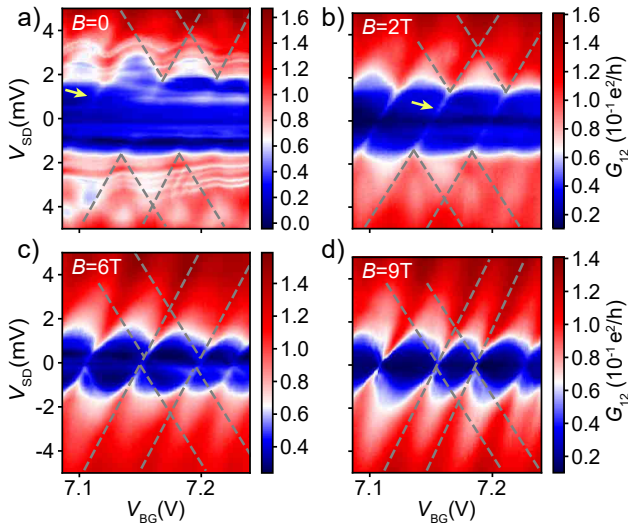
Figure 5.4. Extraction of Δ^* from Coulomb resonances displacement in V_{SD} for contacts C1-C2. a) to d) show the conductance through contacts C1-C2 as function of V_{BG} and V_{SD} at the indicated magnetic fields. The Coulomb resonances tips are indicated by the dashed grey lines.

The same analysis is made for contacts C2-C3 (blue rectangles), with data available in appendix B. For this curve, we obtain n = 1, while $\Delta^* \sim 1.12$ meV and $B_C \sim 12$ T correspond well to the previously obtained values. While a larger gap in the transport experiments can be simply attributed to a significant fraction of the bias developing across another part of the device, for example, across the second N-S junction, the different functional dependence is not well understood.

We now analyze the temperature dependence of the energy gap. Figure 5.5 a) shows the conductance of the device for temperatures ranging from 1.7 K to 7.8 K. The curve at 1.7 K is fitted (dashed line) using the BTK model, adjusting the normal state resistance and the temperature. We use the inflection points to estimate the energy gap size and plot it as function of temperature in Figure 5.5 b). These points are fitted to $\Delta^* = \Delta_0\sqrt{1 - T/T_C}$, yielding a critical temperature $T_C =$7.7 K in good agreement with literature values for bulk MoRe [159, 165].
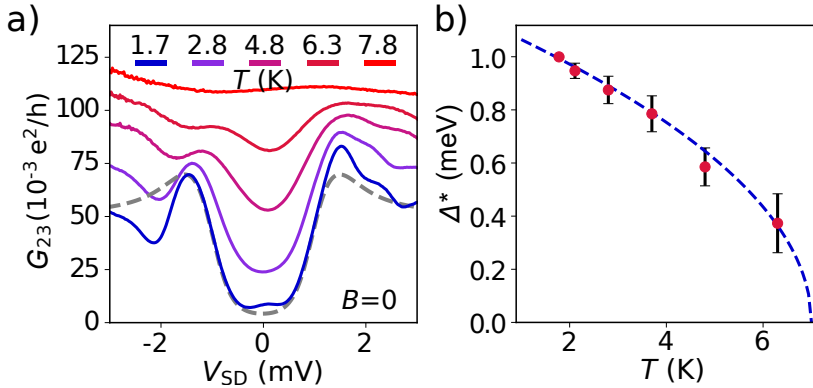
Figure 5.5. a) Conductance as function of V_{SD} at the indicated temperatures for contacts C2-C3. Curves displaced in y-axis. b) Extraction of Δ^* as a function of temperature from the inflection points of the curves in a).

5.1.3. Conclusion for device I

In conclusion, we established superconducting contacts to a monolayer of the TMDC semiconductor MoS$_2$ using MoRe VIA contacts. The transport corresponds to a MoS$_2$ incoherently coupled to MoRe reservoirs. The superconducting energy gap is in good agreement with a single N-S interface with low transmission coefficient. The magnetic field- and temperature dependence of the energy gap ensure conformity to bulk MoRe superconductivity. An asymmetry in the contact transparency leads to a higher voltage drop at one of the N-S interfaces, which dominates the transport.

5.2. Device II: Quantum interference effects on S-MoS$_2$-S devices

The data in device I exhibited an asymmetry between contacts which led to single N-S interface physics, i.e., one NS interface was more conducting for sub-gap voltages, so that the measured voltage drop mainly occurs across the other, less ideal junction. In this section we introduce a device with more uniform contacts, demonstrating the two N-S interfaces. The previously observed Coulomb resonances resulting from strong confinement are now replaced by quantum interference effects. Sub-gap features evidence the formation of bound states between the Andreev reflections at the N-S interfaces and defects in the semiconductor.

5.2.1. Fabrication
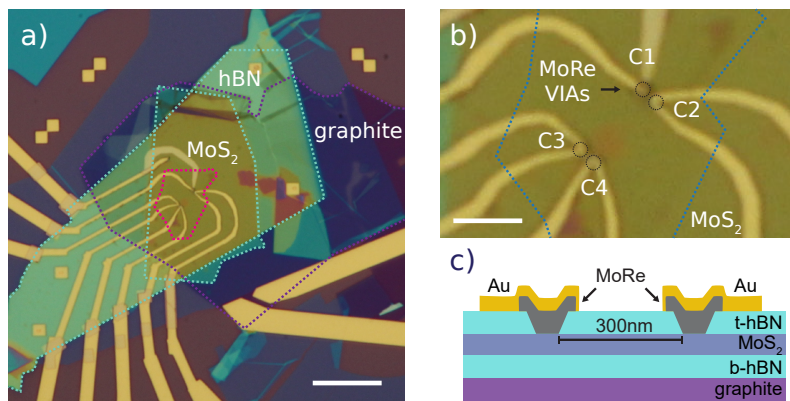
Figure 5.6. a) Optical image of the device II surface with flakes indicated. Scale bar is $10\,\mu$m. b) MoRe VIAs contacts and their labels. Scale bar is $3\,\mu$m. c) Schematic cross-section of the heterostructure.

Device II[2] is fabricated in a similar manner as device I, with improvements in the VIA contact fabrication. We decrease the channel length to $300\,$nm and increase the yield and reproducibility of the contacts. The acceleration voltage used in the EBL was reduced for a larger undercut in the PMMA mask, which decreases the side deposition caused by MoRe sputtering. The reactive ion etching with SF_6 was better timed to avoid excessive etching of the substrate where the VIAs are deposited. An AFM cleaning step was introduced before

---

[2]Two samples were produced, showing compatible characteristics.

stacking the hBN flake to clean residual side deposition and polymer at the surface of the device. With a yield of 100% the contacts in device II have normal state resistance in the range of 150 - 200 kΩ which corresponds to a resistance-area product of 20 - 30 kΩ μm^2, a factor of ten lower than device I. Figure 5.6 shows an optical image of the sample surface with contact labels indicated. We focus our discussion on contacts C1-C2, with a separation of about 300 nm.

5.2.2. Two N-S interfaces transport

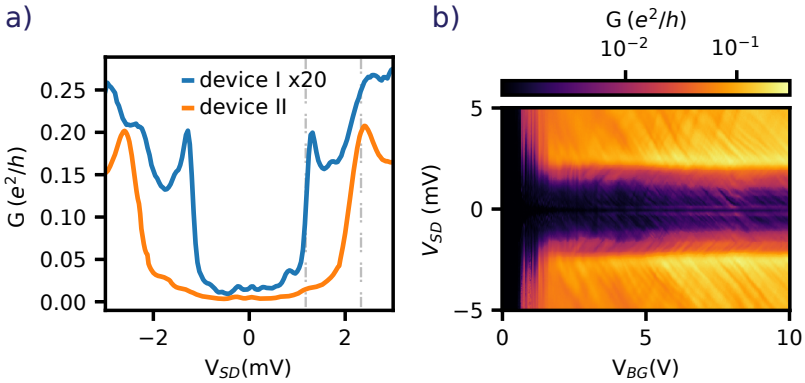This improved fabrication allows us to investigate new effects, onto which we put now our focus.

Figure 5.7. a) Conductance as a function of V_{SD} comparing devices I and II at similar charge carrier density n. b) Conductance of device II as function of V_{BG} and V_{SD}.

In Figure 5.7 a) we compare the conductance of devices I and II as a function of V_{SD} for at similar charge carrier density $n \sim 6 \times 10^{12} \text{cm}^{-2}$. The curve for device I was rescaled for clarity. We observe a doubling in the width of the suppression in conductance for device II, consistent with a low junction transparency, but very similar for both contacts. This contrasts with the single N-S interface transport exhibited by device I. We interpret this structure as a more even voltage drop between the two interfaces. The quantities Δ/e and $2\Delta/e$ are marked in the bias voltage axis.

The conductance as a function of V_{SD} and V_{BG} for device II is plotted in Figure 5.7 b). The suppression in conductance at $|V_{SD}| = 2.4$ mV extends throughout the whole V_{BG} range. For $V_{BG} < 1.8$ V, we find Coulomb block-

ade resonances, most likely due to disorder near the contacts, that become less screened near the conduction band minimum. Here, we focus on larger backgate voltages.

In this regime (V_{BG} >1.8 V), we find a continuous, essentially sinusoidal modulation of the conductance as a function of both, V_{BG} and V_{SD}, without a discernible Coulomb gap. The visibility of these resonances is $\Delta G/\overline{G} \sim 0.2$ for $|V_{SD}|$ >2.4 mV. At around V_{BG} =5 V, an increase in the average conductance takes place. This backgate voltage corresponds to $n \sim 3 \times 10^{12}$cm^{-2}, which is obtained using a plate capacitor model with 30 nm hBN flake thickness and depletion voltage at V_{BG} =0.6 V. This charge carrier density suggests the occupation of the second subband [39]. At zero bias an even stronger suppression in conductance is observed. These features are discussed below.

5.2.3. Quantum interference effects
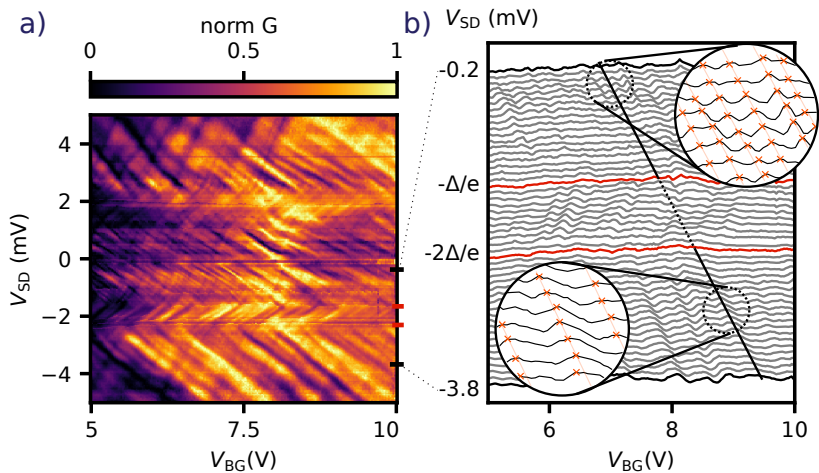
Figure 5.8. Evolution of FP resonances in gate voltage. a) Normalized conductance as function of V_{BG} and V_{SD}. Normalization is taken for every bias voltage line. b) Wireplot of the indicated bias in a). The gap edges Δ/e and $2\Delta/e$ are marked as red lines. The black diagonal line follows a resonance from high (bottom) to small (top) V_{SD}. The zoomed-in regions have the same V_{BG} range and mark the resonance peaks with orange X.

In this section, we discuss the modulation in conductance often called electronic Fabry-Perot (FP) resonances [166].

To make these resonances more visible, we normalized the conductance along the backgate axis of the data[3], as plotted in Figure 5.8 a). We find a regular pattern of narrow resonances with an enhanced conductance.

Such resonances in the normal state originate from constructive interference of the partial electron waves formed between two scatterers, or in a confined region, as in a cavity. The backgate tunability indicates that this interference happens in the semiconductor material and that each resonance marks a specific Fermi wavelength λ_F, multiples of $\lambda_F/2$ should match the cavity length L. Thus, a constructive interface takes place when

$$2Lk_F \overset{!}{=} 2\pi N, \qquad (5.3)$$

where $N \in \mathbb{Z}$.

We note that there is a change in the slope around $|V_{SD}| = 1.2\,\mathrm{mV}$ and $2.4\,\mathrm{mV}$, switching from positive to negative slope and then back to positive at small bias. These values of voltage bias correspond to Δ/e and $2\Delta/e$ respectively. We understand these changes in the slopes as a mere change in the visibility of resonances with asymmetric barriers modulated by the DoS in the superconductor, which results in a bias dependent electrochemical average potential on the MoS$_2$ channel. The concrete discussion is given in appendix C, but for the main text it is important to note that the spacing between the resonances in gate voltage does not depend on the bias.

For hard-wall confinement, the spacing in k-space between two of the resonances matches the cavity length as $\Delta k = \pi/L$. Relating this spacing to the spacing of the resonances when plotted as a function of the electron density, one finds

$$L = \frac{\sqrt{2\pi/p}}{\sqrt{n_{N+1}} - \sqrt{n_N}}. \qquad (5.4)$$

where p is the band degeneracy[4] and n_N is the charge carrier density related to the N-th resonance, which can be translated by equation 2.6 to a backgate voltage.

From the data in Figure 5.7 b) we extract backgate voltages for consecutive peaks and estimate L using equation 5.4. The results are plotted in Figure 5.9 b). For high negative, $|V_{SD}| > 2\Delta/e$ we obtain similar values of $\sim220\,\mathrm{nm}$. For a low bias of $|V_{SD}| < 2\Delta/e$ the apparent length of the cavity seems to double i.e. $L \sim500\,\mathrm{nm}$.

---

[3]For every bias value we calculate the normalized conductance as $G(V_{BG}) = \dfrac{G(V_{BG}) - G_{min}}{G_{max} - G_{min}}$.

[4]Considering the two-fold spin degeneracy in monolayer MoS$_2$, $p = 2$ for the lower subband occupation and $p = 4$ if upper and lower subbands are occupied.
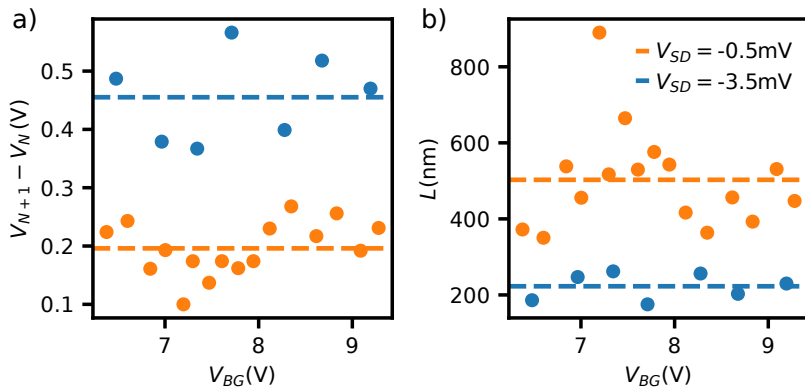
Figure 5.9. a) Difference in V_{BG} for two consecutive resonances at $V_{SD} = -0.5\,$V (orange dots) and $V_{SD} = -3.5\,$V (blue dots). b) Calculated cavity length using equation 5.4 for two consecutive resonances at $V_{SD} = -0.5\,$V (orange dots) and $V_{SD} = -3.5\,$V (blue dots). The dashed lines in both figures represent the mean value of the respective points.

Since this effect seems not to originate from electrostatic effects (see appendix C), we attribute this apparent doubling of the cavity length to Andreev reflection (AR) occurring at *one* of the superconducting reservoirs, which results in a hole being retro-reflected and retracing the same trajectory as the original electron, thereby acquiring the same phase one more time. Only after another AR process, the hole is again converted into an electron partial wave that can interfere constructively with the original electron wave, as shown in Figure 5.10 for a) above the superconducting gap and b) sub-gap AR.

Such a discrete quantum state with an AR process at one or more boundaries is usually called "Andreev bound state" (ABS), and were observed in MBE grown 2D systems [167] and in several 1D systems, like carbon nanotubes [168–170] or semiconducting nanowires [17], and now in a 2D monolayer semiconductor. We note that in contrast to previous examples based on quantum dot physics, in the presented case, electron-electron interactions seem to be negligible and the ABSs are dominated by the quantized kinetic energy.

5.2.4. Two dimensional Andreev Bound states near a superconductor in a disorder system

Now we focus on conductance resonances at very low bias, $|V| \ll \Delta/e$. Figure 5.11 shows data sets for a series of magnetic fields and a smaller backgate voltage range. In Figure 5.11 a) at zero magnetic field, the conductance shows
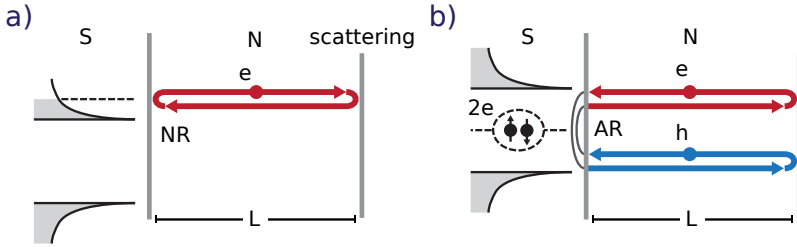
Figure 5.10. 1D schematic of the process resulting in the cavity length doubling. a) In the quasiparticle regime of the superconductor an electron reaches the N-S interface and is retro-reflected by a NR, traveling the length $2L$ before being backscattered and interfering with itself. b) At the superconducting gap, the electron is retro-reflected as a hole, which travels the length L, then is backscattered back to the N-S interface. Another Andreev reflection generates an electron which then interferes with the initial wavefunction. The total length traveled is $4L$.

sharp resonances that can be traced back to the FP resonances discussed above. These resonances end at a maximum conductance at $|V_{SD}| \approx 170 \, \mu V$. Below this voltage, the conductance is suppressed by a factor of ~ 3 at zero bias voltage. For the sake of discussion, we call this feature "minigap" [171, 172], to distinguish it from the superconducting energy gap of bulk MoRe. We find such a minigap for all gate voltages, and similar characteristics in experiments with other contact pairs. For larger magnetic fields, for example in Figure 5.11 b), the peaks of the minigap split in energy, which results in a slightly larger minigap and two "sub-minigap" resonances, all essentially independent of the gate voltage, in contrast to the sloped resonances discussed in the previous section. At a certain magnetic field of $B \sim 2 \, T$, the two sub-minigap peaks merge at zero bias to form a single maximum that sticks to $V_{SD} = 0$ as a function of V_{BG}. This zero bias peak (ZBP) persists for an extended magnetic field range of $\sim 1.2 \, T$. An example is shown in Figure 5.11 c) at $B = 2.8 \, T$.

At even larger magnetic fields, the amplitude of the ZBP decreases below the resolution of our experiments without a discernible splitting and with the ordinary FP resonances becoming visible also in the minigap region, as shown in Figure 5.11 d) for $B = 4 \, T$. The resonance spacing is essentially still the same as at zero field, consistent with the fact that the bulk MoRe gap is still significantly larger at these fields.

The magnetic field dependence of the minigap and the emerging zero-bias conductance peak can be best seen in Figure 5.12 a), where we plot the bias traces averaged over the backgate voltage range of Figure 5.11, for a series of magnetic fields. In addition, in Figure 5.12 b) we plot a single trace of the raw
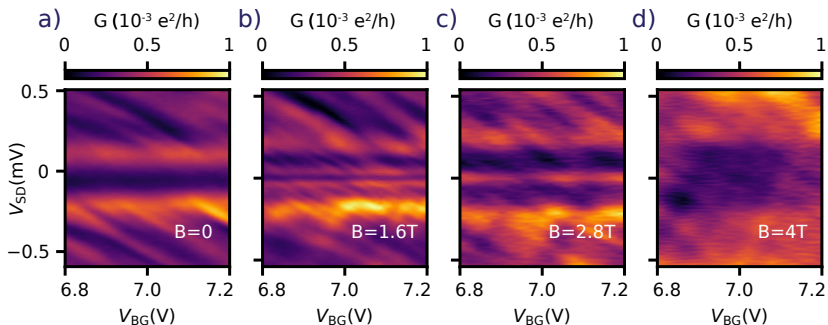
Figure 5.11. Sub-gap peaks evolution in magnetic field. a) to d) Conductance as function of V_{BG} and V_{SD} at the indicated magnetic fields.

data ($V_{BG} = 8$ V) as a function of B, with an individual constant background conductance subtracted for each V_{BG} , to remove random conductance fluctuations possibly due to flux vortices in the superconductor [163]. While the former plot shows the zero-bias peak especially clearly, the latter shows the splitting off of the sub-minigap resonances, a linear dependence of the position with the magnetic field, and that they merge into a zero-bias peak that then "sticks" to zero over a prolonged magnetic field. We have observed similar characteristics, including ZBP at a finite magnetic field in the measurements of all other contact pairs, and in other devices.

ZBP have gained a large interest in the search for topologically non-trivial, Majorana-like subgap states, but have also been found in topologically trivial phases [173, 174], for example, due to quantum interference in nanowires with intrinsic spin-orbit interaction [175]. Since the resonances in our case are essentially independent of the gate voltage, and the magnetic field is applied perpendicular to the electron motion, we propose a different mechanism, namely ABSs forming in a slightly disordered 2D material near a superconducting contact.

Our semi-classical view is sketched in Figure 5.13. In the normal state of a superconducting reservoir and at zero magnetic field, a single electron wave forms a loop enclosing a finite area due to a series of scattering events near the contact and normal reflections (NR) at the contact, as in Figure 5.13 a). On these loops, the partial electron waves can interfere constructively or destructively, depending on the path length L and the Fermi wavelengths of the electrons. The distribution of path lengths L_j and the corresponding areas A_j are determined by the disorder characteristics, like the mean free path l_{mfp}, and vary from contact to contact. If the reservoir is superconducting, the reflection at the contact is replaced by AR for low energies, which results
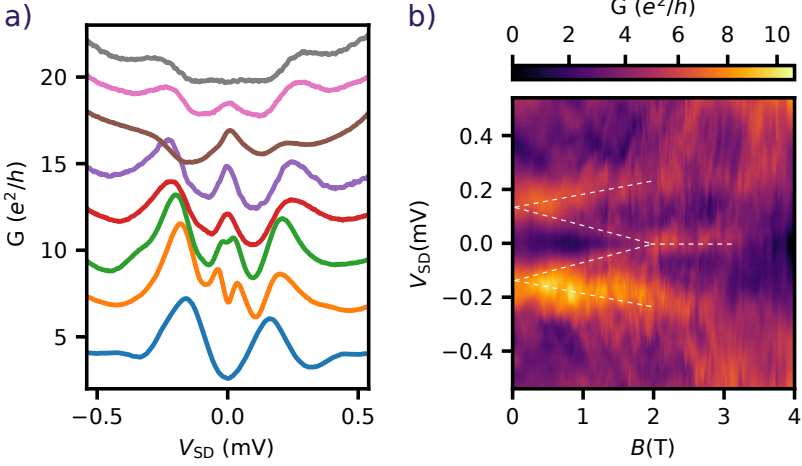
Figure 5.12. Evolution of the sub-gap peaks in magnetic field. a) Average conductance over V_{BG} =6.8-7.2 V as function of V_{SD} at the indicated magnetic fields. b) Conductance as function of B and V_{SD} at V_{BG} =8 V. White dashed lines are a guide to the eye.

in a retro-reflected hole tracing back the original electron path [176]. For low enough magnetic fields the semi-classical trajectories can be considered as straight before a scattering occurs, which suggests that the cyclotron radius $r_c = \frac{m^* v_F}{eB}$ is smaller than the mean free path l_{mfp}, or $B < \frac{m^* v_F}{el_{mfp}} \sim 2$T, for $\mu \sim 5000\,\text{cm}^2/\text{Vs}$ [149]. Over this range, we expect the trajectories to be only weakly affected by the magnetic field, except for a phase gain due to the enclosed area A. Similar as discussed in section 2.5.2, near a superconducting contact [112], we obtain the condition for constructive interference on a given path j as

$$2L_j \frac{E_N^j}{\hbar v_F} - 2\arccos\frac{E_N^j}{\Delta} \pm 4\pi\frac{\phi_j}{\phi_0} = N \cdot 2\pi, \qquad (5.5)$$

where $N \in \mathbb{Z}$, E_N^j is the resonance energy, Δ the superconductor energy gap, $\phi_j = A_j \cdot B$ is the magnetic flux through the area of the loop, and $\phi_0 = h/e$ the single electron flux quantum.

The first term describes a phase gain due to the evolution along the trajectory, the second term is the phase due to the two ARs, and the third term accounts for the phase due to the vector potential of the magnetic field. This
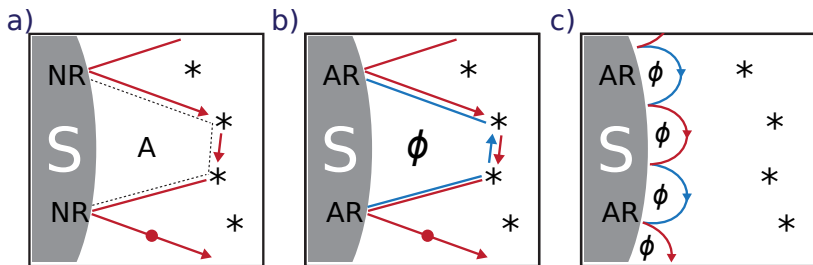
Figure 5.13. Semi-classical model of the quasiparticle trajectories. The shaded area on the side represents the superconductor interface, the white the semiconductor and the start scatterers randomly distributed around ℓ_{mfp}. a) In the normal state of the superconductor and at $B = 0$, electrons are scattered around the interface forming a loop of area A. b) In the superconductor limit a AR hole traces back the original electron path. At small fields, the trajectories are almost straight. The area A picks a flux ϕ. c) In the superconductor limit with quasiparticles in skipping orbits due to strong magnetic fields.

last term can have either sign because the electron can traverse the loop in either direction. A more precise description would take into account the average over an ensemble of possible loop trajectories, for which we expect a distribution with the most probable loop length on the order of a few mean free paths. However, we stress that our picture is that there is a distribution of such trajectories with a maximum number for a given average area and path length, which results in a conductance maximum at the bias and magnetic field that corresponds to the most probable trajectory properties. In addition, we only consider small energies $E_N << \Delta$, so that the second term can be approximated as $2 \arccos E_N/\Delta \approx \pi - 2E_N/\Delta$, which results in

$$E_N = \frac{2\pi}{F}(N + \frac{1}{2}) \pm \frac{4\pi e A}{hF}B, \tag{5.6}$$

with the constant $F := \frac{2L}{\hbar v_F} + \frac{2}{\Delta}$.

This equation explains several of our observations:

1) for $B = 0$, there are no resonances allowed, and the first ABSs occur for $N = -1$ and $N = 1$, symmetrically around $V_{SD} = 0$, which one might interpret as a "minigap" at the characteristic energy $\Delta^* = \pi/F$.

2) we expect the resonance energy to change linearly with B, as found in the experiments, with a slope given by the prefactor in equation 5.6. We can extrapolate these resonances to obtain the characteristic field at which the resonances merge to zero bias, $B_{low} \sim \frac{h}{4eA}$. Though we at least qualitatively may understand the low field characteristics, this toy model does not account

for the "sticking" of the resonance to zero bias. Our qualitative explanation for this is that in this field, the cyclotron radius shrinks to the same order of magnitude as the mean free path, so that the trajectories become curved. Once $r_c < \ell_{mfp}$, the trajectories are not affected by disorder anymore, and we expect electron and hole skipping orbits. Since the most probable and efficient emission angle is perpendicular to the contact surface, the electron and hole areas enclose the same areas, but, while obtaining the same kinetic and AR phases, they pick up the opposite flux because of the opposite quasiparticle charge [177], so that the two fluxes cancel and resonance becomes field-independent. Similar as discussed in section 2.5.2, a finite bias then suppresses the conductance because of different paths at different energies in the bias window average out to zero conductance. We believe that this qualitative picture of skipping electron and hole orbits at a superconductor interface shows similar characteristics to more elaborate theoretical predictions of zero-bias peaks in a disk-shaped semiconducting region surrounded by a superconductor [178], which can also occur with only small spin-orbit interaction.

5.2.5. Conclusion for device II

Improving the MoRe VIA fabrication resulted in devices with a lower contact resistance and more uniform voltage drop at the leads. The latter is witnessed by the doubling of the suppression in conductance, corresponding to the quasiparticle tunneling through two consecutive N-S interfaces. In the gate dependence we observe fluctuations in the conductance arising from coherent quantum interference of the quasiparticle wavefunctions above the energy gap. A doubling of the resonance frequency within the superconductor energy gap is an indication of electron-hole transport mediated by AR at the superconducting contact. Moreover, we analyze sub-gap conductance peaks, which we attribute to ABS between S and the surrounding disorder. We qualitatively explain the behavior of these states in magnetic field by a semi-classical picture of the quasiparticle trajectories.

5

5.3. Outlook for MoRe VIAs to monolayer MoS$_2$

We demonstrate that superconducting VIA contacts offer a promising platform for implementing hybrid devices in the context of 2D semiconductors. We were able to maintain pristine crystal with high electron mobility in chemical-free interfaces to the superconductor material. The intrinsic superconductivity of the leads presented clear effects on the device transport characteristics. Strong indications of coherent transport were provided, with single particle resonances above the superconducting energy gap, and Andreev bound state resonances at energies below. Although the Josephson effect was not observed, we presume that a reduction in the channel length could show coherent effects across the entirety of the device.

5

6 Quantum interference effects on S-InSe-S devices
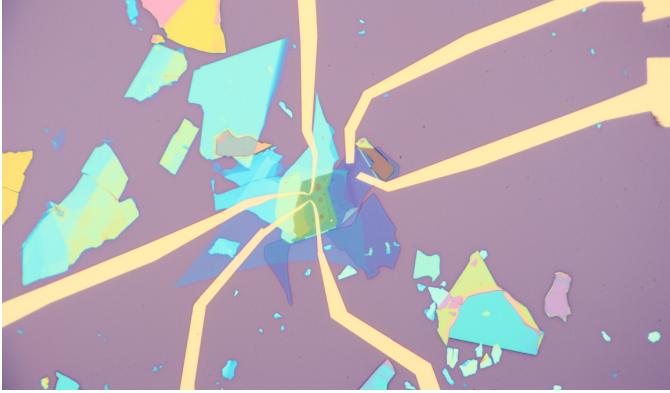
In this brief chapter, we discuss devices based in 2D InSe semiconductor. Our interest in InSe lies in reported high mobility [REF] and low electron effective mass. With CB minimum in the Γ point, no valley degree of freedom or intrinsic spin-orbit interaction InSe has a simpler band structure compared to MoS_2, which could be seen as control experiments to compare to the MoS_2 devices.

We demonstrate edge contacts as a potential architecture for contacting InSe in hybrid devices. Afterwards, we apply the VIA architecture to InSe, which yields results comparable to MoS_2. However, the sub-gap features do not match the proposed model, requiring further investigation.

6.1. MoRe edge contacts to a few layer InSe

Edge contact technique is promising to avoid extensive modifications in the band structure of 2D semiconductors caused by top contacted devices as only the sharp end of the material is in contact with the metallic lead. Here we demonstrate the fabrication of superconducting edge contacts to InSe and characterize the electrical transport.

6.1.1. Fabrication

A 5 nm thick InSe flake is encapsulated in hBN by the dry transfer method. A multilayer graphene at the bottom of the stack serves as backgate. The top hBN thickness is estimated about 40 nm by AFM scans. An EBL step defines regions in a PMMA resist which are etched using CHF_3 plasma (parameters available in appendix E). Afterwards, 60 nm MoRe are sputtered into the etched holes creating contacts to the InSe flake in a 300 nm channels. A step AFM cleaning is performed to remove excess material resulting from sputtering. Ti-Au leads are deposited connecting to the MoRe electrodes. Figure 6.1 a) shows an optical image of the device surface before the Ti-Au leads were deposited. The inset shows a schematic of the heterostructure vertical cross-section. The sample was mounted to a dilution refrigerator and cooled down to 60 mK. The measurements shown below were performed using standard lock-in technique.
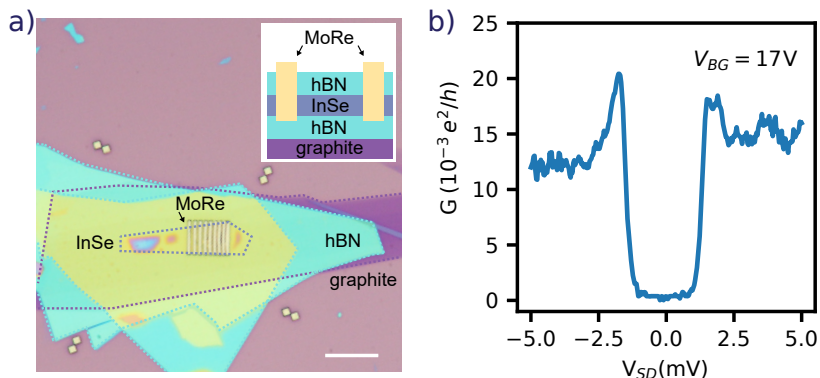

Figure 6.1. MoRe edge contacts to InSe. a) Optical image of the sample surface. Inset shows a schematic of the vertical cross-section of the heterostructure. The scale bar is $10\,\mu m$. b) Conductance as function of V_{SD} at $V_{BG} = 17\,V$.

6.1.2. Characterization

We measured the conductance as a function of the applied bias voltage V_{SD} for $V_{BG} = 17\,$V, shown in Figure 6.1 b). Similar results as discussed in chapter 5 are observed, showing transport characteristics of a quasiparticle tunneling through a single N-S interface.

The conductance as a function of V_{BG} and V_{SD}, plotted in Figure 6.2 a) shows a tapered shape of the suppression in conductance. At $V_{BG} < 13\,$V the suppression has width $V_{SD} \approx 1.5\,$mV, which decreases to $V_{SD} \approx 1.2\,$mV at maximum gate voltage. We tentatively attribute the tapered shape to a gate dependent resistance of the InSe semiconductor, which has a similar value to the resistance at the largest N-S interface below $V_{BG} = 13\,$V. Above this value, the main resistance is only the N-S interface bringing the suppression to the expected value for Δ_{MoRe}.
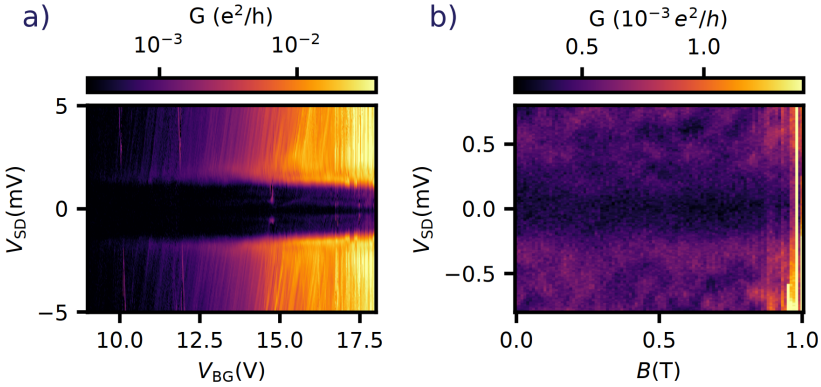

Figure 6.2. MoRe edge contacts to InSe a) Conductance as a function of V_{BG} and V_{SD}. b) Conductance as function of B and voltage bias V_{SD} at $V_{BG} = 15\,$V.

Also in Figure 6.2 a), for bias voltages above $V_{SD} = 1.2\,$mV conductance modulations are visible. Upon further inspection, we note that these modulations are also present in the sub-gap region (not shown). In this case, they form a "minigap", as discussed in chapter 5, around $V_{SD} = 250\,\mu$V. Additionally, two CB resonances are seen at 10 V and 12 V backgate. The interpretation of these modulations is similar to the discussion in chapter 5, where here the variation in the position of the "minigap" can be thought of as a variations in the path length distribution made by the charges in the semi-classical model. Unfortunately, the sub-gap limit in this sample is too noisy to make any comparison of the apparent cavity length. Figure 6.2 b) shows the conductance at a small

V_{SD} range as a function of magnetic field for V_{BG} =15 V. Here the dark region at zero bias marks the "minigap" at around V_{SD} =250 μV. Within the measurement resolution, there seem to be no changes in bias of this feature. This diverges from the splitting observed in chapter 5. Understanding this characteristic in terms of the semiclassical ABS model (equation 5.6) would require an extremely small magnetic field dependence which could be obtained by a large path length and small loop areas, causing the second term of equation 5.6 to be negligible.
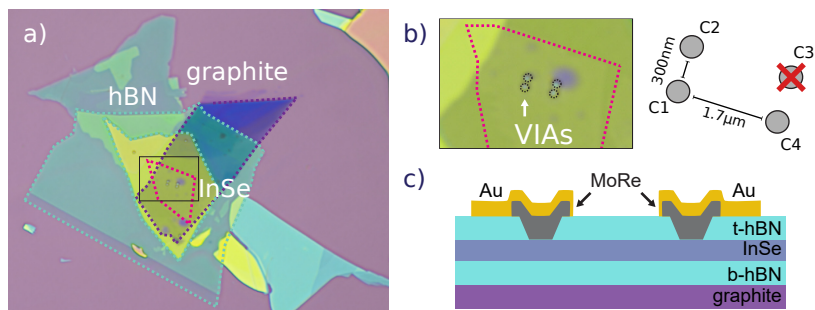
6.2. MoRe VIAS to few layers InSe

Figure 6.3. MoRe VIA contacts to InSe a) Optical lithography of the device surface, indicating flakes. b) Zoom showing VIA contacts a schematic of the distance between contacts. c) Schematic of the vertical cross-section of the heterostructure.

In this section, we demonstrate the versatility of VIA contacts by applying to a different 2D semiconductor, InSe. Although InSe has a different band structure and crystal lattice we obtain qualitatively similar results to the MoS$_2$ devices.

6.2.1. Fabrication

We fabricate an encapsulated multilayer ($\sim$3L) InSe device with MoRe VIA contacts. The hBN containing the MoRe VIAs belong to the same batch as for device II, containing contacts spaced by 300 nm and 1.7 μm spacing between pairs, shown in Figure 6.3 b) and schematic cross section in c). All the other fabrication parameters match device II. The contact yield is about 70%. Two samples were produced with reproducible results. The measurements presented here were performed at 60 mK.

6.2.2. Superconducting gap spectroscopy

We measure the conductance of the device using standard lock-in technique, with sinusoidal voltage modulation of frequency 77 Hz. The first observation is that depending on the contact pairs chosen for measurements, the conductance presents suppression starting at either $V_{SD} =1.2\,\text{mV}$ (for contacts C1-C2 and C2-C4) or $V_{SD} =2.4\,\text{mV}$ (for contacts C1-C2), as shown in Figure 6.4 a) and b). Which reproduce the characteristics of devices I and II in chapter 5 in a single device. We also note that the conductance is always reduced once contact C2 is in use. Our interpretation is that contact C2 has a lower interface transparency compared to C1 and C4 and once it is in use in a two-terminal measurement, most of the voltage drops happen at it dominating the transport features.
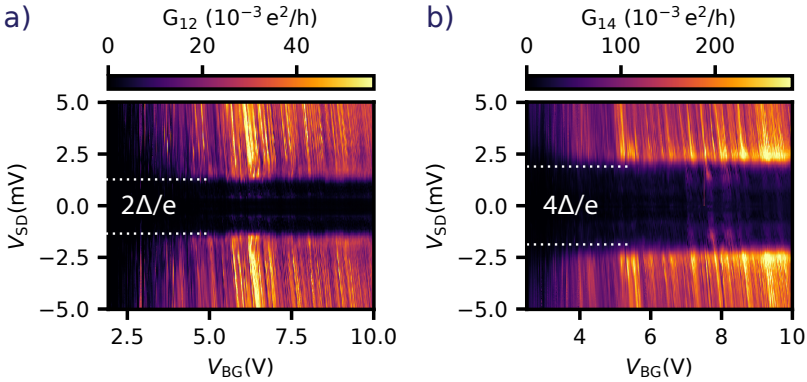

Figure 6.4. Conductance as a function of V_{BG} and V_{SD} for a) contacts C1-C2 b) contacts C1-C4.

For all contact configurations, we observe conductance resonances. The slope of the resonances here is steeper and the density of the lines is higher than the MoS_2 devices[1]. Also, the visibility here is more pronounced, $\Delta G/\overline{G} \sim 0.4$. While the slope is associated with the coupling to source and drain as discussed in appendix C, the density of the resonances and the visibility are given by the wavefunction interference with disorder in the 2DEG. Denser resonance spacing results in a larger apparent cavity length, given by equation 5.4. This could suggest a larger spacing between scatterers or a longer ℓ_{mfp} for the InSe device compared to MoS_2. We understand the higher visibility of the resonances as stronger localization of the quasiparticles in InSe, which is

---

[1]This comparison is only possible since the dielectric hBN flakes used in these heterostructures has a roughly similar thickness on the plate capacitor model.

expected for $m^*_{InSe} < m^*_{MoS_2}$.

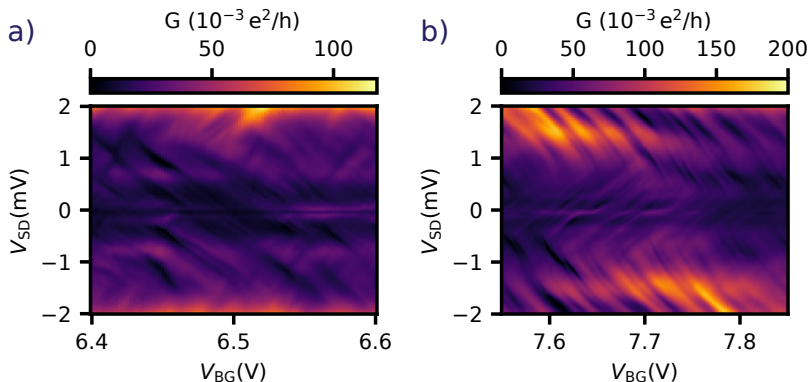### 6.2.3. Sub-gap peaks and magnetic field dependence

Figure 6.5. Sub-gap peaks for contacts C1-C2. Conductance as a function of V_{BG} and V_{SD} at two different V_{BG} ranges. a) Finite bias peaks from 6.4 V to 6.6 V b) A zero bias peak extending from 7.6 to 7.8 V.

Now we focus on the sub-gap peaks for contacts C1-C4. The data for contact pair C1-C2 can be found in appendix D.

Figure 6.5 shows the conductance for a lower bias range, $|V_{SD}| = 2$ mV as a function of V_{BG} at two backgate voltage ranges, from 6.4 V to 6.6 V and 7.6 V to 7.8 V. For most of V_{BG} we observe a "minigap" shown in Figure 6.5 a), with finite bias peaks (FBP) and a suppression at zero bias. But for a few irregular segments of V_{BG}, e.g. 7.6 V to 7.8 V, we observe the formation of a single peak at zero bias voltage (ZBP), as in 6.5 b). The same ZPB is also present at from $V_{BG} = 7$ V to 7.1 V.

The difference between FBP and ZBP is more clear in Figure 6.6, where we plot the average conductance for each V_{SD} value over the V_{BG} ranges in Figure 6.5. The FBP (blue curve) are located around $V_{SD} = 20\,\mu$V, accompanied by side peaks at $V_{SD} = 250\,\mu$V. The ZBP is accompanied by a modulation at $V_{SD} = 1.5$ mV.

The magnetic field evolution of these low bias peaks is shown in Figure 6.7 for a backgate voltage cross sections at $V_{BG} = 6.55$ V, representing a region of FBP and $V_{BG} = 7.05$ V for a region of ZPB.

For the ZBP case, in Figure 6.7 b) we note a splitting into two peaks moving to higher bias values as the magnetic field increases. For the FBP case, Figure 6.7 a), the peaks move *only* to higher bias values as the magnetic field increases.
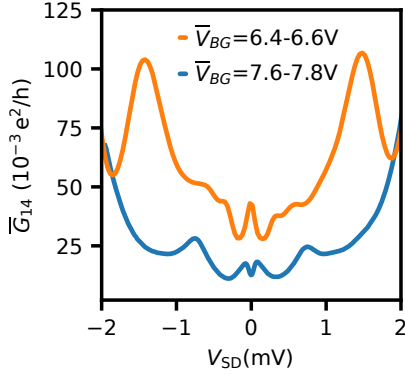
Figure 6.6. Average conductance as a function of V_{SD} for the backgate ranges indicated.

This is contrasting to the MoS_2 data in chapter 5, where we observe a spitting moving simultaneously to higher and lower bias values. Additionally, there is no crossing at zero bias for finite magnetic fields as seen for device II in chapter 5.

We sweep the magnetic field to negative values, to check for small offsets that would push the crossing of the FBP to negative values. We did not observe a crossing except for smearing at zero bias, which is hysteretic in the sweep direction.

At $B \sim 2.5\,\text{T}$ these peaks fade into the background conductance. The data up to $9\,\text{T}$ magnetic field and at a larger bias range is shown in appendix D. For both cases, the slope in magnetic field is similar under the measurement resolution of $\sim 64\,\mu\text{V/T}$, correspondent to a Landé g-factor $g \sim 2.2$.

The presence of FBP at zero magnetic field is clear in terms of equation 5.6 as discussed for device II. However, in our experiments, we only observe an increase of the energy peaks in bias voltage as a function of magnetic field, which contradicts the opposite of the field dependence. Additionally, the presence of a ZBP can only be justified if the path length L increases such that the minigap is smaller than our experiment resolution.
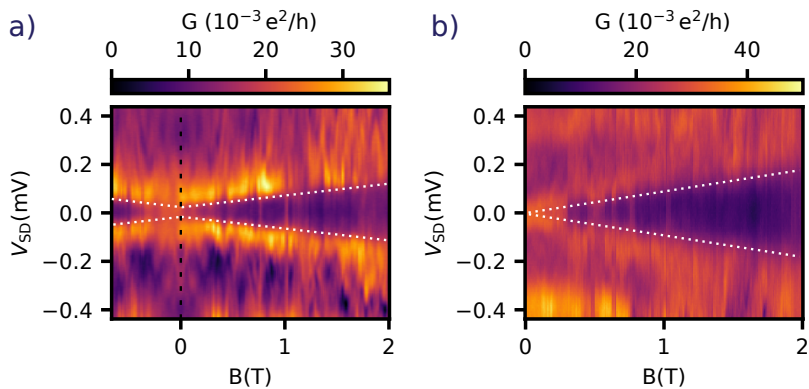
Figure 6.7. Evolution of the low bias peaks in magnetic field. Conductance as function of B and V_{SD} for a) finite bias peaks at $V_{BG} =6.55\,$V b) zero bias peaks at $V_{BG} =7.05\,$V. White dashed lines are guides to the eye.

6.3. Outlook

In conclusion, we successfully fabricated MoRe VIA contacts to a few layers InSe and obtained similar results to MoS_2. This demonstrates the versatility of the contacting method. The sub-gap peaks and their evolution in field is discussed in terms of the semi-classical picture provided in chapter 5, but present a few divergences, that do not match the model.

7 Conclusion and Outlook

The goal of this thesis was to develop and investigate the electronic transport on planar superconductor-semiconductor hybrid devices, employing two-dimensional semiconductors such as TMDCs and others.

The focus was a proximity region between superconducting leads connected to a two-dimensional weak link. The main challenges were a reliable contacting method that would provide low Schottky barrier and coherent electron transport through the interface. Throughout the project, we investigate different contacting techniques and materials to overcome Schottky barrier and optimize the interface cleanliness between electrodes and semiconductors. Using semimetallic bismuth, we were able to reproduce the low contact resistance reported in a very recent publication, but employing such materials in combination with a superconducting film proved not straightforward. No effects of superconductivity were observed suggesting the bismuth might not be suitable, but not discarding the use of other semimetals.

The VIA contacting method using MoRe resulted in devices with excellent electron mobilities and coherent tunneling of quasiparticles through the N-S interfaces, which provides spectroscopy measurements of the superconducting gap. We also observe quantum interference phenomena rising from the quasiparticle wavefunctions interaction with the disorder in the system. By analyzing the properties of these interferences, we obtain indications of electron hole transport and formation of Andreev Bound states in the sub-gap regime. A simple semi-classical model provides qualitative understanding of the evolution of sub-gap states in magnetic field. These results show solid steps towards Josephson physics in 2D materials.

Additionally, we aimed to develop reliable local field effect gating, useful for probing and manipulating quasiparticle states. This was realized by introducing narrow constriction in monolayer MoS_2. We demonstrate well-defined, quantized steps in conductance. The identification of the conductance steps showed to be more problematic than for example in high-mobility GaAs, because the 2D material adjacent to the QPC cannot be neglected and requires a more in-depth analysis, which we discuss with a simple electrostatics model. By studying the discrete energy levels we were to infer properties of the confining potential. The magnetic field dependence suggested degeneracy of spin rather than valley degree of freedom.

As an outlook, we expect 2D semiconductors to be a viable platform for hybrid devices with exciting prospects of spin and valley degrees of freedom. Further improvements in the channel length using the current MoRe VIA architecture could lead to coherent effects connecting the two interfaces. The established gate defined nanostructure could be used to probe the proximitized region, providing insights of reflection coefficients at the N-S interfaces. Future investigations should also focus on improving the interface transparency. Although our results with Bi-Al devices were not promising there are other semimetals that could be investigated, e.g. Sb or α-phase Sn. Although the latter is known for being an unstable phase, it also possesses intrinsic superconductivity at low temperatures which is a considerable advantage. Once the superconducting proximity effect is established in a considerable region, the nanostructrures could be easily adapted to quantum dots and used in Cooper pair splitting experiments. A planar gate tunable Josephson junction with spin and valley degree of freedom and strong spin-orbit interaction could be an exciting platform for quantum circuits as qubits or for the investigation of exotic topological states.

7

Bibliography

[1] G. E. Moore, Electronics Magazine **38** (1965).

[2] G. E. Moore, IEEE Solid-State Circuits Society Newsletter **11**, 36 (2006).

[3] T. D. Ladd, F. Jelezko, R. Laflamme, Y. Nakamura, C. Monroe, and J. L. O'Brien, Nature **464**, 45 (2010).

[4] E. Pednault, J. A. Gunnels, G. Nannicini, L. Horesh, and R. Wisnieff, "Leveraging secondary storage to simulate deep 54-qubit sycamore circuits," (2019), arXiv:1910.09534 [quant-ph] .

[5] H.-S. Zhong, H. Wang, Y.-H. Deng, M.-C. Chen, L.-C. Peng, Y.-H. Luo, J. Qin, D. Wu, X. Ding, Y. Hu, P. Hu, X.-Y. Yang, W.-J. Zhang, H. Li, Y. Li, X. Jiang, L. Gan, G. Yang, L. You, Z. Wang, L. Li, N.-L. Liu, C.-Y. Lu, and J.-W. Pan, Science **370**, 1460 (2020).

[6] V. Mourik, K. Zuo, S. M. Frolov, S. R. Plissard, E. P. A. M. Bakkers, and L. P. Kouwenhoven, Science **336**, 1003 (2012).

[7] C. Beenakker, Annual Review of Condensed Matter Physics **4**, 113 (2013).

[8] L. Fu and C. L. Kane, Phys. Rev. B **79**, 161408 (2009).

[9] F. Ronetti, D. Loss, and J. Klinovaja, Phys. Rev. B **103**, 235410 (2021).

[10] M. M. Leivo, J. P. Pekola, and D. V. Averin, Applied Physics Letters **68**, 1996 (1996).

[11] A. Bordoloi, V. Zannier, L. Sorba, C. Schönenberger, and A. Baumgartner, Nature **612**, 454 (2022).

[12] T. W. Larsen, K. D. Petersson, F. Kuemmeth, T. S. Jespersen, P. Krogstrup, J. Nygård, and C. M. Marcus, Phys. Rev. Lett. **115**, 127001 (2015).

[13] E. Marchiori, L. Ceccarelli, N. Rossi, G. Romagnoli, J. Herrmann, J.-C. Besse, S. Krinner, A. Wallraff, and M. Poggio, Applied Physics Letters **121** (2022), 10.1063/5.0103597.

[14] K.-Y. Kang, I. Song, Y. S. Ha, S.-K. Han, G. Y. Sung, I.-H. Song, and G. Park, IEEE Transactions on Applied Superconductivity **9**, 3074 (1999).

[15] L. Fritzsch, M. Schubert, G. Wende, and H.-G. Meyer, Applied Physics Letters **73**, 1583 (1998).

[16] C. Ciaccia, R. Haller, A. C. C. Drachmann, C. Schrade, T. Lindemann, M. J. Manfra, and C. Schönenberger, "Gate tunable josephson diode in proximitized inas supercurrent interferometers," (2023), arXiv:2304.00484 [cond-mat.mes-hall] .

[17] C. Jünger, S. Lehmann, K. A. Dick, C. Thelander, C. Schönenberger, and A. Baumgartner, "Intermediate states in andreev bound state fusion," (2021), arXiv:2111.00651 [cond-mat.mes-hall] .

[18] K. S. Novoselov, A. K. Geim, S. V. Morozov, D. Jiang, Y. Zhang, S. V. Dubonos, I. V. Grigorieva, and A. A. Firsov, Science **306**, 666 (2004).

[19] M. Ashton, J. Paul, S. B. Sinnott, and R. G. Hennig, Phys. Rev. Lett. **118**, 106101 (2017).

[20] M. C. Lemme, D. Akinwande, C. Huyghebaert, and C. Stampfer, Nature Communications **13**, 1392 (2022).

[21] D. Akinwande, C. Huyghebaert, C.-H. Wang, M. I. Serna, S. Goossens, L.-J. Li, H.-S. P. Wong, and F. H. L. Koppens, Nature **573**, 507 (2019).

[22] S. Manzeli, D. Ovchinnikov, D. Pasquier, O. V. Yazyev, and A. Kis, Nature Reviews Materials **2**, 17033 (2017).

[23] A. L. R. Manesco and A. Pulkin, "Spatial separation of spin currents in transition metal dichalcogenides," (2023), arXiv:2206.07333 [cond-mat.mes-hall] .

[24] A. K. Geim and I. V. Grigorieva, Nature **499**, 419 (2013).

[25] Y. Cao, V. Fatemi, S. Fang, K. Watanabe, T. Taniguchi, E. Kaxiras, and P. Jarillo-Herrero, Nature **556**, 43 (2018).

[26] D. I. Indolese, P. Karnatak, A. Kononov, R. Delagrange, R. Haller, L. Wang, P. Makk, K. Watanabe, T. Taniguchi, and C. Schönenberger, Nano Letters **20**, 7129 (2020).

[27] A. Kononov, M. Endres, G. Abulizi, K. Qu, J. Yan, D. G. Mandrus, K. Watanabe, T. Taniguchi, and C. Schönenberger, Journal of Applied Physics **129** (2021), 10.1063/5.0021350.

[28] F. Telesio, M. Carrega, G. Cappelli, A. Iorio, A. Crippa, E. Strambini, F. Giazotto, M. Serrano-Ruiz, M. Peruzzini, and S. Heun, ACS Nano **16**, 3538 (2022).

[29] D. J. Trainer, B. Wang, F. Bobba, N. Samuelson, X. Xi, J. Zasadzinski, J. Nieminen, A. Bansil, and M. Iavarone, ACS Nano **14**, 2718 (2020).

[30] E. Mikheev, I. T. Rosen, and D. Goldhaber-Gordon, Science Advances **7**, eabi6520 (2021).

[31] H. van Houten and C. Beenakker, Physica B: Condensed Matter **175**, 187 (1991).

[32] T. Ihn, *Semiconductor Nanostructures: Quantum States and Electronic Transport* (Oxford University Press, Oxford, 2010).

[33] V. Umansky, R. de Picciotto, and M. Heiblum, Applied Physics Letters **71**, 683 (1997).

[34] J. Shabani, M. Kjaergaard, H. J. Suominen, Y. Kim, F. Nichele, K. Pakrouski, T. Stankevic, R. M. Lutchyn, P. Krogstrup, R. Feidenhans'l, S. Kraemer, C. Nayak, M. Troyer, C. M. Marcus, and C. J. Palmstrøm, Phys. Rev. B **93**, 155402 (2016).

[35] B. Radisavljevic, A. Radenovic, J. Brivio, V. Giacometti, and A. Kis, Nature Nanotechnology **6**, 147 (2011).

[36] Z. Wang and B. Mi, Environmental Science & Technology **51**, 8229 (2017).

[37] Z. Wu, B. T. Zhou, X. Cai, P. Cheung, G.-B. Liu, M. Huang, J. Lin, T. Han, L. An, Y. Wang, S. Xu, G. Long, C. Cheng, K. T. Law, F. Zhang, and N. Wang, Nature Communications **10**, 611 (2019).

[38] A. Kormányos, V. Zólyomi, N. D. Drummond, and G. Burkard, Phys. Rev. X **4**, 011034 (2014).

[39] R. Pisoni, A. Kormányos, M. Brooks, Z. Lei, P. Back, M. Eich, H. Overweg, Y. Lee, P. Rickhaus, K. Watanabe, T. Taniguchi, A. Imamoglu, G. Burkard, T. Ihn, and K. Ensslin, Phys. Rev. Lett. **121**, 247701 (2018).

[40] T. Y. T. Hung, K. Y. Camsari, S. Zhang, P. Upadhyaya, and Z. Chen, Science Advances **5**, eaau6478 (2019).

[41] S. Liu, Y. Liu, L. N. Holtzman, B. Li, M. Holbrook, J. Pack, T. Taniguchi, K. Watanabe, C. R. Dean, A. Pasupathy, K. Barmak, D. A. Rhodes, and J. Hone, "Two-step flux synthesis of ultrapure transition metal dichalcogenides," (2023), arXiv:2303.16290 [cond-mat.mtrl-sci] .

[42] J. G. Roch, G. Froehlicher, N. Leisgang, P. Makk, K. Watanabe, T. Taniguchi, and R. J. Warburton, Nature Nanotechnology **14**, 432 (2019).

[43] D. Costanzo, S. Jo, H. Berger, and A. F. Morpurgo, Nature Nanotechnology **11**, 339 (2016).

[44] M.-H. Shang, H. Hou, J. Zheng, Z. Yang, J. Zhang, S. Wei, X. Duan, and W. Yang, The Journal of Physical Chemistry Letters **9**, 6032 (2018).

[45] C. Kong, Y.-X. Han, L. jie Hou, and P.-J. Yan, International Journal of Hydrogen Energy **47**, 242 (2022).

[46] D. Liu, Y. Guo, L. Fang, and J. Robertson, Applied Physics Letters **103**, 183113 (2013).

[47] A. K. Dash, H. Swaminathan, E. Berger, M. Mondal, T. Lehenkari, P. R. Prasad, K. Watanabe, T. Taniguchi, H.-P. Komsa, and A. Singh, 2D Materials **10**, 035002 (2023).

[48] J. Hu, L. Yu, J. Deng, Y. Wang, K. Cheng, C. Ma, Q. Zhang, W. Wen, S. Yu, Y. Pan, J. Yang, H. Ma, F. Qi, Y. Wang, Y. Zheng, M. Chen, R. Huang, S. Zhang, Z. Zhao, J. Mao, X. Meng, Q. Ji, G. Hou, X. Han, X. Bao, Y. Wang, and D. Deng, Nature Catalysis **4**, 242 (2021).

[49] D. A. Bandurin, A. V. Tyurnina, G. L. Yu, A. Mishchenko, V. Zólyomi, S. V. Morozov, R. K. Kumar, R. V. Gorbachev, Z. R. Kudrynskyi, S. Pezzini, Z. D. Kovalyuk, U. Zeitler, K. S. Novoselov, A. Patanè, L. Eaves, I. V. Grigorieva, V. I. Fal'ko, A. K. Geim, and Y. Cao, Nature Nanotechnology **12**, 223 (2017).

[50] M. Wasala, H. I. Sirikumara, Y. Raj Sapkota, S. Hofer, D. Mazumdar, T. Jayasekera, and S. Talapatra, J. Mater. Chem. C **5**, 11214 (2017).

[51] J. Jiang, L. Xu, C. Qiu, and L.-M. Peng, Nature **616**, 470 (2023).

[52] H. Cai, Y. Gu, Y.-C. Lin, Y. Yu, D. B. Geohegan, and K. Xiao, Applied Physics Reviews **6** (2019), 10.1063/1.5123487.

[53] D. Shcherbakov, P. Stepanov, S. Memaran, Y. Wang, Y. Xin, J. Yang, K. Wei, R. Baumbach, W. Zheng, K. Watanabe, T. Taniguchi, M. Bockrath, D. Smirnov, T. Siegrist, W. Windl, L. Balicas, and C. N. Lau, Science Advances **7**, eabe2892 (2021).

[54] M. Hamer, E. Tóvári, M. Zhu, M. D. Thompson, A. Mayorov, J. Prance, Y. Lee, R. P. Haley, Z. R. Kudrynskyi, A. Patanè, D. Terry, Z. D. Kovalyuk, K. Ensslin, A. V. Kretinin, A. Geim, and R. Gorbachev, Nano Letters **18**, 3950 (2018).

[55] Y. Lee, R. Pisoni, H. Overweg, M. Eich, P. Rickhaus, A. Patanè, Z. R. Kudrynskyi, Z. D. Kovalyuk, R. Gorbachev, K. Watanabe, T. Taniguchi, T. Ihn, and K. Ensslin, 2D Materials **5** (2018), 10.1088/2053-1583/aacb49.

[56] S. Tao, X. Zhang, J. Zhu, P. He, S. A. Yang, Y. Lu, and S.-H. Wei, Journal of the American Chemical Society **144**, 3949 (2022).

[57] J. Chen, Journal of Physics and Chemistry of Solids **125**, 23 (2019).

[58] Y. Ma, Y. Dai, L. Yu, C. Niu, and B. Huang, New Journal of Physics **15**, 073008 (2013).

[59] S. Sze and K. K.N., *Physics of Semiconductor Devices* (John Wiley and Sons, Inc., 2006).

[60] Y. Wang and M. Chhowalla, Nature Reviews Physics **4**, 101 (2022).

[61] S. McDonnell, C. Smyth, C. L. Hinkle, and R. M. Wallace, ACS Applied Materials & Interfaces **8**, 8289 (2016).

[62] C. M. Smyth, R. Addou, S. McDonnell, C. L. Hinkle, and R. M. Wallace, The Journal of Physical Chemistry C **120**, 14719 (2016).

[63] C. M. Smyth, R. Addou, C. L. Hinkle, and R. M. Wallace, The Journal of Physical Chemistry C **123**, 23919 (2019).

[64] M. Endres, A. Kononov, M. Stiefel, M. Wyss, H. S. Arachchige, J. Yan, D. Mandrus, K. Watanabe, T. Taniguchi, and C. Schönenberger, Phys. Rev. Mater. **6**, L081201 (2022).

[65] M. Bai, F. Yang, M. Luysberg, J. Feng, A. Bliesener, G. Lippertz, A. A. Taskin, J. Mayer, and Y. Ando, Phys. Rev. Mater. **4**, 094801 (2020).

[66] Y. Liu, J. Guo, E. Zhu, L. Liao, S.-J. Lee, M. Ding, I. Shakir, V. Gambin, Y. Huang, and X. Duan, Nature **557**, 696 (2018).

[67] Q. H. Thi, H. Kim, J. Zhao, and T. H. Ly, npj 2D Materials and Applications **2**, 34 (2018).

[68] T. Y. Jeong, H. Kim, S.-J. Choi, K. Watanabe, T. Taniguchi, K. J. Yee, Y.-S. Kim, and S. Jung, Nature Communications **10**, 3825 (2019).

[69] C. Kim, I. Moon, D. Lee, M. S. Choi, F. Ahmed, S. Nam, Y. Cho, H.-J. Shin, S. Park, and W. J. Yoo, ACS Nano **11**, 1588 (2017).

[70] Q. Yue, J. Kang, Z. Shao, X. Zhang, S. Chang, G. Wang, S. Qin, and J. Li, Physics Letters A **376**, 1166 (2012).

[71] J. Pető, G. Dobrik, G. Kukucska, P. Vancsó, A. A. Koós, J. Koltai, P. Nemes-Incze, C. Hwang, and L. Tapasztó, npj 2D Materials and Applications **3**, 39 (2019).

[72] K. Gołasa, M. Grzeszczyk, J. Binder, R. Bożek, A. Wysmołek, and A. Babiński, AIP Advances **5**, 077120 (2015).

[73] C. Zhang, M.-Y. Li, J. Tersoff, Y. Han, Y. Su, L.-J. Li, D. A. Muller, and C.-K. Shih, Nature Nanotechnology **13**, 152 (2018).

[74] P.-C. Shen, C. Su, Y. Lin, A.-S. Chou, C.-C. Cheng, J.-H. Park, M.-H. Chiu, A.-Y. Lu, H.-L. Tang, M. M. Tavakoli, G. Pitner, X. Ji, Z. Cai, N. Mao, J. Wang, V. Tung, J. Li, J. Bokor, A. Zettl, C.-I. Wu, T. Palacios, L.-J. Li, and J. Kong, Nature **593**, 211 (2021).

[75] K. Sotthewes, R. van Bremen, E. Dollekamp, T. Boulogne, K. Nowakowski, D. Kas, H. J. W. Zandvliet, and P. Bampoulis, J Phys Chem C Nanomater Interfaces **123**, 5411 (2019).

[76] Y. Liu, P. Stradins, and S.-H. Wei, Science Advances **2**, e1600069 (2016).

[77] M. Farmanbar and G. Brocks, Phys. Rev. B **93**, 085304 (2016).

[78] R. T. Tung, Phys. Rev. B **64**, 205310 (2001).

[79] W. Li, X. Gong, Z. Yu, L. Ma, W. Sun, S. Gao, Ç. Köroğlu, W. Wang, L. Liu, T. Li, H. Ning, D. Fan, Y. Xu, X. Tu, T. Xu, L. Sun, W. Wang, J. Lu, Z. Ni, J. Li, X. Duan, P. Wang, Y. Nie, H. Qiu, Y. Shi, E. Pop, J. Wang, and X. Wang, Nature **613**, 274 (2023).

[80] D. Somvanshi, S. Kallatt, C. Venkatesh, S. Nair, G. Gupta, J. K. Anthony, D. Karmakar, and K. Majumdar, Phys. Rev. B **96**, 205423 (2017).

[81] C. D. English, G. Shine, V. E. Dorgan, K. C. Saraswat, and E. Pop, Nano Letters **16**, 3824 (2016).

[82] Q. Smets, B. Groven, M. Caymax, I. P. Radu, G. Arutchelvan, J. Jussot, D. Verreck, I. Asselberghs, A. N. Mehta, A. Gaur, D. Lin, and S. E. Kazzi, 2019 IEEE International Electron Devices Meeting (IEDM) , 23.2.1 (2019).

[83] E. Ber, R. W. Grady, E. Pop, and E. Yalon, "Pinpointing the dominant component of contact resistance to atomically thin semiconductors," (2021), arXiv:2110.02563 [physics.app-ph] .

[84] H. Liu, M. Si, Y. Deng, A. T. Neal, Y. Du, S. Najmaei, P. M. Ajayan, J. Lou, and P. D. Ye, ACS Nano **8**, 1031 (2014).

[85] J. Kang, W. Liu, D. Sarkar, D. Jena, and K. Banerjee, Phys. Rev. X **4**, 031005 (2014).

[86] G. Arutchelvan, C. J. Lockhart de la Rosa, P. Matagne, S. Sutar, I. Radu, C. Huyghebaert, S. De Gendt, and M. Heyns, Nanoscale **9**, 10869 (2017).

[87] A. Szabo, A. Jain, M. Parzefall, L. Novotny, and M. Luisier, Nano Letters **19**, 3641 (2019).

[88] Z. Cheng, J. Backman, H. Zhang, H. Abuzaid, G. Li, Y. Yu, L. Cao, A. V. Davydov, M. Luisier, C. A. Richter, and A. D. Franklin, Advanced Materials **n/a**, 2210916 (2023).

[89] M. Poljak, M. Matić, and A. Zeljko, IEEE Electron Device Letters **42**, 1240 (2021).

[90] M. Brahma, M. L. Van de Put, E. Chen, M. V. Fischetti, and W. G. Vandenberghe, in *2021 International Conference on Simulation of Semiconductor Processes and Devices (SISPAD)* (2021) pp. 175–179.

[91] A. Seredinski, E. G. Arnault, V. Z. Costa, L. Zhao, T. F. Q. Larson, K. Watanabe, T. Taniguchi, F. Amet, A. K. M. Newaz, and G. Finkelstein, AIP Advances **11**, 045312 (2021).

[92] B. J. van Wees, H. van Houten, C. W. J. Beenakker, J. G. Williamson, L. P. Kouwenhoven, D. van der Marel, and C. T. Foxon, Phys. Rev. Lett. **60**, 848 (1988).

[93] D. A. Wharam, T. J. Thornton, R. Newbury, M. Pepper, H. Ahmed, J. E. F. Frost, D. G. Hasko, D. C. Peacock, D. A. Ritchie, and G. A. C. Jones, Journal of Physics C: Solid State Physics **21**, L209 (1988).

[94] M. Büttiker, Phys. Rev. B **41**, 7906 (1990).

[95] T. T. Heikkila, *The Physics of Nanoelectronics: Transport and Fluctuation Phenomena at Low Temperatures* (Oxford University Press, 2013).

[96] S. Datta, *Electronic Transport in Mesoscopic Systems*, Cambridge Studies in Semiconductor Physics and Microelectronic Engineering (Cambridge University Press, 1995).

[97] A. Bordoloi, *Spin Projection and Correlation Experiments in Nanoelectronic Devices*, Phd thesis, University of Basel, Basel (2021), `https://edoc.unibas.ch/84831/`.

[98] H. Kamerlingh Onnes, Commun. Phys. Lab. Univ. Leiden , 120b,122b (1911).

[99] W. Meissner and R. Ochsenfeld, Naturwissenschaften **21**, 787 (1933).

[100] F. London, H. London, and F. A. Lindemann, Proceedings of the Royal Society of London. Series A - Mathematical and Physical Sciences **149**, 71 (1935).

[101] J. Bardeen, L. N. Cooper, and J. R. Schrieffer, Phys. Rev. **106**, 162 (1957).

[102] V. L. Ginzburg and L. D. Landau, "On the theory of superconductivity," in *On Superconductivity and Superfluidity: A Scientific Autobiography* (Springer Berlin Heidelberg, Berlin, Heidelberg, 2009) pp. 113–137.

[103] M. Tinkham, *Introduction to Superconductivity*, Dover Books on Physics Series (Dover Publications, 2004).

[104] B. Josephson, Physics Letters **1**, 251 (1962).

[105] P. W. Anderson and J. M. Rowell, Phys. Rev. Lett. **10**, 230 (1963).

[106] R. Gross, A. Marx, and F. Deppe, *Applied Superconductivity: Josephson Effect and Superconducting Electronics*, De Gruyter Textbook (De Gruyter, 2016).

[107] G. E. Blonder, M. Tinkham, and T. M. Klapwijk, Phys. Rev. B **25**, 4515 (1982).

[108] T. M. Klapwijk, Journal of Superconductivity **17**, 593 (2004).

[109] V. Ambegaokar and A. Baratoff, Phys. Rev. Lett. **11**, 104 (1963).

[110] P. F. Bagwell, Phys. Rev. B **46**, 12573 (1992).

[111] C. Jünger, A. Baumgartner, R. Delagrange, D. Chevallier, S. Lehmann, M. Nilsson, K. A. Dick, C. Thelander, and C. Schönenberger, Communications Physics **2**, 76 (2019).

[112] B. J. van Wees, P. de Vries, P. Magnée, and T. M. Klapwijk, Phys. Rev. Lett. **69**, 510 (1992).

[113] A. Kastalsky, A. W. Kleinsasser, L. H. Greene, R. Bhat, F. P. Milliken, and J. P. Harbison, Phys. Rev. Lett. **67**, 3026 (1991).

[114] M. Schechter, Y. Imry, and Y. Levinson, Phys. Rev. B **64**, 224513 (2001).

[115] D. Indolese, *Engineered graphene Josephson junctions probed by quantum interference effects*, Phd thesis, University of Basel, Basel (2021), `https://edoc.unibas.ch/81789/`.

[116] Q. Zhao, S. Puebla, W. Zhang, T. Wang, R. Frisenda, and A. Castellanos-Gomez, Advanced Photonics Research **1**, 2000025 (2020).

[117] Y. Anzai, M. Yamamoto, S. Genchi, K. Watanabe, T. Taniguchi, S. Ichikawa, Y. Fujiwara, and H. Tanaka, Applied Physics Express **12**, 055007 (2019).

[118] A. Castellanos-Gomez, M. Buscema, R. Molenaar, V. Singh, L. Janssen, H. S. J. van der Zant, and G. A. Steele, 2D Materials **1**, 011002 (2014).

[119] P. Kumar, K. S. Figueroa, A. C. Foucher, K. Jo, N. Acero, E. A. Stach, and D. Jariwala, Journal of Vacuum Science & Technology A **39**, 032201 (2021).

[120] X. Cui, G.-H. Lee, Y. D. Kim, G. Arefe, P. Y. Huang, C.-H. Lee, D. A. Chenet, X. Zhang, L. Wang, F. Ye, F. Pizzocchero, B. S. Jessen, K. Watanabe, T. Taniguchi, D. A. Muller, T. Low, P. Kim, and J. Hone, Nature Nanotechnology **10**, 534 (2015).

[121] S. Davari, J. Stacy, A. Mercado, J. Tull, R. Basnet, K. Pandey, K. Watanabe, T. Taniguchi, J. Hu, and H. Churchill, Phys. Rev. Appl. **13**, 054058 (2020).

[122] S. Chen, J. Son, S. Huang, K. Watanabe, T. Taniguchi, R. Bashir, A. M. van der Zande, and W. P. King, ACS Omega **6**, 4013 (2021).

[123] M. Ramezani, *Superconducting contacts and quantum interference phenomena in monolayer semiconductor devices*, Phd thesis, University of Basel, Basel (2022), https://edoc.unibas.ch/90187/.

[124] L. Wang, I. Meric, P. Y. Huang, Q. Gao, Y. Gao, H. Tran, T. Taniguchi, K. Watanabe, L. M. Campos, D. A. Muller, J. Guo, P. Kim, J. Hone, K. L. Shepard, and C. R. Dean, Science **342**, 614 (2013).

[125] H. Choi, B. H. Moon, J. H. Kim, S. J. Yun, G. H. Han, S.-g. Lee, H. Z. Gul, and Y. H. Lee, ACS Nano **13**, 13169 (2019).

[126] A. Jain, A. Szabo, M. Parzefall, E. Bonvin, T. Taniguchi, K. Watanabe, P. Bharadwaj, M. Luisier, and L. Novotny, Nano Letters **19**, 6914 (2019).

[127] R. Pisoni, Y. Lee, H. Overweg, M. Eich, P. Simonet, K. Watanabe, T. Taniguchi, R. Gorbachev, T. Ihn, and K. Ensslin, Nano Letters **17**, 5008 (2017).

[128] K. Marinov, A. Avsar, K. Watanabe, T. Taniguchi, and A. Kis, Nature Communications **8**, 1938 (2017).

[129] D. Van Tuan, B. Scharf, Z. Wang, J. Shan, K. F. Mak, I. Žutić, and H. Dery, Phys. Rev. B **99**, 085301 (2019).

[130] A. W. Tsen, B. Hunt, Y. D. Kim, Z. J. Yuan, S. Jia, R. J. Cava, J. Hone, P. Kim, C. R. Dean, and A. N. Pasupathy, Nature Physics **12**, 208 (2016).

[131] E. J. Telford, A. Benyamini, D. Rhodes, D. Wang, Y. Jung, A. Zangiabadi, K. Watanabe, T. Taniguchi, S. Jia, K. Barmak, A. N. Pasupathy, C. R. Dean, and J. Hone, Nano Letters **18**, 1416 (2018).

[132] C. Reale, Acta Physica Academiae Scientiarum Hungaricae **37**, 53 (1974).

[133] N. A. Court, A. J. Ferguson, and R. G. Clark, Superconductor Science and Technology **21**, 015013 (2007).

[134] H. K. Kundu, S. Biswas, N. Ofek, V. Umansky, and M. Heiblum, Nature Physics **19**, 515 (2023).

[135] M. A. Topinka, B. J. LeRoy, S. E. J. Shaw, E. J. Heller, R. M. Westervelt, K. D. Maranowski, and A. C. Gossard, Science **289**, 2323 (2000).

[136] T. Ihn, S. Gustavsson, U. Gasser, B. Küng, T. Müller, R. Schleser, M. Sigrist, I. Shorubalko, R. Leturcq, and K. Ensslin, Solid State Communications **149**, 1419 (2009).

[137] J. A. Folk, R. M. Potok, C. M. Marcus, and V. Umansky, Science **299**, 679 (2003).

[138] S.-T. Lo, C.-H. Chen, J.-C. Fan, L. W. Smith, G. L. Creeth, C.-W. Chang, M. Pepper, J. P. Griffiths, I. Farrer, H. E. Beere, G. A. C. Jones, D. A. Ritchie, and T.-M. Chen, Nature Communications **8**, 15997 (2017).

[139] J. Dubois, T. Jullien, F. Portier, P. Roche, A. Cavanna, Y. Jin, W. Wegscheider, P. Roulleau, and D. C. Glattli, Nature **502**, 659 (2013).

[140] M. Hashisaka, Y. Yamauchi, S. Nakamura, S. Kasai, K. Kobayashi, and T. Ono, Journal of Physics: Conference Series **109**, 012013 (2008).

[141] H. van Houten, L. W. Molenkamp, C. W. J. Beenakker, and C. T. Foxon, Semiconductor Science and Technology **7**, B215 (1992).

[142] C. Rossler, K.-D. Hof, S. Manus, S. Ludwig, J. P. Kotthaus, J. Simon, A. W. Holleitner, D. Schuh, and W. Wegscheider, Applied Physics Letters **93** (2008), 10.1063/1.2970035.

[143] T.-M. Chen, M. Pepper, I. Farrer, D. A. Ritchie, and G. A. C. Jones, Applied Physics Letters **103** (2013), 10.1063/1.4819489.

[144] P. Gallagher, M. Lee, J. R. Williams, and D. Goldhaber-Gordon, Nature Physics **10**, 748 (2014).

[145] Y. Takagaki and K. H. Ploog, Phys. Rev. B **60**, 9750 (1999).

[146] K. Wang, K. De Greve, L. A. Jauregui, A. Sushko, A. High, Y. Zhou, G. Scuri, T. Taniguchi, K. Watanabe, M. D. Lukin, H. Park, and P. Kim, Nature Nanotechnology **13**, 128 (2018).

[147] K. Sakanashi, P. Krüger, K. Watanabe, T. Taniguchi, G.-H. Kim, D. K. Ferry, J. P. Bird, and N. Aoki, Nano Letters **21**, 7534 (2021).

[148] C. H. Sharma and M. Thalakulam, Scientific Reports **7**, 735 (2017).

[149] M. Ramezani, I. C. Sampaio, K. Watanabe, T. Taniguchi, C. Schönenberger, and A. Baumgartner, Nano Letters **21**, 5614 (2021).

[150] A. Stern, T. Scaffidi, O. Reuven, C. Kumar, J. Birkbeck, and S. Ilani, Physical Review Letters **129** (2022), 10.1103/physrevlett.129.157701.

[151] Y. V. Sharvin and Yu., Journal of Experimental and Theoretical Physics (1965).

[152] F. Bauer, J. Heyder, E. Schubert, D. Borowsky, D. Taubert, B. Bruognolo, D. Schuh, W. Wegscheider, J. von Delft, and S. Ludwig, Nature **501**, 73 (2013).

[153] S. M. Cronenwett, H. J. Lynch, D. Goldhaber-Gordon, L. P. Kouwenhoven, C. M. Marcus, K. Hirose, N. S. Wingreen, and V. Umansky, Phys. Rev. Lett. **88**, 226805 (2002).

[154] A. C. Graham, K. J. Thomas, M. Pepper, N. R. Cooper, M. Y. Simmons, and D. A. Ritchie, Phys. Rev. Lett. **91**, 136404 (2003).

[155] A. C. Graham, M. Y. Simmons, D. A. Ritchie, and M. Pepper, Phys. Rev. Lett. **100**, 226804 (2008).

[156] L. Banszerus, B. Frohn, T. Fabian, S. Somanchi, A. Epping, M. Müller, D. Neumaier, K. Watanabe, T. Taniguchi, F. Libisch, B. Beschoten, F. Hassler, and C. Stampfer, Phys. Rev. Lett. **124**, 177701 (2020).

[157] L. Weidinger, C. Schmauder, D. H. Schimmel, and J. von Delft, Phys. Rev. B **98**, 115112 (2018).

[158] S. Baer, C. Rössler, E. C. de Wiljes, P.-L. Ardelt, T. Ihn, K. Ensslin, C. Reichl, and W. Wegscheider, Phys. Rev. B **89**, 085424 (2014).

[159] V. Singh, B. H. Schneider, S. J. Bosman, E. P. J. Merkx, and G. A. Steele, Applied Physics Letters **105**, 222601 (2014).

[160] R. C. Dynes, V. Narayanamurti, and J. P. Garno, Phys. Rev. Lett. **41**, 1509 (1978).

[161] S. Skalski, O. Betbeder-Matibet, and P. R. Weiss, Phys. Rev. **136**, A1500 (1964).

[162] J. Gramich, A. Baumgartner, and C. Schönenberger, Applied Physics Letters **108**, 172604 (2016).

[163] J. Gramich, A. Baumgartner, and C. Schönenberger, Phys. Rev. Lett. **115**, 216801 (2015).

[164] Q.-f. Sun, J. Wang, and T.-h. Lin, Phys. Rev. B **59**, 3831 (1999).

[165] S. Sundar, L. S. Sharath Chandra, V. K. Sharma, M. K. Chattopadhyay, and S. B. Roy, AIP Conference Proceedings **1512**, 1092 (2013).

[166] M. T. Allen, O. Shtanko, I. C. Fulga, J. I.-J. Wang, D. Nurgaliev, K. Watanabe, T. Taniguchi, A. R. Akhmerov, P. Jarillo-Herrero, L. S. Levitov, and A. Yacoby, Nano Letters **17**, 7380 (2017).

[167] C. M. Moehle, P. K. Rout, N. A. Jainandunsing, D. Kuiri, C. T. Ke, D. Xiao, C. Thomas, M. J. Manfra, M. P. Nowak, and S. Goswami, Nano Letters **22**, 8601 (2022).

[168] J.-D. Pillet, C. H. L. Quay, P. Morfin, C. Bena, A. L. Yeyati, and P. Joyez, Nature Physics **6**, 965 (2010).

[169] J. Schindele, A. Baumgartner, R. Maurand, M. Weiss, and C. Schönenberger, Phys. Rev. B **89**, 045422 (2014).

[170] J. Gramich, A. Baumgartner, and C. Schönenberger, Phys. Rev. B **96**, 195418 (2017).

[171] C. Beenakker, in *Quantum Dots: a Doorway to Nanoscale Physics* (Springer Berlin Heidelberg, 2005) pp. 131–174.

[172] L. Banszerus, F. Libisch, A. Ceruti, S. Blien, K. Watanabe, T. Taniguchi, A. K. Hüttel, B. Beschoten, F. Hassler, and C. Stampfer, "Minigap and andreev bound states in ballistic graphene," (2021), arXiv:2011.11471 [cond-mat.mes-hall] .

[173] H. Pan and S. Das Sarma, Phys. Rev. Res. **2**, 013377 (2020).

[174] H. Pan and S. Das Sarma, Phys. Rev. B **104**, 054510 (2021).

[175] D. I. Pikulin, J. P. Dahlhaus, M. Wimmer, H. Schomerus, and C. W. J. Beenakker, New Journal of Physics **14**, 125011 (2012).

[176] M. Ben Shalom, M. J. Zhu, V. I. Fal'ko, A. Mishchenko, A. V. Kretinin, K. S. Novoselov, C. R. Woods, K. Watanabe, T. Taniguchi, A. K. Geim, and J. R. Prance, Nature Physics **12**, 318 (2016).

[177] J. Cserti, P. Polinák, G. Palla, U. Zülicke, and C. J. Lambert, Phys. Rev. B **69**, 134514 (2004).

[178] O. Dmytruk, D. Loss, and J. Klinovaja, Phys. Rev. B **102**, 245431 (2020).

A Additional data to QPC device

Additional QPC pinch-off curves

Here we provide additional DC conductance plots as a function of the splitgate voltage for different two backgate voltages. In Figure A.1 a) the number of plateaus at $V_{BG} =2.5\,\text{V}$ is reduced to $N =3$. This is in agreement with the inverse relation between the Fermi wavelength λ_F and the charge carrier concentration. Additionally, we note that this curve does not present the 0.7 anomaly as it is the case for Figure A.1 b) at $V_{BG} =3.6\,\text{V}$.
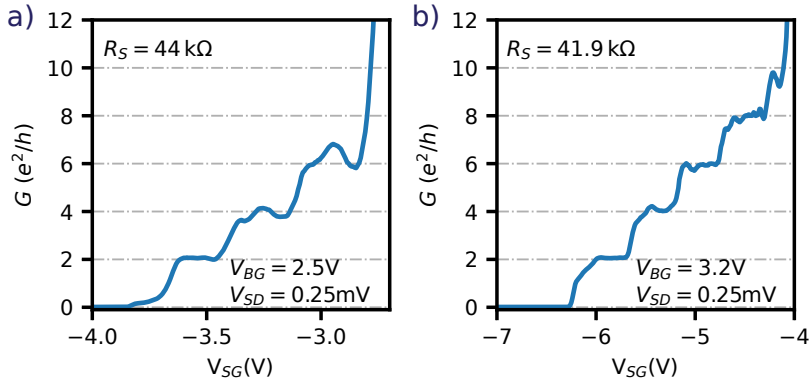

Figure A.1. Conductance as function of the splitgate voltage for a) $V_{BG} =2.5\,\text{V}$ and b) $V_{BG} =3.6\,\text{V}$.

Landau fan diagram

Applying zero voltage to the splitgates we measure the conductance of the device as a function of the backgate voltage V_{BG} and magnetic field B for a voltage bias $V_{SD} =8\,mV$, shown in Figure A.2 a). By fitting a polynomial we extract the background curve, plotted in b). We obtain the two subbands MoS_2 Landau fan as reported by Ref. [39]. For $V_{BG} <3\,V$ a single the lowest subband is occupied generating the fan structure denoted by the green dotted lines. The onset of the lowest subband can be estimated by extrapolating these lines to $B = 0$. With that we obtain $V_{BG} \sim 0.17\,V$. For $V_{BG} >3\,V$ the second subband contributes to transport. The onset is hard to determine by extrapolation due to the broadening of the Landau fan lines. Here we observe SdH oscillations down to $B =5.5\,T$, which sets a lower bound for charge carrier mobility as $\mu_{SdH} \geq 1800\,cm^2/Vs$ in good agreement with the estimated field effect mobility.
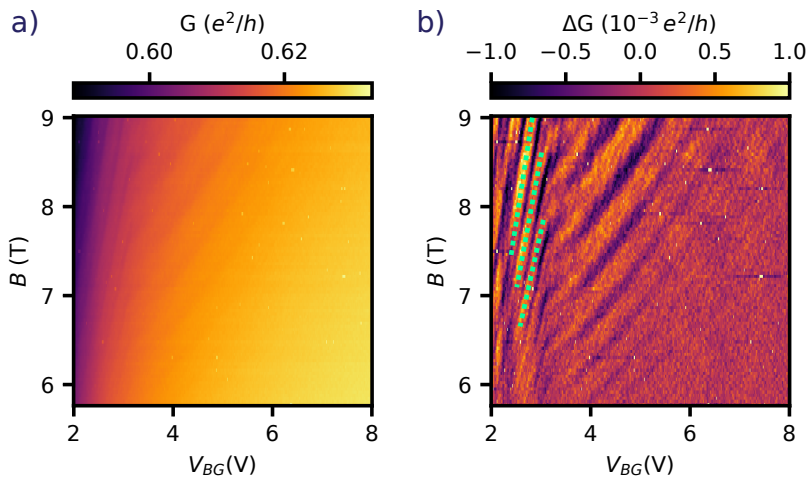

Figure A.2. Raw conductance as a function of V_{BG} and B with no influence from the splitgate. b) Background subtraction reveals the Landau fan diagram of monolayer MoS_2 with two subband contributions.

B Additional data to Device I

Shubnikov de Haas oscillations

In Figure B.1 a) we plot the two terminal conductance through terminals C1-C2 as a function of V_{BG} and B for $V_{SD} = 8\,\mathrm{mV}$. A third-order polynomial background was extracted for each gate voltage to eliminate effects from the classical Hall effect and CB effects. We observe well-developed Shubnikov de Haas oscillations, suggesting a high $\mathrm{MoS_2}$ quality, with an onset at $B_{on} < 4\,\mathrm{T}$, yielding an electron mobility $\mu \geqslant 2500\,\mathrm{cm^2/Vs}$.
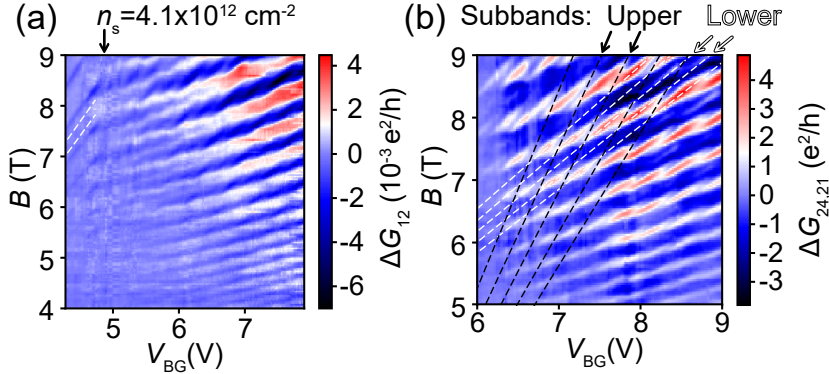

Figure B.1. a) Two-terminal conductance $G_{12} = I_1/V_{SD}$ with $V_{SD} = 8\,\mathrm{mV}$ applied to contact C2, plotted as a function of the magnetic field B and V_{BG} at $60\,\mathrm{mK}$. n_s points out the gate voltage corresponding to the electron density at which the higher spin–orbit subbands start to be populated. b) Three-terminal dc conductance $G_{24,21} = I_2/V_{12}$ with an external bias $V_{SD} = 10\,\mathrm{mV}$ applied to C4, while the current I_2 is measured at C2 and the voltage difference V_{12} between C1 and C2. In both maps, a third-order polynomial was subtracted at each gate voltage to remove a smooth background.

The two-terminal magneto-conductance measurements suffer from large background resistances due to Schottky barriers, which we can partially circumnavigate by performing a three-terminal experiment. In Figure Figure B.1 b),

we plot the dc conductance $G_{24,21}$, as explained in the figure caption. This technique removes the contact resistance at C4 so that the conductance resonances due to the Landau levels can be measured more clearly. The results in Figure B.1 b) show similar patterns as in better-suited Hall bar experiments, exhibiting clear superposition patterns of the spin and valley split subbands, indicated by dashed lines. We note that due to the less ideal contact geometry of our devices, we cannot go to lower electron densities in these experiments, because the current density passing near the remote contacts is very low. For more information see Refs. [39, 149]

Extraction of superconductor energy gap as function of magnetic field

In the main text of section 5.1 we show the dependende of the superconducting MoRe energy gap as a function of B extracted by different methods. In Figure fig:add:morefields we provide a few examples of the V_{BG} ranges which were average to plot Figure 5.3 a).
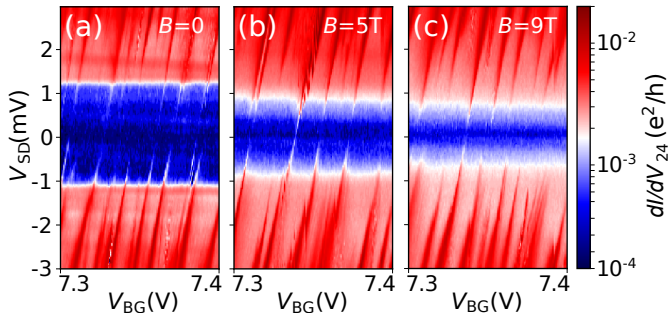

Figure B.2. Conductance G_{24} as a function of V_{SD} and V_{BG} at a) $B = 0$, b) $B = 5\,\text{T}$, and c) $B = 9\,\text{T}$.

Figure B.3 shows the Coulomb resonance tips with which the blue rectangles in Figure 5.3 b) were extracted.
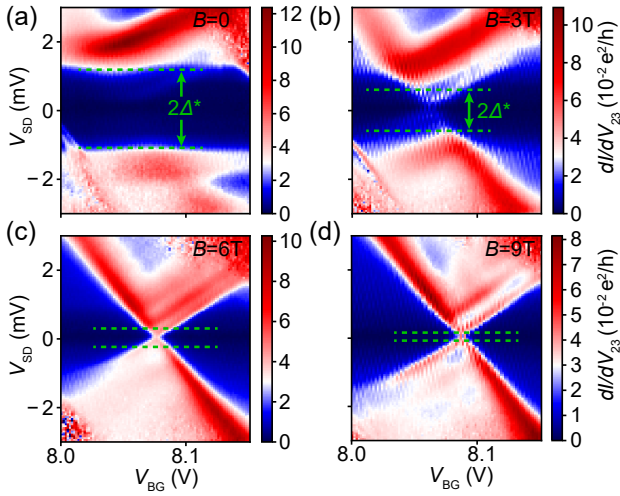
Figure B.3. Conductance as a function of V_{SD} and V_{BG} using contacts C2-C3 at the perpendicular magnetic fields indicated. The green dashed lines show the V_{SD} used for extracting the energy gap (blue rectangles) in Figure 5.3.

C Additional data to Device II

Magnetic field dependence of the superconducting energy gap

We measure the magnetic field dependence of the suppression in device II, resultant of the quasiparticle tunneling through the N-S interfaces. Figure C.1 a) show the conductance as functions of B and V_{SD} at $V_{BG} = 8\,\text{V}$. The indicated cross sections are plotted in Figure C.1 b). The behavior is similar to the observed in device I.
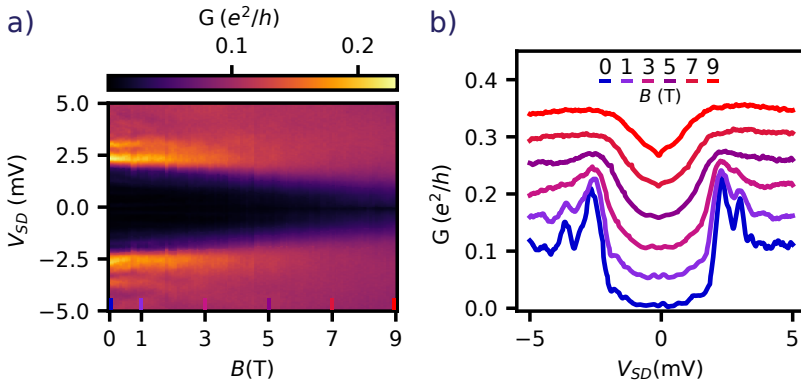

Figure C.1. Magnetic field dependence of device II. a) Differential conductance as function of B and V_{SD} at $V_{BG} = 8\,\text{V}$. b) Cross section in V_{SD} for the magnetic fields indicated. Curves are displaced in y-axis.

About the resonance slopes in the gate-bias dependence

In this section, we investigate in some detail what the slope of the conductance resonances should be when the differential conductance is plotted as a function of the bias voltage, V_{SD} and the backgate voltage, V_{BG}.

If the electron density would be determined solely by V_{BG}, we would expect only resonances with a positive slope, i.e. each change in the source electrochemical potential is compensated by a corresponding change in the gate voltage to follow a constant electron density. This slope would be given by

$$s = \frac{dV_{SD}^{(\text{res})}}{dV_{BG}^{(\text{res})}} = \frac{\pi\hbar^2 c}{pe^2 m^*}, \tag{C.1}$$

where $c = \epsilon\epsilon_0/d$ is the geometrical capacitance per area formed by the backgate and $p = 2$ the band degeneracy. However the actual values and the visible negative sloped resonances do not match this picture.

We do not expect a significant capacitive coupling from the contacts to the active region of the device, as we obtain very similar slopes and patterns in long and short devices using other contact pairs. The average electrochemical potential on the MoS$_2$ must lies in between μ_S and μ_D. To exactly determine its position we assume that in equilibrium

$$\frac{dn}{dt} = r_{S_{in}} + r_{D_{in}} - r_{S_{out}} - r_{D_{out}} \overset{!}{=} 0 \tag{C.2}$$

where $r_{S,D}$ are the rate of carrier coming from (or moving out) the source and drain leads. We can write $r_{S,D}$ in terms of the transmission probabilities $\Gamma_{S,D}$ by

$$f_S D_S \Gamma_S (1-P) D_N + f_D D_D \Gamma_D (1-P) D_N$$
$$- (1-f_S) D_S \Gamma_S P D_N - (1-f_D) D_D \Gamma_D P D_N \overset{!}{=} 0 \quad \text{(C.3)}$$

with $D_{S,D}$ the quasiparticle density of states of the superconductor, D_N the density of states in the normal conductor, f the Fermi distribution and P the occupation probability. In this picture we neglect Andreev reflection processes, i.e. we assume a small transmission probability to the reservoirs. With that, we can estimate the occupation probability $P(E)$ as

$$P(E) = \frac{D_S(E-\mu_S)f(E-\mu_S)\Gamma_S + D_S(E-\mu_D)f(E-\mu_D)\Gamma_D}{D_S(E-\mu_S)\Gamma_S + D_D(E-\mu_D)\Gamma_D},$$

The electron density is given by the gate voltage, with only the conduction band minimum E_{cbm} as a free parameter,

$$n = \int_{E_{cbm}}^{\infty} P(E)D_{2D}dE = \frac{c}{e}\Delta V_{BG},$$

with $D_{2D} = p\frac{m^*}{\pi \hbar^2}$ the density of states in the 2D semiconductor and ΔV_{BG} the gate voltage measured from the pinch-off voltage (here $\sim 0.2\,\text{V}$). With E_{cbm} known, we can then calculate the electrical current

$$I = \int_{E_{cbm}}^{\infty} T(E)[f(E - \mu_S) - f(E - \mu_D)]dE,$$

with the transmission $T(E)$ determined by the constructive interference in the device, for which we simply take a periodic function in E.

These equations can be easily evaluated numerically. The corresponding differential conductance $G = dI/dV_{SD}$ is plotted in Figure C.2, in a) for symmetric tunnel barriers, which results in the positive slopes following equation C.1. The corresponding change in the conduction band minimum is plotted in Figure b) and depends only on the gate voltage.

In contrast, by choosing asymmetric barriers or different background DoS, we find a qualitatively very similar pattern as in our experiments in the main text, namely an alternating visibility of the positive and negative slopes when the bias is set below the Δ/e and $2\Delta/e$, respectively, show in Figure C.2 c). To compare with the experiment, we also plot the conductance normalized separately for each bias voltage in Figure C.2 e). Again, we plot the corresponding modulation of the conduction band minimum in Figure C.2 d), which now depends on both, V_{SD} and V_{BG}.

The physical meaning can be understood easily by considering that a stronger coupling to a reservoir gives a larger weight to the respective electrochemical potential - reduced for energies in the BCS gaps.

For the main text, it is important to note that the spacing between the resonances in gate voltage *does not depend* on the bias, which can be directly seen in Figure C.2 f), since the number of resonances in the plotted gate voltage range is the same for each bias.
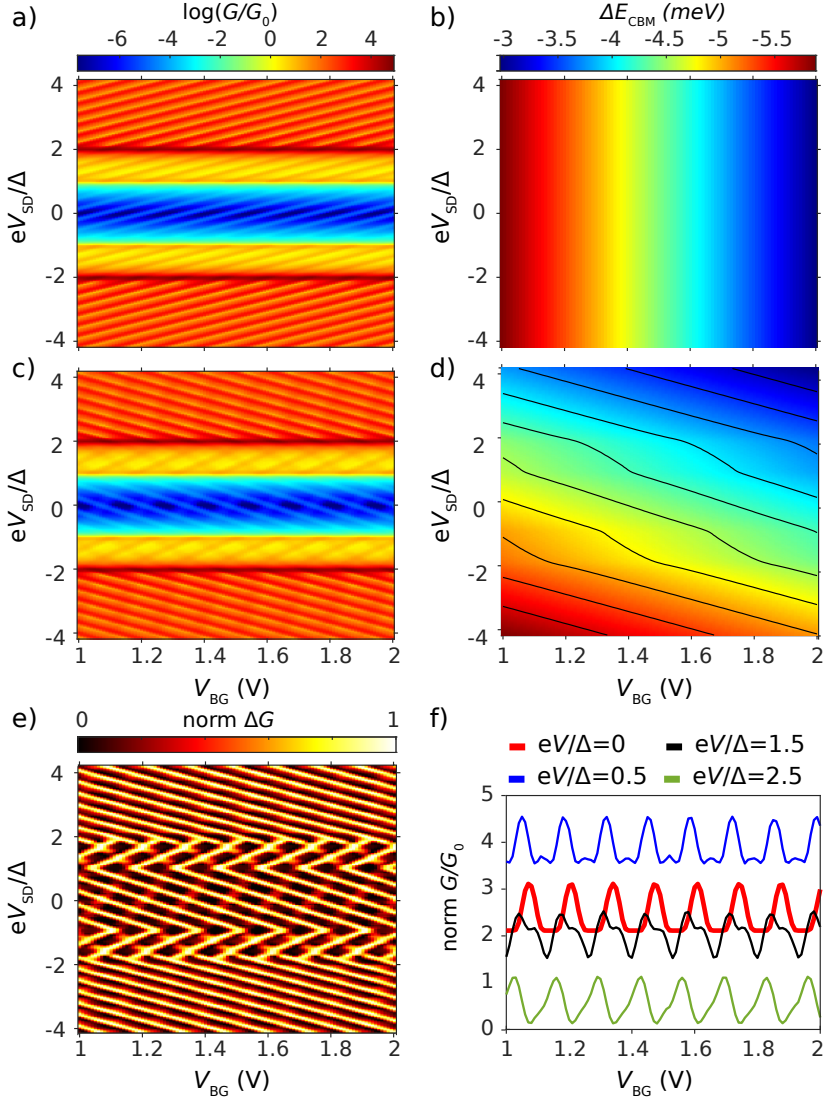
Figure C.2. From a), c) and e) Differential conductance as a function of bias voltage and backgate voltage. a) Symmetric tunnel barrier and symmetric bias c) Asymmetric barriers with different DoS at superconductors. e) Same as c) with normalized conductance of each bias voltage. b) and d) are the corresponding shifts in CB minimum for symmetric and asymmetric barriers, respectively. f) Cross sections of the indicated bias voltage in c).

D Additional data to MoRe InSe device

This section presents additional data plots to the MoRe VIA contacts to a few layers InSe presented in section 6.2.

Figure D.1 shows plots of conductance as a function of B and V_{SD} for a) contacts C1-C2, where a suppression of Δ/e in bias is observed and b) for contacts C1-C4, with a suppression of $2\Delta/e$ in bias. The general tendency of the suppression is a decrease in bias voltage as the magnetic field increases. Additionally, the sub-gap peaks can be followed as they increase in bias voltage.
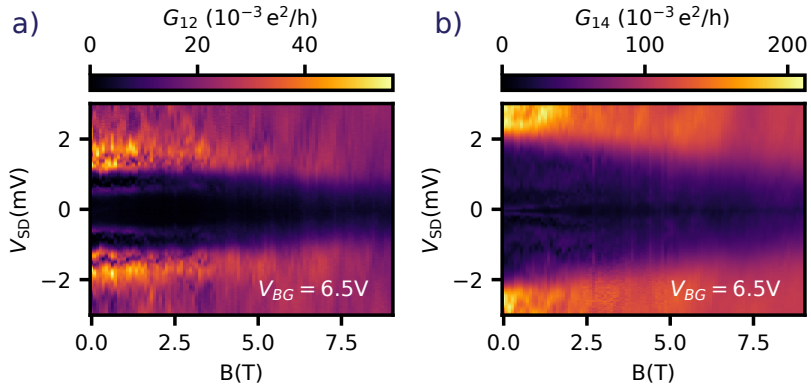

Figure D.1. a) Conductance as a function of B and V_{SD} for contacts C1-C2. b) Conductance as function of B and V_{SD} for contacts C1-C4.

E Fabrication Recipes

In the following we give the detailed fabrication recipes used during this project.

Van der Waals heterostructure fabrication

Material sources

1. Graphite: HQ-graphene

2. hBN: T. Taniguchi et al., National Institute for Material Science, 1-1 Namiki, Tsukuba 305-0044, Japan

3. MoS_2:SPI supplies, natural source (Australia and Canada)

4. InSe: grown by the Bridgman method. Credited to Dr. Zakhar Kudrynskyi and Prof. Dr. Amalia Patanè at the University of Nottingham.

5. Exfoliation tape: NITTO ELP-150P-LC

Reactive ion etching

CHF_3/O_2

1. CHF_3/O_2 (40 sccm/4 sccm); power 60 W; pressure 60 mTorr

2. Etching rates:
   - hBN: 0.3-0.33 nm/s
   - SiO_2: ~0.23 nm/s
   - graphite: 0.07 nm/s

$SF_6/Ar/O_2$

1. $SF_6/Ar/O_2$ (20 sccm/5 sccm/4 sccm); power 50 W; pressure 25 mTorr

2. Etching rates:

- hBN: $>6.35\,\mathrm{nm/s}$
- SiO_2: $\sim0.5\,\mathrm{nm/s}$

3. After the SF_6 etching a O_2 plasma (E) was used to remove cross-linked PMMA.

O_2

1. O_2 (20 sccm); power 60 W; pressure 40 mTorr

2. Etching rates:
    - hBN: $\sim0.33\,\mathrm{nm/s}$
    - PMMA: $\sim1.66\,\mathrm{nm/s}$

Electron beam lithography

PMMA mask for etching and contact deposition

E

1. Prebake at $180\,^\circ$C for 3 min

2. PMMA 950K (AR-P 672.045 Allresist) solid content 4.5-5.5%

3. Spin coat at 4000 rpm for 40 s with ramp rate of 1000 rpm/s ($\approx 450\,nm$)

4. Postbake at $180\,^\circ$C for 3 min

5. Exposure with e-beam (EHT=20 kV; dose$\approx 400\,\mu$C/cm^2)

6. Development in cold ($\sim5\,^\circ$C) IPA:H_2O (7:3) for 60 s

7. Blow dry with N_2

PMMA lift-off

1. Sample in Acetone (T=50 $^\circ$C) for 30 min

2. Remove excess metal by Acetone flow created with a pipette

3. Transfer to IPA bath

4. Blow dry with N_2

Metal deposition

Fabrication of VIA contacts

- Clean Si substrate with acetone and IPA bath. O_2 plasma for 1 min to enhance adhesion and further clean surface.

- Exfoliate hBN and select flakes with proper thickness and area.

- PMMA mask contact areas by EBL (E)

- SF_6 etching the whole hBN thickness. (E)

- Wash away resist in acetone followed by IPA bath.

- Second step of EBL defining areas slightly larger than the etched areas.

- Contact material evaporation:
  - Sputter MoRe using a AJA ATC Orion.
  - Ignite plasma (Ar 30 sccm, pressure 20 mT, power 50 W)
  - Presputter for 1-2 min
  - Single MoRe (1:1) target:
    * power 100 W
    * background pressure 2 mTorr
    * Ar flow 30 sccm
    * Sample rotation "on"
    * height 40 cm
    * rate 0.27 nm/s
  - Lift off in acetone warm acetone bath.

Fabrication of Bi-Au/Al contacts

1. PMMA mask defined by EBL (E)

2. 30s O_2 etching (E) to increase the adhesion

3. The metal was deposited using a Sharon e-beam evaporator

4. 5 nm of Ti or Cr was deposited as a sticking layer

5. Evaporate Au

6. Lift-off in Acetone (E)

Fabrication of metal top gates

1. PMMA mask defined by EBL (E)

2. 30s O_2 etching (E) to increase the adhesion

3. Deposite metal using e-beam evaporator

4. Pre-deposition of Ti to trap Oxygen and lower the chamber pressure

5. 5 nm of Ti as a sticking layer

6. Au deposition to desired thickness

7. Lift-off in Acetone (E)

PC mixture

1. rinse glass vial and magnetic stirring bar with chloroform

2. add 0.7 g of Poly(Bisphenol A carbonate)

3. add 20 ml of chloroform

4. stir over several hours at $40°$ C until Pc is completely dissolved

Assembly of viscoelastic stamp

1. Clean glass slides in a acetone followed by IPA bath.

2. Drop PC mixture in a glass slide and press it with a second slide, dispersing the liquid. In a rapid sliding movement, separate the two slides remaining a thin PC film. Wait 5min for the film to dry.

3. Place 1mm square cubes of PMDS onto glass slide.

4. Place the PC film on the top of the PMDS cube with help of stick tape.

Curriculum Vitae

Ian Correa Sampaio
Born on 15$^{\text{th}}$ September 1991 in Belo Horizonte (Brazil)

Education

5/2019–now	**PhD in experimental physics at the University of Basel, Switzerland**

- Dissertation in the group of Prof. Dr. C. Schönenberger
  "Two dimensional Semiconductors-Superconductor hybrid devices"

9/2016–11/2018	**Masters of Science in Physics at the Free University of Berlin, Germany**

- Master thesis in the group of Dr. S. Ludwig (Paul Drude Institute for Solid State Electronics, Berlin)
  "Electron Optics in a parabolic cavity with two Quantum Point Contacts"

6/2014–6/2015	**Exchange program at the University of Bergen, Norway**
2/2010–3/2016	**Bachelors of Science in Physics at the Federal University of Belo Horizonte, Brazil**

Positions

8/2019–now	*Teaching assistant for physics at the University of Basel*
2018–2019	*Research assistant in the group of S. Reich at the Free University of Berlin, Germany*

Publications

- *"Superconducting Contacts to a Monolayer Semiconductor"*
  M. Ramezani, **I. Correa Sampaio**, K. Watanabe, T. Taniguchi, C. Schönenberger, and A. Baumgartner
  Nano Letters, 12, 13, 5614-5614 (2021)

- *"Coherent transport and two dimensional Andreev bound states in a monolayer semiconductor"*
  M. Ramezani, **I. Correa Sampaio**, K. Watanabe, T. Taniguchi, C. Schönenberger, and A. Baumgartner
  in preparation

- *"Electrostatics and magnetic field behavior of a Quantum Point Contact in monolayer MoS_2"*
  I. Correa Sampaio, K. Watanabe, T. Taniguchi, C. Schönenberger, and A. Baumgartner
  in preparation

- *"Superconducting bulk and edge contacts to few-layer InSe"*
  I. Correa Sampaio, K. Watanabe, T. Taniguchi, C. Schönenberger, and A. Baumgartner
  in preparation

- *"Optical Absorption of Dye Molecules Remains Unaffected by Submonolayer Complex Formation with Metal Nanoparticles"*
  V. Petráková, **I. Correa Sampaio**, and S. Reich
  Journal of Physical Chemistry C 123, 28, 17498–17504 (2019)

Talks

- *Superconducting contacts to mono- and few-layer semiconductor crystals*
  Graphene 2021, Grenoble (France), October 2021

- *Subgap resonances in monolayer semiconductors with superconducting contacts*
  CMD 29, Manchester (United Kingdom), August 2022

- *Andreev bound states in monolayer semiconductor-superconductor hybrid devices*
  Graphene Workshop 2022, Budapest (Hungary), October 2022

Poster Contributions

- *"Towards fabrication of 2D semiconductor nanostructures with superconducting contacts"*
  NCCR QSIT Junior Meeting 2019, Flumserberg (Switzerland), June 2019

- *"Towards fabrication of 2D semiconductor nanostructures with superconducting contacts"*
  9th NCCR QSIT Winter School and 10th NCCR QSIT General Meeting, Arosa (Switzerland), January 2020

- *"Towards atomically thin molybdenum disulfide nanostructures with superconducting contact"*
  21st International Winterschool in New Developments in Solid State Physics, Mauterndorf (Austria), February 2020

- *"Superconducting contacts to mono- and few-layer semiconductor crystals"*
  The Swiss Nanoconvention 2021, Online, June 2021

Acknowledgements

A doctoral degree is an exciting period, filled with new knowledge, hard work, and uncertainty. All the ups and downs of diving into a novel problem are much easier if you are not alone. Luckily, I had great supervision and colleagues to bring this project to its conclusion. I would like to dedicate the paragraphs below to those who supported me along the way.

Before anything else, I would like to thank Prof. Dr. Christian Schönenberger for the opportunity to work on his group and to learn from one of the experts in nanoelectronics and quantum transport. Christian not only provides all the resources for doing excellent research but also keeps the group in a good mood and in close cooperation with frequent meetings and awesome group excursions.

My gratitude to Dr. Andreas Baumgartner. Thanks for assigning me to this project and for all the numerous hours you spent discussing, thinking, troubleshooting, or just hearing our frustration. This project would of course not be possible without you, but you also played an important role in my education as a scientist.

I would like to thank Prof. Dr. Thomas Ihn and Dr. Stefan Heun for taking part in the examination committee, reading and evaluating this work. It is an honor to me.

A special thanks to Barbara Kammermann, who is capable of making the bureaucracy of the whole world seem effortless! Thanks for all the help you provided, which started even before I stepped into Basel for the first time.

A big thank you to my lab mate Dr. Mehdi Ramezani for sharing this difficult project with me. Your hard work and commitment thrusted this project and saved our PhDs. Only we know the countless fabrication hours, broken samples, and discussions we had along the way.

Thanks to Dr. Paritosh Karnatak, for his advice and company in conferences and climbing halls.

Thank you to my big-office-mates Dr. Alessia Pally, Blesson Varghese, Deepankar Sarmah and Rounak Jha. Only you guys know how tough and fun is to make part of this messy room.

Thank you, Dr. Roy Haller, for the nice inputs you sporadically drop throughout my PhD and for the great time we spend in Manchester.

Thank you to all my colleagues of team MESO Dr. Martin Endres and